UNIVERSITY OF CALIFORNIA

Los Angeles

Additive manufacturing and characterization of structural and multi-functional metamaterials via a large-area high-resolution stereolithography system

A dissertation submitted in partial satisfaction of the

requirements for the degree Doctor of Philosophy

in Civil Engineering

by

Huachen Cui

2020

ABSTRACT OF THE DISSERTATION

Additive manufacturing and characterization

of structural and multi-functional metamaterials

via a large-area high-resolution stereolithography system

by

Huachen Cui

Doctor of Philosophy in Civil Engineering

University of California, Los Angeles, 2020

Professor Xiaoyu (Rayne) Zheng, Chair

Projection micro-stereolithography (PμSL) is a technique for micro-fabrication that can fabricate complex three-dimensional (3D) microstructures. However, this technique has been limited to printing low-volume structures with high resolution. My dissertation research introduces a large-area projection stereolithography (LAPμSL) system that integrates scanning optics with the existing PμSL to manufacture cm-scale objects with micro-scale architectures. This technique enables the fabrication of structures with features down to the sub-10μm scale and overall size up to hundreds of millimeters, which is particularly suitable for fabricating micro-architected metamaterials with large volumes that can be employed in a broad array of applications.

The LAPμSL system is capable of fabricating multi-scale features, making it possible to create lightweight structural materials with feature sizes from a few micrometers to hundreds of millimeters. Herein, we studied the process-structure-property relationships of a class of high-temperature ceramics via LaPμSL. This study, for the first time, achieves high-resolution printing of high-temperature ceramics, with accurate three-dimensional feature sizes on the scale of a few micrometers, opening new opportunities for high-temperature material and device manufacturing. We discovered the size-dependent mechanical properties of high-temperature ceramics and their failure properties corresponding to various feature sizes. Furthermore, the LAPμSL system is capable of fabricating metamaterials containing millions of unit cells, providing a unique experimental platform to study the fracture and damage tolerance of metamaterials. We additively manufactured stretch-dominated architected metamaterials with pre-defined embedded crack, where the size of the unit cells becomes sufficiently small compared to the flaw dimensions. Via combined experimental, X-ray tomography and numerical calculations, we have elucidated the emergence of fracture toughness as a material property in architected metamaterials, which is found to be a property largely influenced by the elastic instabilities of struts members and T-stress, A design map based on a 2-parameter fracture model was developed to guide the design of failure modes in micro-architected metamaterials.

Beyond structural materials, my research then extends to the design and additive manufacturing of multi-functional materials and assembly-free devices for directional sensing, underwater transducers and meso-scale robotic systems. Using piezoelectric materials as an example, we demonstrated the process-structure-property relationships of additive manufacturing of multi-functional materials and energy transduction devices. A novel micro-stereolithography system integrated with the blade-casting process was developed and employed to print piezoelectric particles with surface functionalization. These as-printed piezo-active materials can be rationally designed to achieve programmable voltage-strain responses, going beyond the limitations of the intrinsic crystalline structures. The design strategy can be applied to create the next generation of intelligent infrastructure, able to perform a variety of structural and functional tasks, including simultaneous impact absorption and monitoring, three-dimensional pressure mapping and directionality detection. This study demonstrated the ease of implementation and utility of the piezoelectric metamaterials in underwater applications. Underwater transducers consisting of rationally designed metamaterials to accommodate diverse frequency ranges were developed. Through tuning geometry of the micro-architectures, the working range of the underwater transducers can vary from 10kHZ to 4MHz. With this broad frequency range, we developed hydrophones with arbitrary directivity patterns and ultrasonic array with high sensitivity. This study showed the feasibility and applicability of these underwater transducers for noise elimination and underwater object detection.

Additionally, leveraging these piezo-active micro-architectures, my research then focused on additive manufacturable piezoelectric actuation metamaterials, with programmable deformation modes, including twisting, bending, shearing and axial strain under uniform electric fields. As a consequence of freeform design and fabrication, different types of metamaterial blocks and actuation modes can be combined into a single-piece material block and construct multiple degree-of-freedom modular actuation elements. The stackable, modular actuation elements allow the generation of complex coupled or decoupled motion without any transmission systems, which increases the energy efficiency of robotic systems generated by the piezoelectric metamaterials.

The dissertation of Huachen Cui is approved.

Ertugrul Taciroglu

Jian Zhang

Mathieu Bauchy

Xiaoyu (Rayne) Zheng, Committee Chair

University of California, Los Angeles

2020

Table of Contents

List of figures

Acknowledgements

I would like to thank Prof. Xiaoyu (Rayne) Zheng for taking the time to work with and guide me through the past five years. I appreciate that Dr. Zheng gave me this opportunity to explore different areas of research.

I would like to thank all my committee members for helping me go through the completion of a Ph.D. degree at UCLA.

I wish to express my gratitude to all my group mates for their advice and support in my work. In the AMML (Advanced Manufacturing and Metamaterials Laboratory). I have enjoyed a very open atmosphere with your accompanying.

I would like to acknowledge my family and all the support they have given me. They have always been there to support me and push me forward.

I would like to acknowledge NSF (CMMI-17277492), Air Force Office of Scientific Research (FA9550-18-1-0299), Office of Naval Research (N00014-18-1-2553) and ICTAS Junior Faculty Award and Startup support from Virginia Tech and University of California, Los Angeles for funding support.

Chapter 1.2.1, 2, 3.1 is reproduced from "**Huachen Cui**, Ryan Hensleigh, Hongshun Chen, Xiaoyu Zheng, Additive Manufacturing and size-dependent mechanical properties of three-dimensional microarchitected, high-temperature ceramic metamaterials, Journal of Material Research, 2018, Volume 33, pp. 360-371, DOI: 10.1557/jmr.2018.11"[1].

Chapter 3.3 is adapted from "Chengwei Wang, Weiwei Ping, Qiang Bai, **Huachen Cui**, Ryan Hensleigh, Ruiliu Wang, Alexandra H. Brozena, Zhenpeng Xu, Jiaqi Dai, Yong Pei, Chaolun Zheng, Glenn Pastel, Jinlong Gao, Xizheng Wang, Howard Wang, Ji-Cheng Zhao, Bao Yang, Xiaoyu (Rayne) Zheng, Jian Luo, Yifei Mo, Bruce Dunn, Liangbing Hu, A general method to synthesize and sinter bulk ceramics in seconds, Science, 2020, Volume 368, pp. 521-526, DOI: 10.1126/science.aaz7681"[2].

Chapter 1.3, 4&5 is reproduced from "**Huachen Cui**, Ryan Hensleigh, Desheng Yao, Deepam Maurya, Prashant Kumar, Min Gyu Kang, Shashank Priya, Xiaoyu (Rayne) Zheng, Three-dimensional printing of piezoelectric materials with designed anisotropy and directional response, Nature Materials, 2019, Volume 18, pp. 234-241, DOI: 10.1038/s41563-018-0268-1"[3].

Chapter 6 is a manuscript in preparation for publication.

Chapter 7 is a manuscript in preparation for publication.

Vita

Education

Doctor of Philosophy, Civil & Environmental Engineering Expected: Dec. 2020
UCLA, Log Angeles, CA
Doctor of Philosophy, Mechanical Engineering Transferred to UCLA, Sep. 2019
Virginia Tech, Blacksburg, VA
Bachelor of Science, Manufacture and Automation in Mechanical Engineering, Jun. 2016
Shandong University, China

Journal Publications

- **H. Cui,** R. Hensleigh, D. Yao, D. Maurya, P. Kumar, M. G. Kang, S. Priya, X. Zheng, "Three-dimensional printing of piezoelectric materials with designed anisotropy and directional response", ***Nature Materials (IF: 38.9), 2019*** (Featured on VT News, reported by Science Daily, 3D PRINTING INDUSTRY, Eurek Alert!, Materials Today, Phys. Org, UVEB Technology, etc)
- **H. Cui,** R. Hensleigh, H. Chen, X. Zheng, "Additive Manufacturing and size-dependent mechanical properties of three-dimensional micro-architected, high-temperature ceramic metamaterials", ***Journal of Materials Research, 2018*** (Selected as 2018 Journal of Materials Research Paper of the Year Award, Materials Research Society, reported by Eurek Alert!, SCIENMAG, etc)
- C. Wang, W. Ping, Q. Bai, **H. Cui,** R. Hensleigh **(contributed equally)**, et. al., "A general method to synthesize and sinter bulk ceramics in seconds", ***Science (IF: 41.1), 2020*** (Featured on front cover, reported by c&en, Nanotechnology Now, Yahoo News!, Science Daily, etc)
- R. Hensleigh, **H. Cui (contributed equally),** Z. Xu, J. Massman, D. Yao, J. Berrigan, X. Zheng, "Charge-programmed three-dimensional printing for multi-material electronic devices", ***Nature electronics, 2020*** (Reported by c&en, Tech Xplore, 3D printing industry, etc)
- D. Yao, **H. Cui,** R. Hensleigh, P. Smith, S. Alford, D. Bernero, S. Bush, K. Mann, H. F. Wu, M Chin-Nieh, G. Youmans, X. Zheng, "Achieving the upper bound of piezoelectric response in tunable, wearable 3D printed nanocomposites", ***Advanced Functional Materials (IF: 15.6), 2019*** (Featured on front cover)
- W. Cheng, J. Liu, Z. Zheng, X. He, B. Zheng, H. Zhang, H. Cui, X. Zheng, T. Zheng, B. E. Gnade, J. Cheng, "Adaptive optical beam steering and tuning system based on electrowetting driven fluidic rotor", ***Communications Physics, 2020***
- X. Zheng, W. Smith, J. Jackson, B. Moran, **H. Cui**, D. Chen, N. Fang, J. Ye, T. Weisgrabber, C. Spadaccini, "Multi-scale Metallic Metamaterials" ***Nature Materials (IF: 38.9), 2016*** (Featured on front cover, VT News, reported by Phys.org, Science Daily, Nanowerk, Materials Today, 3Dprint.com etc)
- R. Hensleigh, **H. Cui,** J. Oakdale, J. Ye, P. Campbell, E. Duoss, C. Spadaccini, X. Zheng, M. Worsley, "Additive manufacturing of complex micro-architected graphene aerogels", ***Materials Horizons (IF: 14.4), 2018,*** (Featured on front cover, VT news, reported on SCI

NEWS, 3D PRINTING INDUSTRY, etc)

- N. Gerad, **H. Cui,** C. Shen, Y. Xie, S. Cummer, X. Zheng, Y. Jing, "Fabrication and experimental demonstration of a hybrid resonant acoustic gradient index metasurface at 40 kHz", ***Applied Physics Letters, 2019***

Conferences

- **H. Cui**, A. Shikeea, M. O'Masta, V. Deshpande, X. Zheng, "Fracture toughness of low-density 3D architected metamaterial", ***International Union of Theoretical and Applied Mechanics Symposium, Chicago, IL, Sep. 2018***
- **H. Cui**, R. Hensleigh, D. Yao, D. LoPinto, X. Zheng, "Three-dimensional printing of piezoelectric materials with designed anisotropy and their applications in underwater sensing", ***International Solid Freeform Fabrication Symposium-Additive Manufacturing Conference, Austin, TX, Aug. 2019***
- **H. Cui,** R. Hensleigh, D. Yao, X. Zheng, "Three-dimensional printing of piezoelectric materials with designed anisotropy and their applications", ***International Design Engineering Technical Conferences, Anaheim, CA, Aug. 2019***
- **H. Cui,** R. Hensleigh, D. Yao, X. Zheng, "Self-powered hydrophone with broadband frequency and rationally designed directivity pattern via 3D printing using piezoelectric metamaterials", ***Materials Science & Technology, Portland, Oregon, Oct. 2019***
- A. Shikeea, **H. Cui,** M. O'Masta, X. Zheng, V. Deshpande, "New rules for fracture limited design in micro-architected cellular solides", ***Society of Engineering Science Annual Technical Meeting, St. Louis, MO, Oct. 2019***
- **H. Cui,** R. Hensleigh, D. Yao, D. LoPinto, X. Zheng, "Three-dimensional printing of piezoelectric materials with designed anisotropy and their applications in underwater transducers", ***American Physical Society March Meeting 2020, On-line, Mar. 2020***

Honors &Awards

- National Science Foundation Student Travel Award, **International Solid Freeform Fabrication Symposium-Additive Manufacturing Conference, 2019**
- 1st Place Prize in the Annual Material Advantage Graduate Student Poster Contest (co-authored), **Material Science and Technology (MS&T) Conference, 2019**
- 2018 Journal of Materials Research Paper of the Year Award, **Materials Research Society, 2018**
- National Science Foundation Student Travel Award, **International Solid Freeform Fabrication Symposium-Additive Manufacturing Conference, 2017**
- National college student business plan competition: **3rd Prize, nationally, 1st Prize of Shandong Province, China (Sep. 2014)**
- University level (Shandong University): **2nd Prize Scholarship (Sep. 2013), 1st Prize in student design competition (Oct. 2014), 1st Prize in energy saving technology competition (Mar. 2015)**

Chapter 1 Introduction

This chapter includes the background introduction of the micro-stereolithography technique, the structural high-temperature ceramic, fracture toughness study of micro-architected metamaterials and multi-functional metamaterials. The initiation and objectives of the studies are also introduced at the end of each section.

1.1 Micro-stereolithography

Here, two types of micro-stereolithography are introduced and compared. One of them using scanning stereolithography to cure the photopolymer (UV curable resin) while another one using the digital light projection method. For both kinds of systems, they follow the steps shown below:

1. Generation of the 3D structure that needs to be printed.
2. Adding support material to the CAD model.
3. Setting up the printing parameters including layer thickness and exposure time, etc.
4. Slice the model to generate the 2D slice patterns.
5. Upload slice file and printing parameters to the system.
6. Printing of the 3D structure.
    a) Coating of the UV curable resin

b) UV exposure and solidification of the resin

c) Moving the printing stage by one-layer thickness

d) Recoating of the UV curable resin

e) Repeating step b) ~d) until the printing is done

7. Post process including cleaning, post-exposure, trim support, etc.

The scanning stereolithography scans a laser dot through optics on the surface of the resin according to the programmed laser path based on the 2D slices. In this process, the scanning of the laser dot is controlled by a dual-axis galvo-mirror. A schematic of a scanning stereolithography system is shown in Fig. 1-1.

The projection stereolithography projects the whole 2D slice pattern on top of the resin surface and cures the whole layer in the meantime. The principle of the Projection Stereolithography is given in Figure 1-.

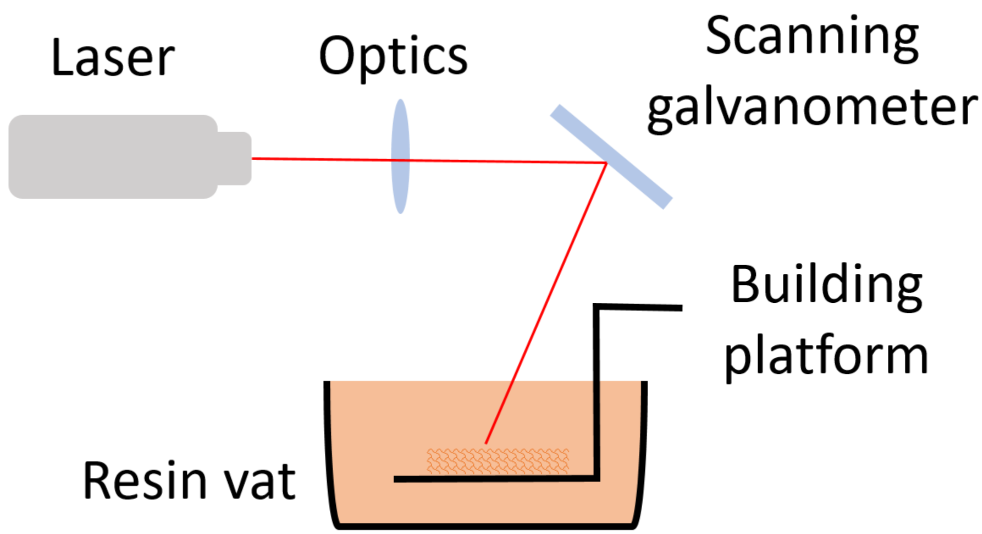

Figure 1-1 Schematic of a scanning stereolithography system

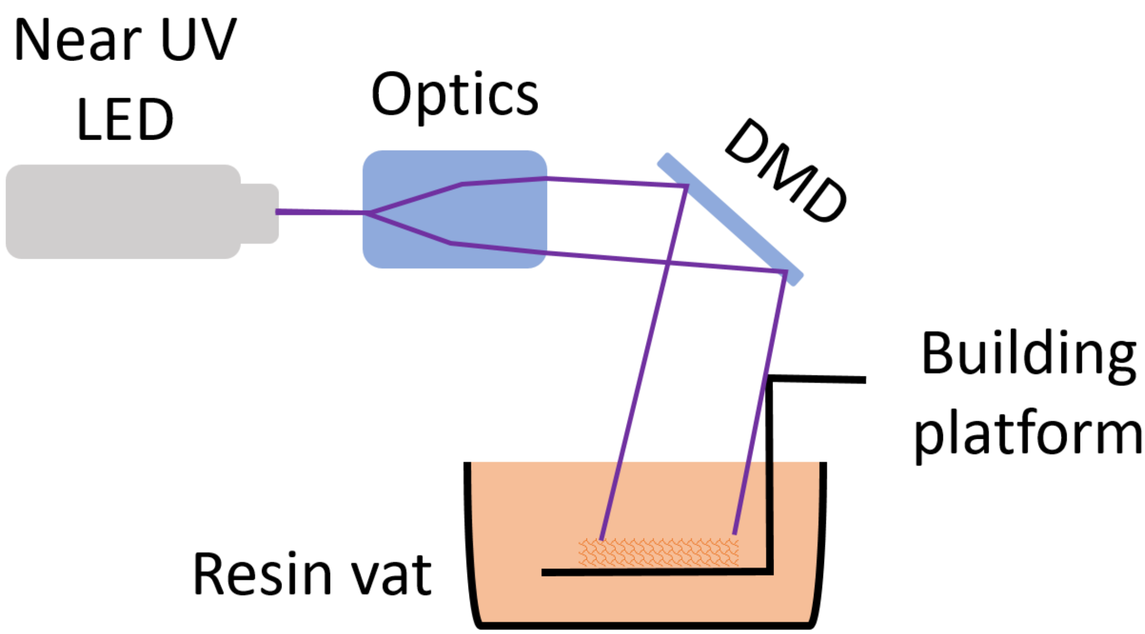

Figure 1-2 Schematic of a projection stereolithography system

The difference between the two kinds of systems is the curing method of a layer. The scanning stereolithography scans 1D laser dots within one layer using two optical mirrors while the projection stereolithography projects the 2D pattern of the layer and all optics do not move during the curing process. The projection stereolithography is preferred due to its high speed and simpler control systems.

In this study, a large-area high-resolution projection micro-stereolithography system was set up based on the projection stereolithography technique, so most literature shown here is related to projection stereolithography.

The projection stereolithography technique was first introduced by Bertsch (1997). The technique employs a spatial light modulator, which is also known as a dynamic mask, to manipulate the UV pattern when the light passes through the modulator. Optics are then placed in the light path to focus the UV pattern on the surface of the liquid resin. The UV light cures the photocurable polymer and forms a layer of solid with the desired pattern. This procedure is repeated layer by layer and the stack of the layers yields the 3D objects.

The dynamic mask is the most important part of the projection stereolithography system and it can be liquid crystal display (LCD) or digital micromirror devices (DMD). Bertsch employed an LCD screen to manipulate pixels and pattern the light by controlling the orientation of the liquid crystal molecules. However, the LCD devices have low transmissivity to UV light and cannot afford high-power UV. Compared to LCD, DMD chips are more frequently used in current projection stereolithography systems because of their smaller pixel size, faster response and high UV transmissivity.

Sun, et. al developed a high-resolution PμSL system with the DMD chip. The system was employed for fabricating complex 3D microstructures which are widely used for micro-electro-mechanical systems (MEMS). A process model was also introduced in this work with all printing parameters generated from experiments. The photo-curing process was quantitatively studied and the minimum feature printed by his system was 0.6μm.[4]

Zheng, et. al designed and optimized a PμSL and demonstrated the manufacturing of a broad array of complex 3D structures from micro- to mesoscale. The system utilized an LCoS mask to achieve a high contrast ratio and small pixel size. The effect of parameters including exposure time, photo-initiator, photo-absorber on the curing depth was investigated and optimized experimentally. To enlarge the printing area, the authors developed a step-and-repeat process, which divided the exposure image into several sub-images. After the printing of the first sub-image, the UV light was turned off and the translation stage moves the building platform to the position of the next sub-image.[5]

Ha et.al developed a system that can realize mass production of 3D architected material in meso-range with a resolution of few microns. The illumination was calibrated to be uniform and the image formation was based on an optical design from fabricating microstructure arrays.[6]

Yayue Pan, et. al. proposed a direct digital manufacturing process based on a mask-image-projection method. The system uses a bottom-up projection configuration and a two-way linear motion approach was employed for recoating the liquid resin with a uniform thickness.[7]

However, the works shown above either suffers from the trade-off between the projection resolution or the unstableness induced by the motion of a heavy building platform. Inspired by these works, a large-area high-resolution stereolithography system was developed and optimized. Instead of moving the building platform or projection system, the system utilizes a parallel light path and moving mirrors to enlarge the printing area with an appropriate building speed.

1.2 Mechanical metamaterials

1.2.1 Mechanical metamaterials made of ceramics

Engineering ceramics offer several beneficial properties, including high strength, wear resistance, high-temperature stability, and lightweight compared to metals. These properties are desirable for many applications, including aerospace components such as gas turbine engines [8-12], as catalysts support [13], bio-ceramic scaffolds for tissue engineering[14, 15], and as temperature-resistant electronics, micro-electromechanical systems (MEMS)[16-20] etc. Despite these desirable properties, bulk ceramics have limited applications due to their high flaw sensitivity, bulky weight and catastrophic fracture behavior upon loading, attributed to the persistence of distributed flaws within the ceramics: cracks, voids, and inclusions [21-23] which leads to a reduction in the fracture strength. Forming ceramics into highly complex shapes and interconnected porosities with high precision are, therefore, nearly impossible when using traditional ceramics manufacturing and processing technologies.

Only a few fabrication approaches for accessing miniaturized ceramic features have been reported, which typically either on additive manufacture (AM) of ceramic particles in polymer resin followed by sintering, or nanoscale coatings on top of a pre-made microstructure template[24, 25].

The former approach, AM with particle-loaded polymers, allows for the fabrication of macro- and micro-lattices comprised of solid ceramic strut members. The particle process has major drawbacks including light scattering and limited loading of dispersed ceramic particles, which results in the final material likely possessing inevitable porosities and a large population of flaws. As such, the resolution and mechanical properties are significantly compromised. The template approach using nanoscale coating usually starts with AM-made polymer micro or nanolattices from projection micro-stereolithography or two-photon-lithography[26-28]. Atomic layer deposition (ALD), a highly conformal deposition process is then used to coat uniform layers of ceramic with thickness control at the atomic level, producing composite micro-features of polymer scaffold and nanoscale ceramic coating. The composite structures can be cut open for removal of the polymer template by etching or thermal treatment to leave behind hollow ceramic shell-like structures [29]. The advantage of the templating approach is the uniform, conformal coating of ceramic and the nano-meter thickness control of the ceramic. However, due to the nature of this templating approach, the resulting ceramics are only limited to a shell-like morphology, making it impossible to produce arbitrary micro-scale ceramic features. Additionally, the slow rate of the ALD process normally on the order of nanometers per hour makes scaling impractical. Glassy carbon lattices were previously fabricated by additive manufacturing followed by a carbonization process[30, 31], achieving a high strength-to-density ratio. However, carbon is not stable at high temperature in open atmosphere, and hence has limited high-temperature applications.

New advances in AM of ceramics have taken advantage of ultraviolet (UV)–curable preceramic monomers, which upon heat treatment, are directly converted into polymer-derived ceramics (PDC) with virtually no porosity[32]. Preceramic monomers rely on inorganic polymers such as carbosilane, siloxane or silazane, bearing UV-curable active functional side-groups such as thiols, vinyls or epoxides. UV crosslinking during the AM processes converts these to net-shaped “green” pre-ceramics which are then converted to a ceramic by inert atmosphere pyrolysis at high (~1000°C) temperature, driving off volatile organic species (e.g. H_2O, CO_2, CH_4, etc.). To date, complex shaped cellular ceramic parts have been produced with virtually no defect porosity using commercially available 3D printers, achieving feature sizes in the range of hundreds of micrometers[32, 33]. Further reduction of the feature size and improve resolutions have not been reported and still presents challenges. As the volatile organic species are driven off during the process, there is the potential for void formation and cracking in ligaments especially for thick sections. The pre-existing defects or flaws during the fabrication of the preceramic polymer lattice also affect the final quality of the 3D printed ceramic.

From a structural perspective, the benefit to reduce the controllable feature size in ceramic is the promise of incorporating size effects and precisely defined 3D architected topologies, which gives rise to the so-called new class of “architected metamaterials”. Architected metamaterials are typically produced using the template ALD approach, motivated to attain nanoscale hollow shells. Through reducing the coating thickness, a two-fold increase in strength was observed for the lower thickness compared to larger thickness as a result of the size effect. While the template ALD process allows for an indirect approach to capitalize on the size effects through reducing coating thickness, the most notable limitations are the challenge of rigorous control of structural integrity from the combined coating and post-etching process and the limited core-shell morphologies.

This study seeks to move beyond the limitations of the templated ALD approach, by improving the resolution of PDC ceramic into the size effect strengthening regime. In this work, we describe the fabrication and mechanical properties of solid high-temperature architected metamaterials with micro-sized thickness and provide direct observation of the size-dependent mechanical properties as a result of the reduction of individual free surface ligament volume. These high-temperature PDCs are produced by a high-resolution large-area projection micro-stereolithography with a resolution of several microns. The preceramic monomers are cured with near-UV light, forming 3D polymer structures that can have sub-10 μm features (the gear teeth in and complex cellular architectures spanning from 10μm scale to several centimeters. These polymer structures can be pyrolyzed to a silicon oxycarbide (SiOC) components with uniform shrinkage and virtually no porosity. The demonstrated approach allows for creation of architected topologies with feature sizes from a few micrometers to milimeters, allowing for a full investigation of the volume size effects. The associated micro-scale size-dependent mechanical properties of the 3D architected PDC metamaterials are investigated. Compression tests are performed on the as-fabricated metamaterials of 3D octet and cuboctahedron with relative densities ranging from 1% to 22 %. The experimental results and analysis indicate that the strength of the parent solid estimated from that of the metamaterials increases as the decrease of relative densities approaches 1%. This effect came from the decreasing of strut thickness while keeping the strut length a constant. We then expanded the investigation of the size-dependent strength as a function of the free unit volume of single strut members. This size-dependent strength of parent solid is discussed using Weibull analysis. It is envisioned that the utilization of the size-dependent mechanical property enabled by the high-resolution additive manufacturing can improve the reliability of these architected structural materials and accelerate the application of the 3D micro-architected high-temperature ceramic for engineering applications.

1.2.2 Fracture toughness of mechanical metamaterials

Three-dimensional, stretch-dominated architected metamaterials, which comprise a periodic repetition of a unit cell encompassing an ordered arrangement of highly connected struts, have demonstrated near linear scaling of both stiffness and strength with density[24, 25, 30], as well as remarkable optical [34, 35] and thermal properties [32, 36, 37]. Advanced fabrication techniques, such as projection microstereolithography [26] and two-photon lithography [38], have led to a realization of metamaterials with constituents ranging from polymeric [24] to metallic [27] to high-temperature ceramic materials [32]. Moreover, it has been demonstrated that incorporation of fractal-like, multi-scale hierarchical micro-architectures, with nanoscale features, can achieve orders of magnitude higher strength and stiffness than stochastic aerogels and foams [27] as well as high compression and tensile recoverability in metamaterials comprised of brittle constituents [27, 39].

Ultimately, as material processing and manufacturing capabilities improve to enable the production of these metamaterials at size scales relevant to real-world structural applications, the performance of these metamaterials will be limited by their defect sensitivity. While much work has been done to investigate the modulus and compressive behavior of these low-density metamaterials [27, 39-43], experimental measurements of their fracture and damage tolerance have been sparse[44], mainly limited by the inability to manufacture sufficiently large samples.

Taking advantage of a large-area high-resolution projection stereolithography system, we present the first experimental measurements and numerical analysis of different crack initiation mechanisms in periodic metamaterials with varying relative densities (viz. the density ratio between the metamaterial and its parent material) and developed a 2-parameter fracture model to describe the fracture toughness of micro-architected metamaterials.

1.3 Multi-functional metamaterials

For many applications, it is essential to create metamaterials with multiple functional properties including mechanical, piezoelectric, electromagnetic, shape-memory, thermal and acoustic properties, etc. The aim of multi-functional metamaterials is adding functionality beyond the novel mechanical properties including high stiffness and strength. The design of these multi-functional materials combines the rationally designed micro-structures with functional materials. In this section, several research studies are reviewed for multi-functional metamaterials and piezoelectric metamaterial is used as an example for the development of multi-functional metamaterials.

Xu, et. al elucidated how to resolve the trade-off between the coefficient of thermal expansion (CTE) and structural efficiency and demonstrated a lightweight bi-material thermal metamaterial that not only is stiff and strong but also has a large range of tunable CTE. The authors demonstrated two distinct mechanisms of thermal expansion shown in a tetrahedron and combined these into an octet-truss lattice to generate tunable CTE values, including negative, zero or positive, without loss in mechanical properties. The demonstrated architectures can be applied to a broad array of applications, including antennas, aerospace systems, etc.

Zhang, et. al printed biocompatible and biodegradable composite shape-memory structures whose shape memory behaviors are triggered by the magnetic field. The authors investigated the shape memory effect of the printed structures experimentally. The printed shape memory lattices can be utilized for potential healthcare and biomedical applications.

Yu, et. al demonstrated stimuli-responsive acoustic metamaterials that can extend the 2D phase space to 3D through rapidly and repeatedly switching signs of constitutive parameters with remote magnetic fields. These metamaterials contain magnetoactive lattice structures and their effective modulus can be reversibly switched between positive and negative within controlled magnetic fields. These metamaterials can have a great number of applications for remote, rapid and reversible modulation of acoustic transportations, refraction, imaging and focusing on subwavelength regimes.

In this work, a piezoelectric metamaterial with arbitrary piezoelectric coefficient tensor is reported and manufactured. The design was implemented by additively manufacturing free-form piezoelectric nanocomposites with complex architectures. The resulting voltage response of the activated piezoelectric metamaterials at a given mode can be selectively suppressed, reversed or enhanced with applied stress. Additionally, these electro-mechanical metamaterials achieve high specific piezoelectric constants and tailorable flexibility with only a fraction of the functionalized solid. The strategy reported here can be applied to create the next generation of intelligent infrastructure, which can perform a variety of structural and functional tasks, including simultaneous impact absorption and monitoring, 3D pressure mapping, and pressure directionality detection.

The direct piezoelectric constant correlates the electric displacement of a material with an applied stress[45-47]. Owing to the ability in converting mechanical to electrical energy and vice versa, piezoelectric materials have enjoyed widespread applications in pressure sensing[48, 49], ultrasonic sensing[50, 51], actuation[52, 53], and energy harvesting[54, 55]. The piezoelectric charge coefficient of piezoceramics, piezocomposites, and the corresponding foams are dictated by their intrinsic crystallographic structures and chemical compositions[56], resulting in common coupling modes of operation[57]. Additionally, their intrinsic microstructures are strongly coupled with other physical properties including mass densities and mechanical properties[58]. Chemical modification such as doping[59, 60] has been introduced to alter the piezoelectric constants in certain directions by altering the crystallographic structures, but their design space is restricted by the limited set of doping agents[61]. It also comes at the cost of other coupled physical properties including mechanical flexibility and sensitivity[62, 63]. While approaches including casting and templating techniques have been utilized to produce piezoelectric foams[64, 65] that showcase the potential for reduced mass densities and improved hydrostatic figures of merits, their piezoelectric coefficients, described by a square foam model[66], are largely limited by the intrinsic crystalline orientation and only occupy a narrow bandwidth within the piezoelectric anisotropy space.

Here we report a different set of concepts in which a wealth of direct piezoelectric responses can be generated through rationally designed piezoelectric architectural units and realized via additive manufacturing of highly sensitive piezo-active lattice materials. The idea begins by designing families of 3D structural node unit assembled from parameterized projection patterns, which allows us to generate and manipulate a set of electric displacement maps with given pressure, thereby achieving full control of piezoelectric constant tensor signatures. These unit cells are then tessellated in three-dimensions, forming metamaterial blocks that occupy vast piezoelectric anisotropy design space, enabling arbitrary selection of coupled operational mode. Upon polarizing the as-fabricated piezoelectric material, we demonstrated that the piezoelectric behavior in any direction can be selectively reversed, suppressed or enhanced, achieving distinct voltage response signatures with applied stress.

To implement this concept, we prepared functionalized lead zirconate titanate (PZT) nanoparticle colloids. These nanoparticles are then covalently bonded with entrapped photo-active monomers. These concentrated piezoelectric colloids are subsequently sculpted into arbitrary 3D form factors through high-resolution additive manufacturing. The building blocks with designed piezoelectric signatures could be assembled into intelligent infrastructures to achieve a variety of functions, including force magnitude and directionality sensing, impact absorbing and self-monitoring, location mapping, without additional sensing component. These free-form PZT nanocomposite piezoelectric metamaterials have not only achieved high piezoelectric charge constant and voltage constant at low volume fractions but also simultaneously possesses high flexibility, which is not attainable through piezoelectric foams or polymers. This study paves the way for a new class of rationally designed electro-mechanical coupling materials, suggesting many possibilities to move structural metamaterials[67, 68] towards smart infrastructures.

1.4 Research goal and formulation of the research framework

My research goal is to develop novel additive manufacturing and processing methods that exploit 3D micro-architectures, functionalities and feature sizes, resulting in the creation of multi-functional systems.

To achieve my research goal, the research framework was formulated, as shown in Fig. 1-3. I started with developing additive manufacturing processes capable of fabricating large-scale micro-architected materials with complex 3D topology and a broad range of feature sizes. Then I investigated the structural properties enabled by micro-scale feature sizes and scalability. On top of that, I developed AM techniques incorporated with functional cues and electronics. These fabrication capabilities extended my research to the creation of multi-functional materials with embedded electrodes and investigation of new opportunities enabled by 3D printed multi-functional materials.

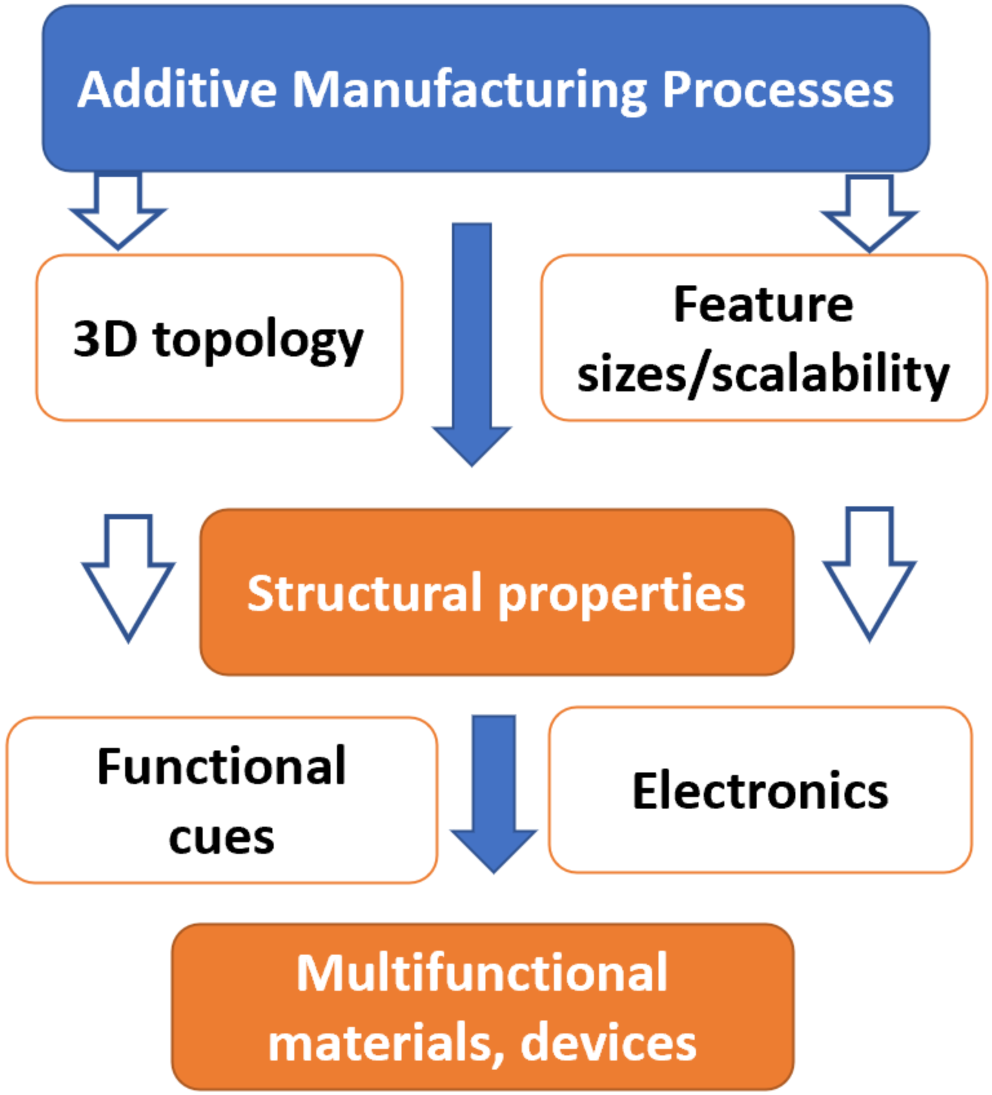

Figure 1-3 Research framework formulation

1.5 Research questions

The primary research questions for the dissertation are stated as follows and the response to each research question are shown in the following Chapters.

Research Question 1 How to enable large area AM with multi-scale features? (Chapter 2)

Research Question 2 How 3D topology, feature size and scalability impart structural properties? (Chapter 3)

Research Question 3 How to develop new AM processes to create multi-functional materials with embedded electronics? (Chapter 4)

Research Question 4 What are the new opportunities enabled by 3D printed multi-functional materials? (Chapter 5, 6 and 7)

Chapter 2 Large-area high-resolution stereolithography system (LAPμSL)

This chapter presents the set-up and calibration of the LAPμSL system. The system configuration is first introduced, and the fabrication capability is demonstrated with representative samples with multi-scale features. The second and third sections investigated the factors affecting curing depth and the overlap design of the sub-images within the exposure of a single layer. The objective of all these calibrations is to achieve optimal printing results. This technique enables the fabrication of structures with features down to the sub-10μm scale and overall size up to hundreds of millimeters, which is particularly suitable for fabricating micro-architected metamaterials with large volumes that can be employed in a broad array of real-world applications.

2.1 System description

The schematic of the LAPμSL system is shown in Fig. 2-1. The 3D models were first built using a custom code and then sliced into 2D patterns. These 2D patterns are sequentially transmitted to a spatial light modulator, which is illuminated with UV light from a light-emitting diode (LED) array. Each image is projected through a reduction lens onto the surface of the photosensitive resin. The exposed liquid cures, forming a layer in the shape of the 2D image, and the substrate on which it rests is lowered to reflow a thin film of liquid over the cured layer. The image projection is then repeated, with the next image slice forming the subsequent layer. In order to increase the resolution, the layer thickness during the 3D printing process must be well controlled. Experiments were conducted to study the effect of polymerization depth against light power projected onto the liquid surface, demonstrating the reliable printing layer thickness control below 10 micrometers.

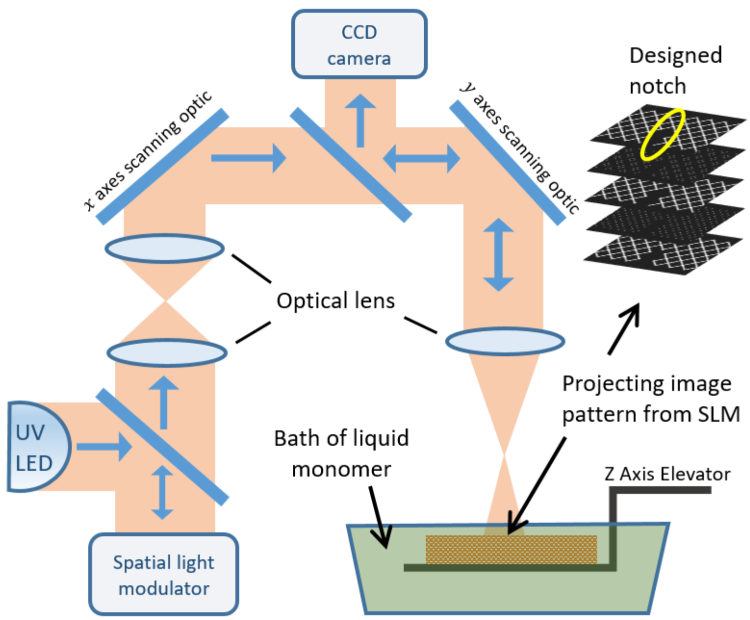

Figure 2-1 Schematic of the LAPμSL system

To further expand the scalability of the architected metamaterial and examine the size effects under a wide range of structural feature size control, the spatial light modulator is coordinated with an optical scanning system to produce large-scale parts with microscale resolution. As the mirrors scan in both axes, 2D patterns are reflected onto a new area next to the previously exposed area. The pattern change on the projector is coordinated with the scanning rate of the scanning mirror system. A customized focusing lens is used below the scanning optics to project the image onto the liquid surface. The frame is updated as the image is moved via the scanning optics to effectively create a continuous image in the photosensitive material. As this scanned image is much larger than a single image of the projector, it enables small feature sizes over a large area. This technique allows the fabrication of polymer or ceramic parts, hundreds of millimeters in size, with multiscale 3D architected features down to the $10\,\mu m$ scale (Fig. 2-3), which is uniquely suitable for fabricating lattice materials with a broad range of feature sizes.

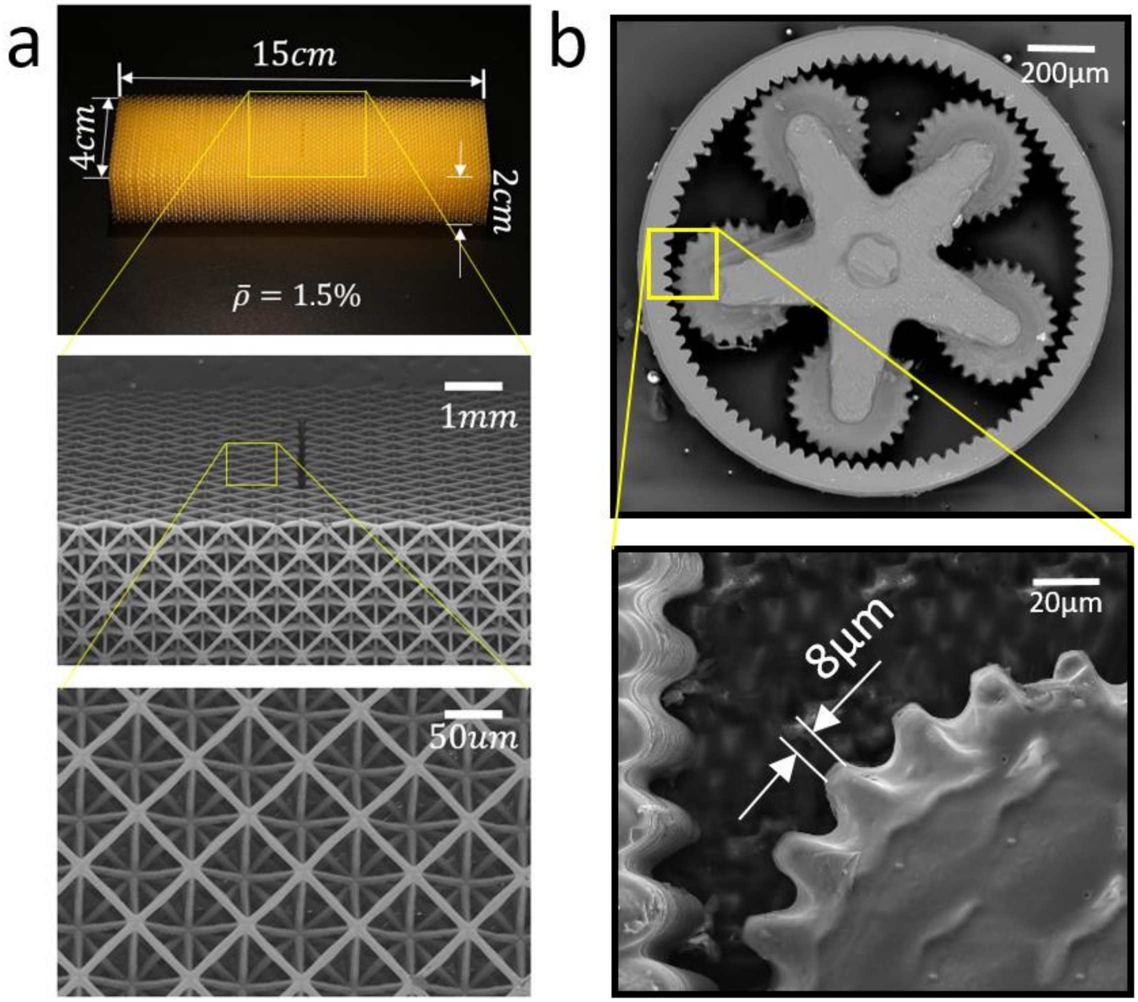

Figure 2-2 a) Optical image and scanning electron micrograph with different magnifications of an octet-truss lattice with a through crack. b) Scanning electron micrographs with different magnifications for a planet gear set.

2.2 Control of curing depth

Liquid resin compositions used for stereolithography usually consist of liquid monomer, photoinitiator and passively absorbing dye. The photoinitiator will release radicals when exposed to UV light. Solidification of the liquid monomer occurs as a result of cross-linking when it reacts with radicals within the preceramic monomers. Passively absorbing dye such as Sudan is used for absorbing the ultraviolet light to well control the curing depth of the liquid monomer. We characterized the working curves of the preceramic monomer through optimization of the photo-absorber, vinyl-thiol siloxane as well as the addition of the stabilization quencher. The working curve equation [69] is used to describe the curing depth of the preceramic resin, C_d, in a form of,

$$C_d = \frac{1}{\alpha} \ln \left(\frac{\alpha_I E}{E_c}\right) \qquad (2-1)$$

where $\alpha = \alpha_I + \alpha_D$ is the resin absorption coefficient, α_I is the absorption coefficient of the photoinitiator, α_D is the coefficient of the passively absorbing dye, E is the actual incident energies and E_c is the critical incident energy needed for curing, in units of mJ/cm^2.

To characterize the polymerization depth of a free layer, an array of overhanging bridge structures was fabricated with an array of photon energy (Fig. 2-3, inset). Each bridge layer represented one polymerization layer, and the mean thickness of a given layer was taken to be the polymerization depth. Fig. 2-3 shows the variation of polymerization depth as a function of total exposure energy (mJ/cm^2) received by the liquid resin (pre-ceramic resin as an example, all other resins shown in this report follow the same calibration procedure). The results indicate that the polymerization depth is linearly proportional to the natural logarithm of UV exposure energy, which is in good agreement with the numerical model. The experimental results confirmed the needed exposure energy for reducing the polymerization depth which is needed for reliably creating final feature size below 10 μm.

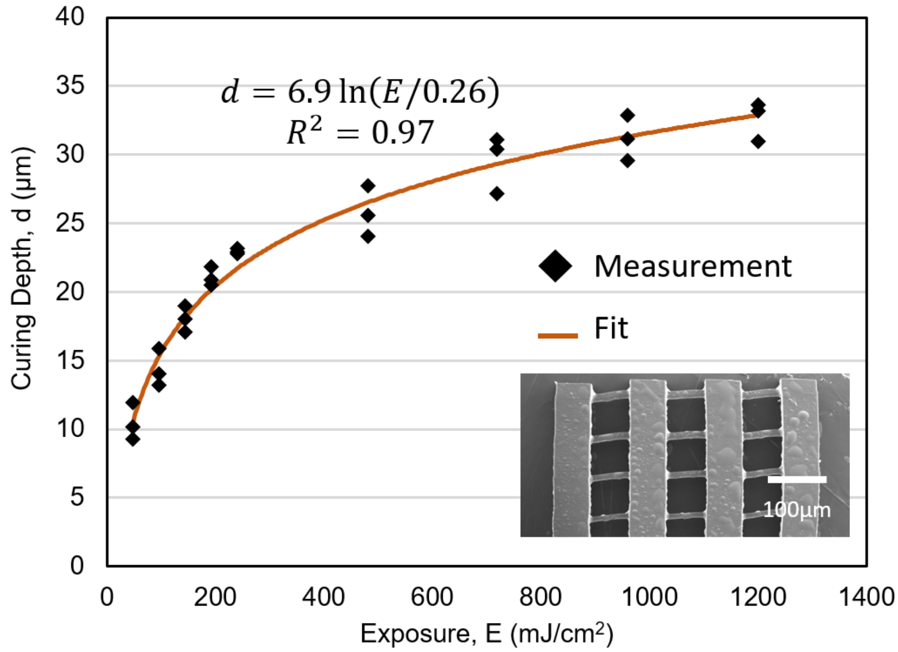

Figure 2-3 Photo flux versus polymerization depth. The curing depth increases linearly with natural logarithm of exposure energy.

2.3 Image overlap adjustment method

For the large area structure printing, the stitching between images' boundaries affects the printing quality significantly. Fig. 2-4 shows the connection between two images. In (a) there is a big gap between the two printed images, while in (b) the two images overlap too much. The consequence of the disconnected images is two structures separate from each other. And for the overlap situation, the two images form a structure, yet since the overlapped parts are exposed twice, the structure size is not uniform. To minimize the overlapping effect, the slicing pattern was also designed to have an overlap and the overlapped area contains a gray area to reduce the overexposure. With the gray area, the light intensity of the overlapped area is half of the rest sub-projection areas. Since the scanning mirrors are controlled by a linear actuator. The motion of the projection area is linearly correlated with the pixel number in the projection area. The overlap distance that's input into the actuator was calculated to be equal to the overlap distance in the projection image.

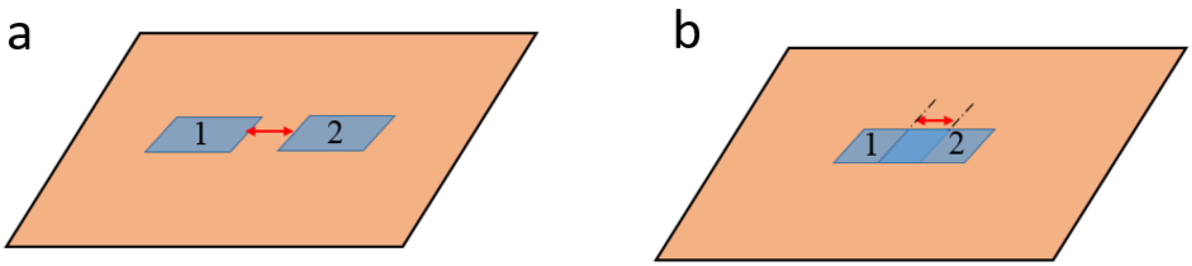

Figure 2-4 Connection between two images. (a) Two structures are separated. (b) Two structures overlap.

2.4 Continuous exposure enabled by continuous scanning

Although the proposed method can enlarge the printing area of projection stereolithography, the speed of the process is slow since there is no exposure when the optics move. The printing time for each layer, T_{layer}, can be calculated by

$$T_{layer} = T_{coat} + n^2 \times T_{exposure} + (n^2 - 1) \times T_{move}$$

where T_{coat} is the resin recoating time for each layer, $T_{exposure}$ is the exposure time for each printing area and T_{move} is the stage moving time. To improve the printing speed, a continuous exposure method was developed to increase the printing speed by synchronizing the stage motion and exposure which are corresponding to $T_{exposure}$ and T_{move} respectively.

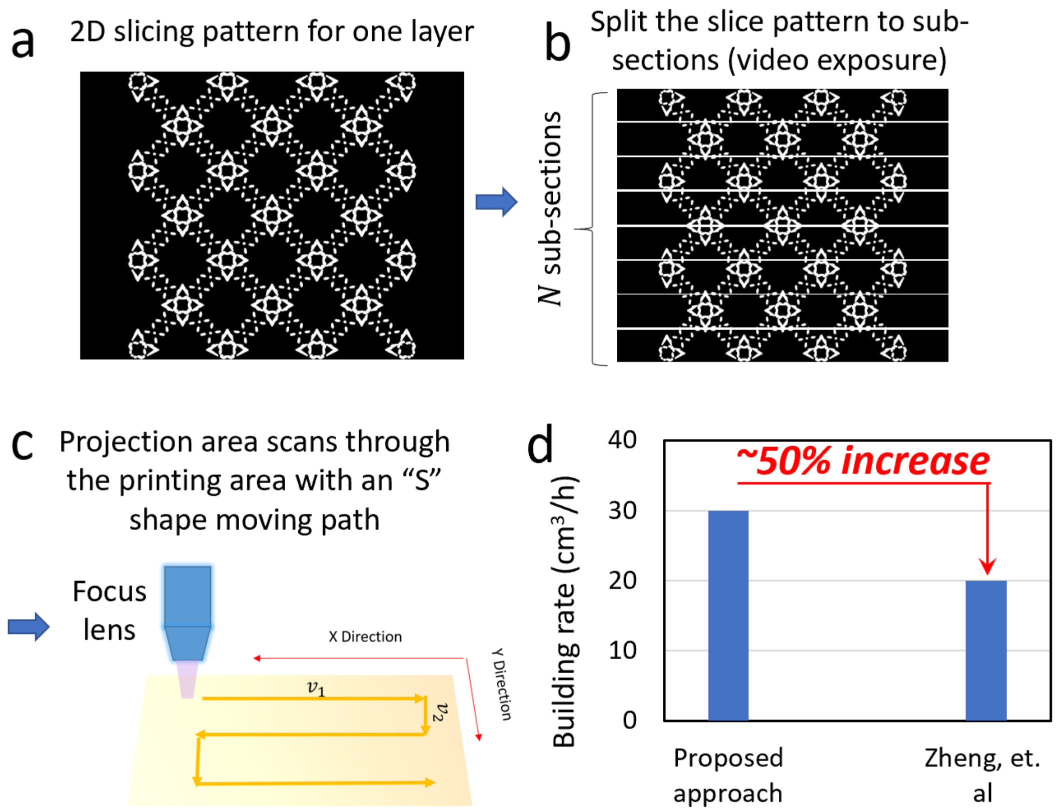

Figure 2-5 (a-b) Schematic of the continuous exposure method (d) Benchmark the printing speed of the continuous exposure method with the state-of-art large area projection micro-stereolithography.

Before printing, we first add a buffering region for motor acceleration to get a steady speed while curing (Fig. 2-5a) and then we split the projection area into sub-sections (Fig. 2-5b) and cure the resin with a video rather than sub-patterns (Fig. 2-5c). Fig. 2-5d shows the building rate of the proposed approach and a state-of-art LAPuSL method. The building rate is calculated based on the printing time of a 5cm3 lattice with 20um resolution. With the proposed method, the building rate of the LAPuSL system outperforms the state-of-art scanning stereolithography[27] by over 50%. The new LAPuSL system is a unique method to fabricate metamaterials with micro-scale architectures and large volumes. It paves the way to the characterization and application of metamaterials in more practical scenarios.

Chapter 3 Application of the LAPμSL system on mechanical metamaterials

In this chapter, the size-dependent mechanical properties of 3D architected ceramic metamaterials (Section 3.1) and the fracture toughness behavior of micro-architected metamaterials (Section 3.2) were investigated.

The LAPμSL system is capable of fabricating multi-scale features, making it possible to create lightweight structural materials with feature sizes from a few micrometers to hundreds of millimeters. Section 3.1 investigated the size-dependent properties of architected high-temperature ceramics via the LAPμSL system. We found that these high-temperature architected ceramics of identical 3D topologies exhibit size-dependent strength influenced by both strut diameter and strut length. Weibull theory is utilized to map this dependency with varying single strut volumes. These observations demonstrate the structural benefits of increasing feature resolution in additive manufacturing of ceramic materials.

Additionally, the LAPμSL system is capable of fabricating metamaterials containing millions of unit cells, providing a unique experimental platform to study the fracture and damage tolerance of metamaterials. Here we additive manufactured stretch-dominated architected metamaterials with pre-defined embedded crack, where the size of the unit cells become sufficiently small compared to the flaw dimensions. Section 3.2 elucidated the emergence of fracture toughness as a material property in architected metamaterials, which is found to be a property largely influenced by the elastic instabilities of struts members and T-stress, A design map based on a 2-parameter fracture model was developed to guide the design of failure modes in micro-architected metamaterials.

3.1 Size-dependent mechanical properties of 3D architected high-temperature ceramic metamaterials

3.1.1 Unit cell structure selection and lattice design

Due to the different arrangements of cell struts, cellular structures can deform by either the bending or stretching of the cell struts and can be classified into bending-dominated or stretch-dominated structures, respectively. Maxwell [70] proposed an algebraic rule setting out the condition for a pin-jointed frame of b struts and j frictionless joints to be both statically and kinematically determinate. In three dimension the condition is

$$M = b - 3j + 6 = 0 \qquad (3-1)$$

If its joints are locked (rigid joint) and $M > 0$, its members carry tension or compression when loaded, and it becomes a stretch-dominated structure. A stretch-dominated unit cell structure is substantially more mechanically efficient than its bending-dominated ($M < 0$) counterpart, because slender structures are much stiffer when stretched than when bent. Thus, we choose stretch-dominated structures to fabricate architected polymer-derived ceramic (PDC) metamaterials.

The octet-truss unit cell, a stretch-dominated structure first proposed by Fuller [71], is used in this study. Octet-truss structure is a method for filling 3D space with a structurally efficient truss structure of arbitrary cell size (Fig. 3-1a). The cell has a regular octahedron as its core, surrounded by eight regular tetrahedra distributed on its faces. All the strut elements have identical aspect ratios, with 12 solid rods connected at each node. The cubic symmetry of the cell's f_{cc} structure generates a material with nearly isotropic behavior. When made from high specific modulus and strength materials, the octet-truss lattice is, therefore, a weight-efficient, stress supporting cellular topology. The cuboctahedron unit cell, composed of a periodic arrangement of octahedra, is also used in this study (Fig. 3-1b). While it is not fully rigid, the octahedral sub-units are rigid. It is therefore defined to be a periodically rigid topology [72].

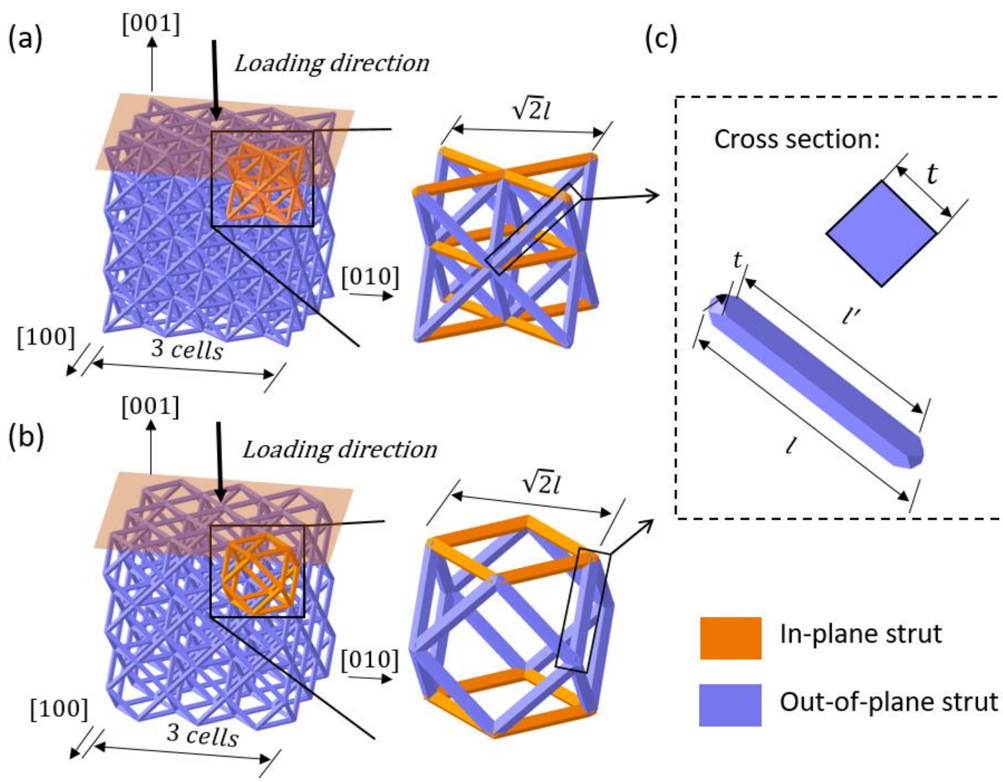

Figure 3-1 Computer-aided design models for a) the octet-truss lattice, unit cell, b) the cuboctahedron lattice, unit cell and c) their struts.

The struts of the unit cells are designed to have a square cross-section, thickness, t, and node-to-node length, l (Fig. 3-1c). The unit cell size equals $\sqrt{2}l$ and the cubic lattices, consisting of

$3 \times 3 \times 3$ unit cells, are constructed by periodic packing of these two kinds of unit cells along their three principal directions, respectively. Here, we fabricated samples with relative densities ranging from 1% -22%. The relative densities were tuned by modifying the aspect ratio (t/l) within the periodic unit cells. More details about the relative density calculation are illustrated in the next section. Among all these lattices, the length, l, of each strut and hence the overall dimension of the samples has been kept a constant. In addition, octet-truss lattices with the same relative density (same aspect ratio, t/l) but varying cell size, i.e. strut thickness and strut length, are also fabricated and tested.

3.1.2 Relative density design

The analytical expressions for the relative density of octet-truss and cuboctahedron lattices are derived. For low relative density, the higher order term of strut aspect ratio, i.e. t/l, due to the nodal effect, is negligible; as the strut aspect ratio increases, the nodal effect plays a more significant role in relative density calculation and neglecting this effect renders noticeable overestimation of the relative density. For octet-truss and cuboctahedron lattice with square cross-sections, the node is considered as a cube and hence the volume of the node is taken as $V_{node} = t^3$. The end-to-end length (distance between the edges of two nearest nodes as shown in Fig. 3-1c) is defined by $l' = l - t$, where l is typically called the node-to-node strut length. By considering a repeating unit cell, the relative density accounting for the nodal effect is then expressed as

$$\bar{\rho} = \frac{\rho}{\rho_s} = \frac{\mathrm{N}_{strut} t^2 l' + \mathrm{N}_{node} t^3}{\mathrm{L}^3} \qquad (3-2)$$

where N_{strut} and N_{node} are the number of struts and nodes within a repeating unit cell; L is the edge length of a repeating cubic unit cell.

Considering the cases of octet-truss and cuboctahedron unit cells, N_{strut} is 24 and 12 for octet-truss and cuboctahedron unit cell, respectively; N_{node} is 4 and 3 for octet-truss and cuboctahedron unit cell, respectively; L equals to $\sqrt{2}l$. Therefore, the relative density expressions are given by

$$\bar{\rho}_{octet} = 6\sqrt{2}\frac{t^2}{l^2}\left(1 - \frac{5}{6}\frac{t}{l}\right) \qquad (3-3)$$

$$\bar{\rho}_{cubo} = 3\sqrt{2}\frac{t^2}{l^2}\left(1 - \frac{3}{4}\frac{t}{l}\right) \qquad (3-4)$$

where $\bar{\rho}_{octet}$ and $\bar{\rho}_{cubo}$ are relative densities of octet-truss and cuboctahedron lattices with nodal correction, respectively. The corresponding expressions without nodal correction simply neglect the term in the parenthesis in Eq. (3-3) and (3-4). The discrepancy between relative densities with and without nodal correction starts to emerge when $\bar{\rho} > 20\%$ [73]. In our case, we neglect the nodal volume effect since the relative density range used for experiments is 1% ~ 22%.

3.1.3 Experimental design

The mass and volume of all the ceramic lattices are measured after pyrolysis. The relative density is calculated as the ratio between the mass and volume and compared with the designed volume fraction. The as-fabricated SiOC lattices were tested at ambient temperature in free compression along [001] direction, as shown in Fig. 3-1, at a nominal strain rate of $8 \times 10^{-4} s^{-1}$ on Instron 5944 using standard flat compression plates (T1223-1022). The peak load divided by the crosssectional area of the lattices was defined as the effective strength of the lattices. The Young's modulus was extracted from the steady slope of the stress-strain curves. The tested strength, Young's modulus of lattices and relative density of the lattices are used to plot the scaling relationship and size effect analysis in the next section.

3.1.4 Polymer-derived ceramic characterization

The pyrolysis procedure was accompanied by 37% weight loss and 34% linear shrinkage. Scanning electron microscopy (SEM) with energy dispersive X-ray analysis (EDS) was performed. The result (Fig. 3-2) shows that the sample has a composition of 20.44 atomic percent (at %) carbon, 38.6 at % oxygen and 40.96 at % silicon, or $SiO_{0.9}C_{0.5}$ The content of oxygen is similar to the previous studies, however, the content of carbon is lower and, the content of silicon is higher compared to the previous studies [32]. Previous reports have shown the significant dependence of SiOC on composition [74]. These effects can be generalized as, the more silicon carbide (SiC) like, i.e. more carbon, less oxygen, the SiOC composition becomes, the greater the mechanical properties, Young's modulus and hardness. Variation in compositions can lead to an approximate doubling in properties.

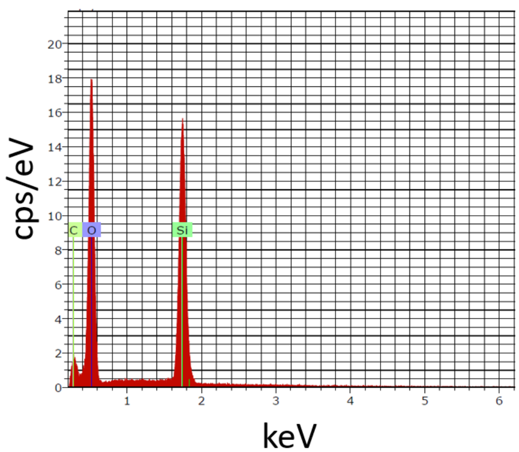

Figure 3-2 Energy dispersive X-ray analysis of a single strut inside the lattice.

3.1.5 Strength and Young's modulus scaling in high-temperature ceramic lattices

The testing results of Young's modulus and strength of both octet-truss and cuboctahedron are summarized in Fig. 3-3. The compressive strength versus relative density is plotted for each architecture in Fig. 3-3a and compared to other octet-truss lattices with different parent solids [24, 43].

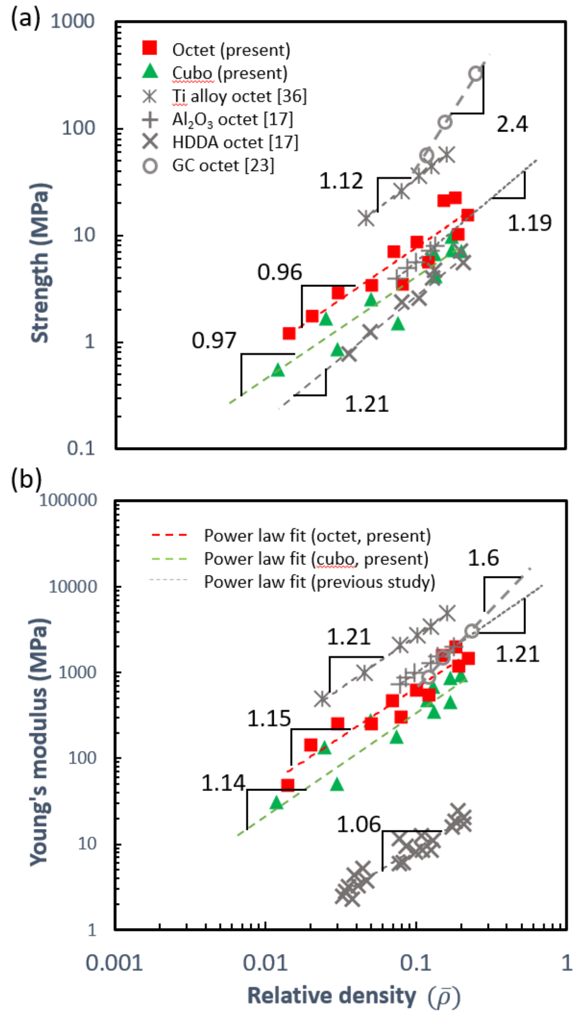

Figure 3-3 Scaling law of effective strength and Young's modulus of the octet-truss and cuboctahedron lattices. The experimental results of previous studies are shown as a comparison.

Well-developed theories[42, 43] show that on the macroscale, under uniaxial compressive loading, the compressive stiffness and yield strength of these structures theoretically show linear scaling relationships: $E/E_s \propto \bar{\rho}$ and $\sigma/\sigma_s \propto \bar{\rho}$, where E_s is the Young's modulus of the base material, σ_s is the strength of the base material. However, as indicated in Fig. 3-3a, the previously reported experimental results [24, 43] show that, under uniaxial compression, the scaling factors for stretch-dominated lattices are normally in the range of 1.06 to 1.21, or even as high as 2.4, larger than the theoretical value, since there are fabrication imperfections weakening the performance of these lattices.

Interestingly, in testing results of the PDC lattices, the apparent strength (σ) - relative density ($\bar{\rho}$) scaling in the as-fabricated ceramic lattices shows a scaling power that is smaller than 1 for both octet-truss lattices and cuboctahedron lattices, outperforming theoretically predicted scaling powers. In contrast, the obtained scaling relationship of Young's modulus (E) and relative density ($\bar{\rho}$) in Fig. 3-3b are consistent with previously reported scaling values as well as predicted by theory on stretch dominated lattices. It should be commented that the cuboctahedron lattice here is considered to be a stretch-dominated lattice for its periodic rigidity. We hypothesize that the strength of these architected lattices is influenced by a possible strong size-dependent effect as the smallest ligament becomes slender in the micro-scale range (i.e., reduction of strut size), which will be further investigated in the following sections.

3.1.6 Strut thickness dependent PDC strength

To investigate the size dependency of PDC strength, the strength of the parent solid that comprises the individual solid strut members for each sample is estimated by normalization of the effective compressive strength of the lattices with its topology dependent factor. The effective strength of cellular materials can be approximated by the first-order scaling law [75]:

$$\sigma_{eff} = \Sigma\sigma_s \qquad (3-5)$$

where Σ is a lattice topology and geometry dependent scaling factor, σ_s is the fracture strength of the base material. The scaling factor Σ, accounting for both the lattice geometry and relative density, can be calculated by

$$\Sigma = C\bar{\rho}^{\alpha} \qquad (3-6)$$

where C is a geometric parameter depending on the lattice topology as well as the loading direction, $\bar{\rho}$ is a function of (t/l), and the exponent α is 1 for stretch-dominated behavior, theoretically [41]. Based on previous studies, the experimental results of the geometric parameter, C, for octet-truss lattices cuboctahedron lattices are 0.3 and 0.16 [42, 72] for [001] direction loading, respectively.

Such that the effective strength of the lattice can be normalized by the geometric factor to estimate the strength of the individual ligament

$$\sigma_n = \frac{\sigma_{eff}}{\Sigma} \qquad (3-7)$$

σ_n can be seen as an estimation of the strength of the parent solid.

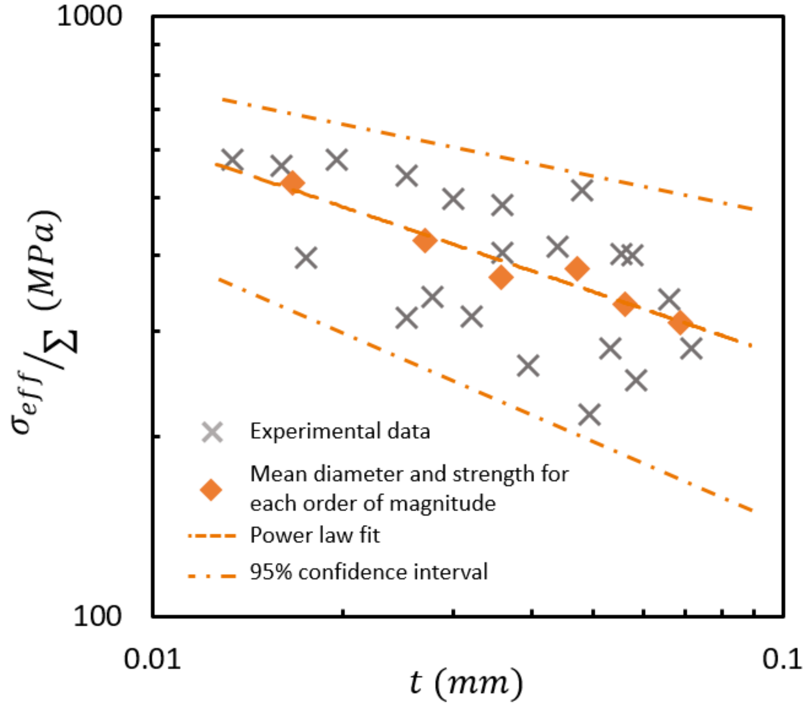

Figure 3-4 Effect of strut diameter on the normalized strength of relative density controlled ceramic lattices. The means of estimated PDC strength are calculated using each 10-micron interval for strut thickness for strut volume in order to filter the scattering of the data.

Here, as relative density reduces, the only changing parameters for both octet truss lattices and cuboctahedron lattices are strut thickness while the strut length has been kept constant. The normalized strength of the parent solid excluding all geometric factors is plotted against the only variable strut thickness in Fig. 3-4. The size-dependent mechanical property of lattices with differing relative density from Fig. 3-3a can now be visualized in Fig 3-4. The means of estimated PDC strength are calculated using each 10-micron interval for strut thickness for strut volume in order to filter the scattering of the data[76]. The strength of the PDC solid carries a power-law relationship with the strut thickness as there is no characteristic length for the brittle PDC strut [76-

[79]. A power-law fitting is applied to the calculated mean strength of the ceramic solids as a function of strut thickness and yield the following relationship,

$$\sigma_s = Dt^{-\beta} \qquad (3-8)$$

where β is the scaling factor of the strut thickness and is found to be 0.36, from our measured experimental results, while D is a constant. The normalized PDC strength increases as the strut thickness decreases, as shown in Fig. 3-4, indicating a size dependency of the strength of the PDC solids possibly due to the reduced size and number of cracks.

Previous studies also show that the strength of brittle [80-82] materials typically increases with decreasing dimensions. Based on the relationship proposed by Griffith between the fracture strength, σ_f, and the critical size of a flaw, c, for brittle materials such as ceramics[83], we know that

$$\sigma_f \propto \frac{1}{\sqrt{c}} \qquad (3-9)$$

A flaw cannot be larger than the component in which it is located. Assuming c correlates with the strut thickness, t [84]. The relationship can be written as

$$\sigma_f \propto t^{-0.5} \qquad (3-10)$$

Even though the scaling factor from our measured experimental results is lower than the value proposed by Griffith, which may be caused by the insufficient number of measurements and experiment errors, our experimental results indicate a size dependency of the strength of the PDC solids.

This size effects as a function of reduced strut thickness in density-controlled sample explain the apparent scaling law of $\sigma_{eff} - \bar{\rho}$. By combining Eq. (3-5, 6 & 8), the effective strength of the lattice can then be modified as,

$$\sigma_{eff} = CD\bar{\rho}^{\alpha}t^{-\beta} \qquad (3-11)$$

Substitute relative density expression without nodal correction into Eq. (3-11), we get

$$\sigma_{eff} = CD\bar{\rho}^{\alpha-\frac{\beta}{2\alpha}}l^{-\beta} \qquad (3-12)$$

Eq. (3-12) can be further modified as

$$\sigma_{eff} \sim \bar{\rho}^{\alpha-\frac{\beta}{2\alpha}} \qquad (3-13)$$

From Eq. (3-13) we know that the scaling between the effective strength and relative density of the lattice is reduced by a factor of $-\frac{\beta}{2\alpha}$, which is caused by the size dependency of the PDC strength. As density further reduces, this $\frac{\beta}{2\alpha}$ will further increases which will result in higher specific strength in lower density solid architected ceramic as compared to higher density samples, i.e., an apparent scaling power smaller than 1 as density decreases further.

3.1.7 Strut volume dependent PDC strength analogous to Weibull size effect

We then proceed to investigate the size strengthening effect by measuring the strength of lattices of identical relative densities, but with uniform reduction of minimal strut volumes. While the benefit of reducing the coating thickness of ceramic through atomic layer deposition have been experimentally demonstrated in previous reports by [39, 85] and explained by the weakest link theory [86], it has not been clear the role of the overall size, i.e., strut volume of each solid ligament that comprise the overall lattices. The size from the length-direction, which contributes to the surface volume of individual solid strut members, in addition to the diameter and thickness of the strut could contribute to the overall size effect of the lattice material. Here, to fully capture the size dependency of the PDC strength, we expand the study by simultaneously modifying the average strut thickness and length within the unit cells. Samples were fabricated with identical relative densities but with a serial reduction of single strut volumes. The Weibull statistical analysis is applied to interpret the relationship between strut volume and material strength.

Derived from the weakest-link-theory based on a chain model [77, 78], the risk of failure of material is given by a probabilistic expression:

$$P_f(\sigma) = 1 - \exp\left\{-\frac{P(\sigma)V}{V_0}\right\} \qquad (3-14)$$

where $P_f(\sigma)$ represents the risk of failure of a material under stress σ; V is the volume of the material and V_0 is a standardized reference volume; $P(\sigma)$ is defined as the probability of material failure under stress σ for a given material volume V. Weibull [87, 88] proposed a power-law solution for $P(\sigma)$ vanishing at a critical value of σ_c as $P(\sigma) = \left(\frac{\sigma-\sigma_c}{\sigma_0}\right)^m$, where σ_c is the critical strength below which the probability of failure is zero, for brittle material $\sigma_c = 0$ since for brittle material any tensile stress can cause brittle fracture; σ_0 is the characteristic strength at $P_f(\sigma) = 63.2\%$; m is the well-known Weibull modulus [89].

Therefore,

$$P_f(\sigma) = 1 - \exp\left\{-\left(\frac{\sigma}{\sigma_0}\right)^m \frac{V}{V_0}\right\} \qquad (3-15)$$

For the same risk of failure under two different stresses, we obtain $\frac{\sigma_1}{\sigma_2} = \left(\frac{V_2}{V_1}\right)^{\frac{1}{m}}$, which leads to the expression of nominal strength of material:

$$\bar{\sigma}_f \propto \left(\frac{1}{V}\right)^{\frac{1}{m}} \qquad (3-16)$$

In the present case, $V = t^2 l$ represents the strut volume. Volume is a function of strut thickness (t) as defined in Fig. 2.

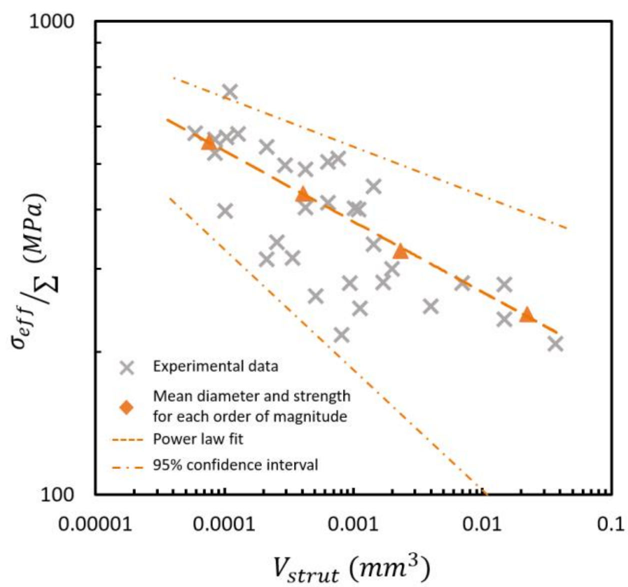

Figure 3-5 Effect of strut volume on the normalized strength of volume controlled ceramic lattices. The mean of the estimated strength was calculated using each order of magnitude for the strut volume.

According to the theorem as in Eq. (3-16), the strength of PDC relates to the strut volume by a simple power law from a statistical viewpoint as shown in Fig. 3-5, which plots the normalized PDC strength versus the strut volume (V). The mean of the estimated strength was calculated using each order of magnitude for the strut volume. The scaling power in Fig. 3-5 shows the trend of the size dependency of strength as a function of strut volume reduction over three decades: decrease of the strut volume leads to the increase of the PDC strength. For 3D architected brittle ceramic metamaterials, the failure of the metamaterials is determined by successive failure of multiple struts. The failure of an individual strut is catastrophic due to the brittle nature of PDC which suggests the applicability of Weibull analysis and weakest link theory only on the strut volume instead of the total volume of the architected material [88]. However, in order to obtain the Weibull modulus and size effect for 3D micro-architected brittle ceramic metamaterials, a non-classical probabilistic model is needed to account for structural factors, which is discussed in the next section.

3.1.8 Discussion and conclusion

This section reports the fabrication of high temperature ceramic architected metamaterials and the characterizations of the size effects derived from the solid micro-scale struts that comprise the stretch-dominated lattices. Additive manufacturing of polymer-derived ceramic had been recently reported to process virtually no porosities in as-fabricated ceramic components. This work, for the first time, extends this paradigm to the fabrication of high-temperature precision ceramics with solid micro-scale features, opening up new opportunities to capitalize on the size effects from miniaturized features and proliferate them to lightweight ceramic architected materials. A well-controlled stabilized preceramic light-sensitive monomer with UV stabilizers enables confinement of polymerization depth within 10 microns, resulting in reliable production of precision 3D ceramic components comprised of microscale solid features.

While extensive investigations have reported the stiffness and strength for a limited number of test samples [41, 42, 44] with thin-walled hollow tube ceramic, this study provides direct observations of the size-dependent strength of ceramic micro-architected metamaterials with solid strut members. The as-fabricated stretch dominated SiOC ceramic metamaterials have revealed a strong size dependency in relative densities reduced from 22% to 1%. A break-down of strength as a function of the diameter of the ligaments revealed a stronger ligament strength when the density of the lattice is reduced. This observation was corroborated by architected lattices with varying single strut volumes of identical relative densities. We conclude that these high-temperature metamaterials approximately follow a Weibull distribution of strength as a function of reduced single strut volumes.

While the present work provides insights of single strut volume on the contribution of the strength of architected metamaterials, it did not capture the size effects of architected metamaterials comprised of a very large number of unit cells, i.e., the cell number size effects. Likewise, the weakest link theory that has been used to relate to the size effects of architected metamaterials will not fully describe the scenario of large area architected metamaterials comprised of a large number of cells. This limitation can be summarized in two-folds: 1) While the classic Weibull analysis [78, 88] as illustrated by Eq. (3-15) can give insight on the probabilistic distribution of strength and "the smaller the stronger" size effects on solid ceramic architected metamaterials, it is not entirely applicable as the structural members with different orientation and position in the architectural layout may carry different stresses such that the effect of stress distribution among strut members should be taken into account[90]. 2) As indicated in the last section, the Weibull size effect originated from the weakest link theory assumes that the failure of architected metamaterials is dictated by the failure of any single strut member. This assumption holds for micro-lattices with a limited number of unit cells; it does not necessarily apply to lattices with a significantly larger number of unit cells. The actual strength extracted from the experimental stress-strain curve is determined by the successive or nearly catastrophic failure of multiple struts. In lattices with a large number of unit cells, the successive failure of struts within the metamaterial is dominated by the effective fracture toughness of the lattice materials, which gives the metamaterials resistance to crack initiation with existing flaws (i.e., breaking of a single or a few strut member) [44, 91]. The subject of the fracture toughness of architected metamaterials remains to be future topics of investigations.

It is interesting to note that the Weibull size effects also did not fully describe the size effects in recently investigated quasi-brittle ceramic lattice networks attributed to the stress distribution throughout the entire material system, which is analogous to the 3D micro-architected brittle ceramic metamaterials. A number of studies have proposed different models utilizing series coupling of elements [92] in which a number of chain models are arranged in series, instead of in parallel, to represent that a single failure of chain does not fail the entire system, in addition to local failure events of a ceramic unit cell dictated by the weakest link theory[78, 93, 94]. Previous studies show an analytical model to deal with the cellular ceramics successive failure by utilizing the homogenization method on a material system scale to consider the failure probability of small-scale constitutive elements on which the classical Weibull theory is applied. Their proposed framework may be extended to the architected ceramic metamaterials and hence involves representations at both microscale (single strut) and macroscale (lattice), could be analogous to micro- and nano-architected ceramics containing a large number of cells. Nevertheless, in order to fully capture the size effect of architected metamaterials studied in this work, future efforts will include incorporating 1) a sufficiently larger sample number (>30 at each strut volume) in order to derive the accurate Weibull modulus of the strength size effect[95]. 2) Probabilities of failure strength as a function of unit cell numbers within a metamaterial with constant single strut volumes.

We have demonstrated the additive manufacturing of precision polymer-derived ceramic components with complex, micro-scale solid features within 10 microns. The methods are based on large-area projection microstereolithography of stabilized UV sensitive preceramic monomers with precise control of structural features from $10\mu m$ scale to millimeters. To study the strength of the high-temperature silicon oxycarbide architected metamaterials, lattices with relative densities ranging from as low as 1% to 22% were fabricated and characterized through uniaxial compression. We found that at lower densities, the strength of these solid ceramic lattices benefits from the reduced strut thickness at the micro-scale, suggesting a possible strong size-dependent strength of the strut members. Weibull theory is then utilized to map this dependency with varying single strut volumes in as-fabricated lattice materials with identical relative densities. Our study provides direct observations and evidence suggesting the benefits of micro-scale structural members in improving the strength of low-density high-temperature ceramics. Through capitalizing upon the reduction of unit strut volumes within the architecture, high-temperature ceramic could achieve high specific strength with only one fraction of their solid counterparts.

3.2 Investigation of fracture toughness of micro-architected cellular materials

In a continuum elastic material, a stress distribution known as a K-field is established near the crack tip [96, 97]. Rapid, unstable crack advance will occur when this stress intensity factor $K = K_{Ic}$, where K_{Ic} is the fracture toughness of the material [98, 99]. Here we put metamaterials on equal footing with common engineering materials by establishing their equivalent K_{Ic}.

3.2.1 Fabrication and preliminary testing

Fabrication of large volume (up to 64 cm^3) samples, containing a pre-designed embedded crack and having relative densities spanning across one orders of magnitude from 1% to 10%, was accomplished using the LAPμSL system, as shown in Fig. 3-6. The samples are designed to have an embedded crack to measure the plane-strain limit. Both the crack size and lattice relative density were varied and all other parameters remain constant. The crack length, sample width, sample height, sample length and unit cell size are defined with a, W, H, B and L, respectively, as shown in Fig. 3-6.

We chose trimethylolpropane triacrylate (TMPTA) as the UV light sensitive monomer to be the parent material for the metamaterials. The key advantage of TMPTA is that it has a linear elastic-brittle tensile response, with a measured Young's modulus $E_s = 0.5$ GPa, and strength $\sigma_s = 13$ MPa, with <20% variation over three decades of strain rate.

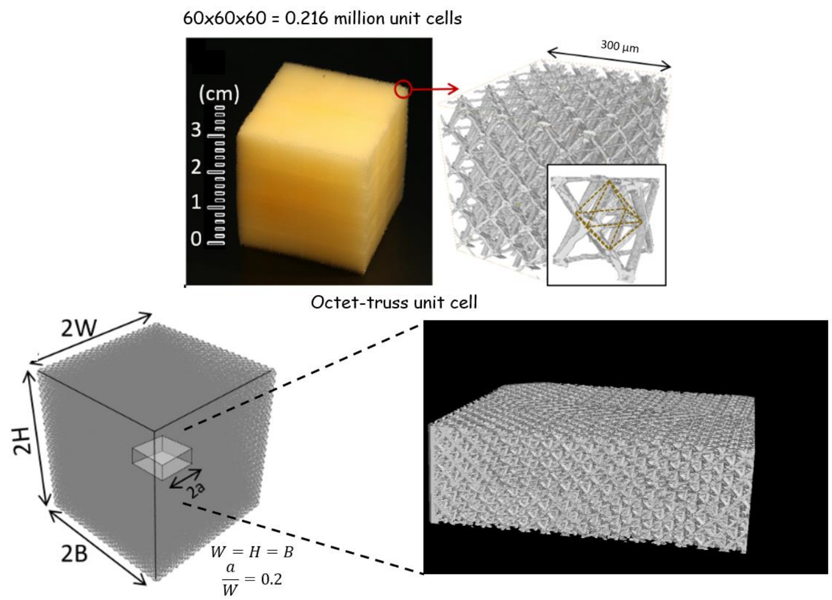

Figure 3-6 Optical image and XCT images of the fracture toughness samples with pre-designed embedded crack.

3.2.2 Crack size and relative density governs toughness

The as-fabricated samples are stretched on a tensile testing fixture with 0.05/min strain rate. The testing fixture is shown in Fig. 3-7 For samples with high relative density (>10%), the load-displacement curve is similar to that of bulk materials. However, the load-displacement curve of the $\bar{\rho} = 2\%$ sample experienced a slop change following the initial linear response, as shown in Fig. 3-7b. The fracture toughness of the tested samples is normalized by the unit cell size and base material strength and is plotted as a function of relative density, as shown in Fig. 3-7c. The results show that the measured toughness depends on relative density and crack size. Toughness for low density and high-density lattices scale differently with relative density.

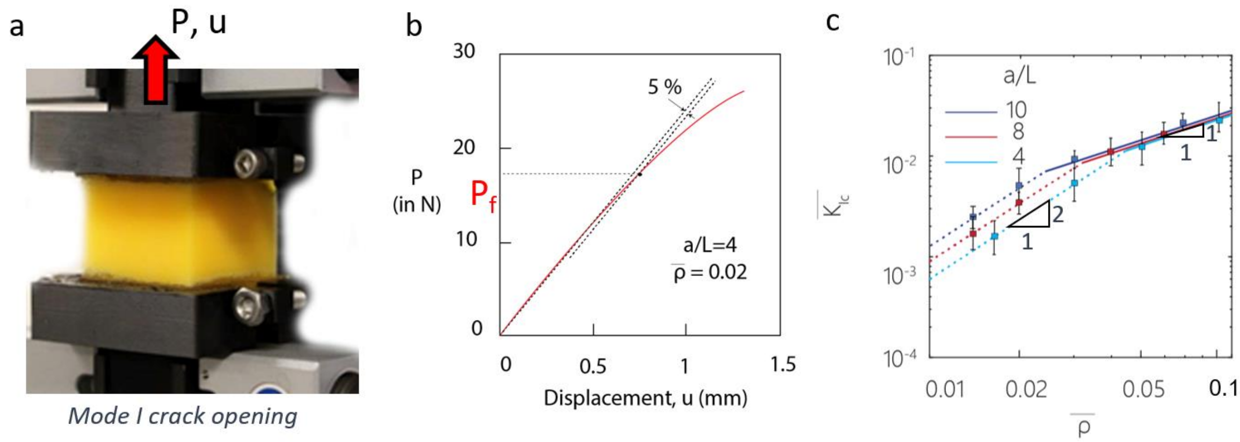

Figure 3-7 a) optical image of the as-fabricated sample loaded with tensile stress. b) Load-displacement curve of a sample with a relative density of 2%. c) The normalized effective fracture toughness as a function of relative density.

3.2.3 Observation of two unique crack-tip failure modes

After observing the different scaling of the fracture toughness of different densities, we performed in-situ XCT and observed two unique crack-tip failure modes for low-density micro-architected metamaterials: crack-tip buckling and crack-flank buckling, as shown in Fig 3-8a&b. For high-density samples, crack-tip tensile failure was observed, which is similar to the failure mode of bulk materials, as shown in Fig. 3-8c. FEA was also performed and we found excellent agreement between measurements and FE predictions. Fig. 3-9 shows the failure modes observed in FEA results with a reducing a/L ratio.

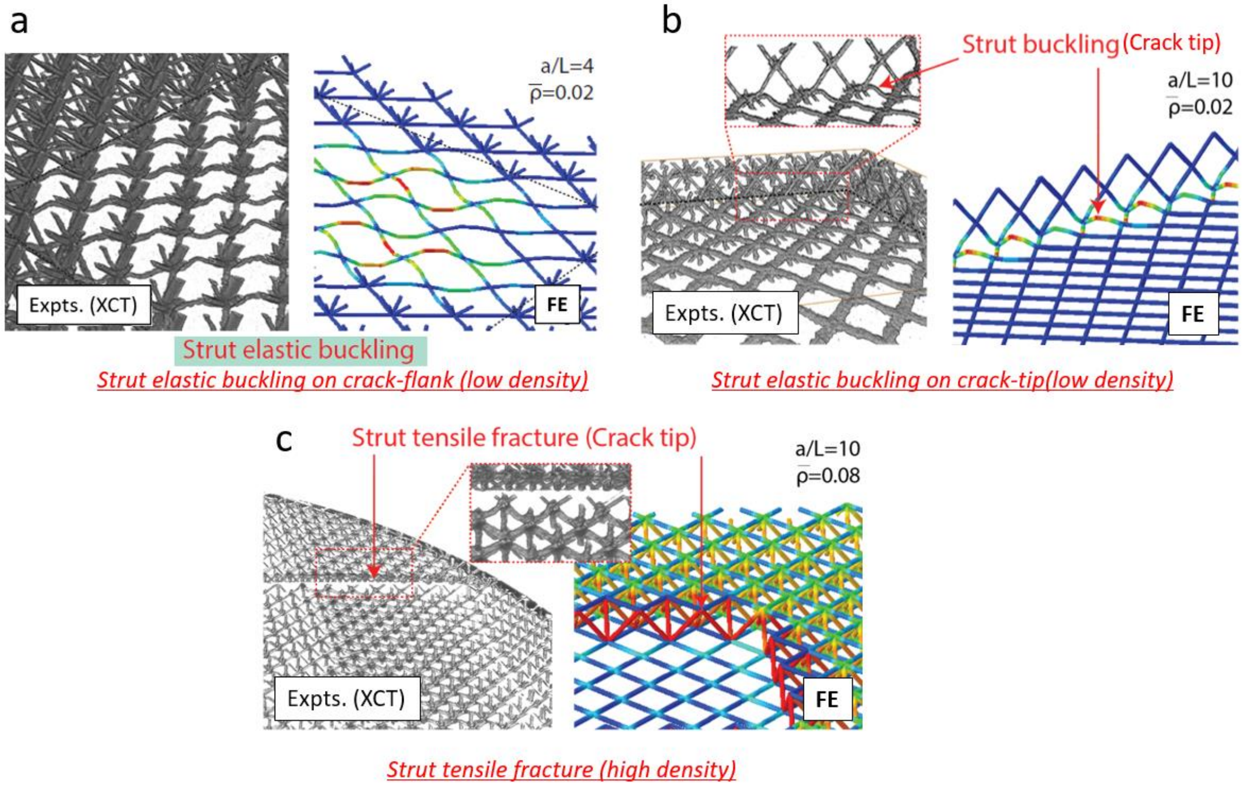

Figure 3-8 In-situ XCT images and FEA results of three different failure modes of the micro-architected metamaterials.

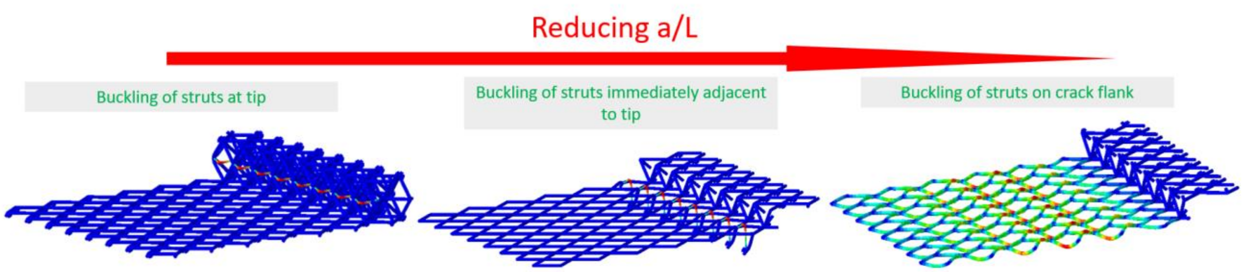

Figure 3-9 FEA results showing the failure modes of the low-density lattices with reducing a/L ratio.

3.2.4 Capturing crack size effect by T-stress

In this section, we define biaxiality, β, to capture the effect of the T-stress experimentally. The following relation connects normalized T-stress ($\bar{T}$) to normalized crack size (a/L) and biaxiality.

$$\beta \equiv \frac{T\sqrt{\pi a}}{K_I}$$

$$\bar{T} \equiv \frac{T\sqrt{L}}{K_I} = \beta\sqrt{\frac{L}{\pi a}}$$

β can be decomposed as β= $\beta_{specimen}$+ $\beta_{loading}$. $\beta_{specimen}$ =-1 (fixed) but β can be adjusted via loading in a multiaxial arrangement, as shown in the schematic in Fig. 3-10.

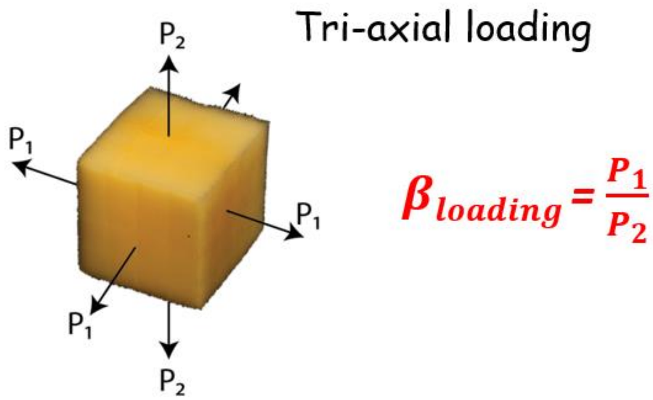

Figure 3-10 Schematic showing the varying $\beta_{loading}$.

Triaxial testings were done on samples with varying relative density and a/L ratio. The optical image and schematic for the testing fixture are shown in Fig. 3-11. During the testing, stresses are applied through several stepper motors and the experiments were performed in an X-ray chamber for capturing the in-situ XCT images during the testing and observing the failure mode of the samples.

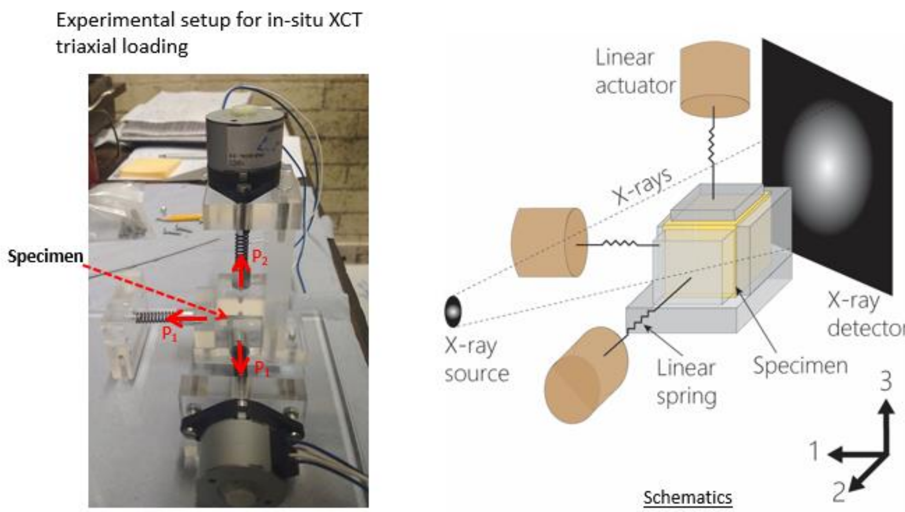

Figure 3-11 Experimental set-up of the triaxial loading test.

During the testing, β and a/L were varied independently for two different densities, and fracture toughness values were measured. The experimental results and the FE calculation are summarized in Fig. 3-12a. When β and a/L are combined into a single parameter $\bar{T}$, all data collapses into single curves confirming that the relevant parameter is $\bar{T}$, as shown in Fig. 3-12b.

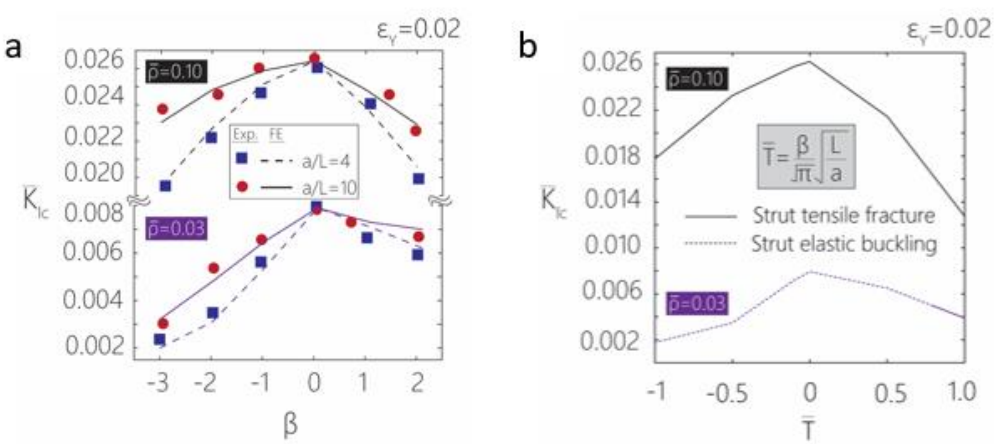

Figure 3-12 a) Normalized fracture toughness values of the architected metamaterials as a function of biaxiality with different a/L ratio and relative densities. b) Normalized fracture toughness values of the architected metamaterials as a function of normalized T-stress.

Based on the observations shown above, we proposed a failure map for designing microarchitected metamaterials using a 2-parameter fracture model, as shown in Fig. 3-13. The map captures the observed effects of crack size, relative density and loading triaxiality. The map generated in this study is for base materials with yield strain limit that equals 0.02. However, a design map for failure can be generated for all kinds of micro-architected metamaterials using the 2-parameter fracture model (K+T) for different unit cell geometries.

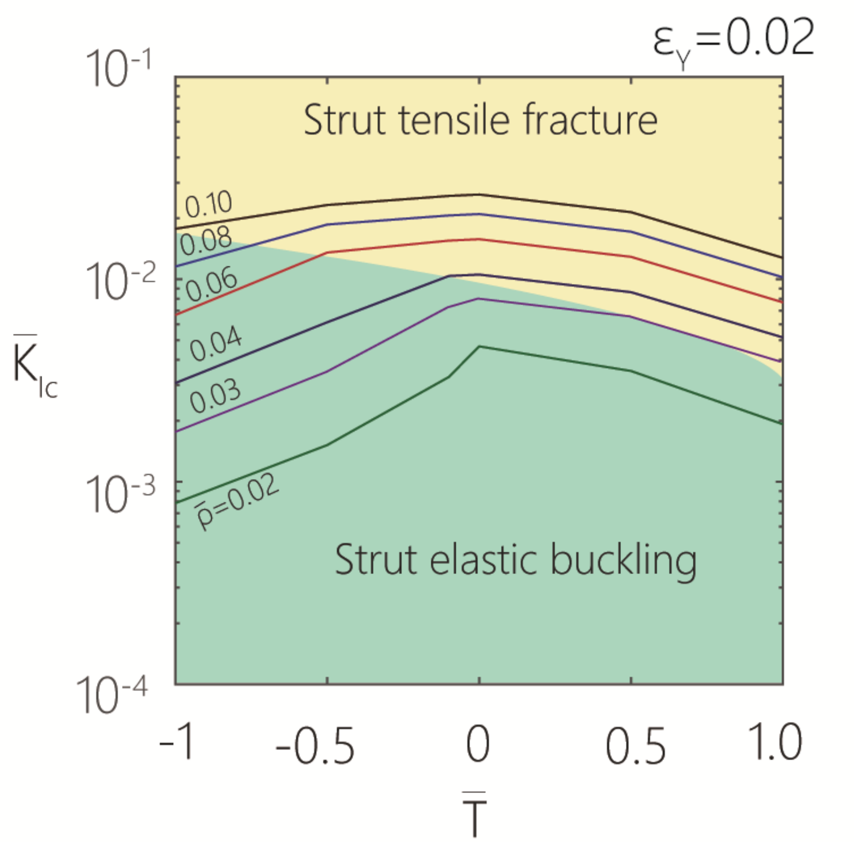

Figure 3-13 Failure maps for the fracture toughness behaviour of microarchitected metamaterials

3.3 High-temperature rapid sintering of complex 3D printed structures

3D printing techniques enable the fabrication of ceramics with complex and microscale features, which might find use in a broad array of high-temperature applications. However, there is a significant bottleneck in the ceramic 3D printing processing-property cycle, particularly for developing new materials. Formulations, printing, and sintering by traditional methods can be labor and time intensive. While printing may only take 2 hours, sintering can consume 12 to 24 hours significantly slowing the processing time. Rapid spark plasma sintering (SPS) technique is impossible for 3D printed structures, since the high pressure applied during sintering can crash the micro-architectures. The rapid high temperature (RHT) sintering technique offers a new means to quickly test a variety of ceramic 3D printing formulations for shrinkage, cracking, functional response, etc. that is not possible by traditional methods. In this section, we incorporated RHT method with the PDC shown in Chapter 3.1. In the RHT technique, the uniformly distributed high sintering temperature enables fast and high-quality sintering of the ceramics and provides a uniform shrinkage to maintain the complex structures. As a demonstration, we successfully fabricated and sintered multiple complex 3D printed structures of polymer-derived ceramics silicon oxycarbide, SiOC) with RHT technique in less than ten seconds (Fig. 3-14). The photographs indicate the uniform shrinkage (~28% linear shrinkage) of the 3D printed ceramics and well-maintained structures after RHT sintering (Fig. 3-14 a-b). By duplicating the unit cells, more complex 3D structures can be built to achieve better mechanical properties, which however introduce more challenges to maintain the fine features. As a demonstration, we successfully sintered four complex structures with different repeating units using RHT technique, and the well-maintained structures of the microstructures indicate the uniform shrinkage during rapid sintering (Fig. 3-14c-e).

In addition to the single composition of the architected ceramic materials, 3D printing possesses the ability to combine multiple materials in a complex, arbitrary 3D architecture, which opens new opportunities for fabricating high-temperature devices. For instance, the combination of giant piezoresistive and magnetic ceramic materials can form a multi-material piezoresistive-magnetic composite structure, which can be used as a magnetic flux density sensor in high-temperature environments and reads resistance changes with corresponding magnetic flux densities. Here, we fabricated multi-material honeycomb structures with aluminum (Al) doped SiOC and cobalt (Co) doped SiOC, which show giant piezoresistivity and magnetic responses, respectively (Fig. 3-14d-e). The conventional sintering method for multi-material polymer-derived ceramics suffers from the diffusion between different materials (Fig. 3-15), which results in degraded sensitivity. However, the structures sintered with RHT sintering method maintained their shape perfectly and show non-detectable cross-doping due to the short sintering time, as shown in Fig. 3-14f. To demonstrate the potential of using the multi-material part as a magnetic flux density sensor, a two-layer honeycomb structure was fabricated with Al- and Co-doped SiOC, as shown in Fig. 3-14g. The piezoresistive part (Al-SiOC) correlates the applied stress and the resistance change (Fig. 3-14h) while the magnetic part (Co-SiOC) induced stress under magnetic fields (Fig. 3-16). The piezoresistive properties of our 3D printed honeycomb structures prepared by conventional, and RHT sintering, are compared to previously reported state-of-the-art piezoresistive materials via the gauge factor, as shown in Fig. 3-14I. We see a significant increase in the gauge factor for RHT sintering, compared to conventional sintering and previous state-of-the-art materials. This establishes our rapid sintering technique as an innovative means to fabricate highly sensitive piezoresistive sensors which can be combined with magnetic materials for high-temperature magnetic field detection. At 25°C and 200°C, a permanent magnet was used to generate magnetic fields ranging from 0mT to 360mT by varying the distance to the as-fabricated sensor, while a digital multimeter was used to read the resistance of the piezoresistive section of the sensor through two copper leads attached on both ends of the honeycomb structure. The resistance change of the sensor, ΔR, and the magnetic flux density, B, are correlated by,

$$\Delta R = KB^2$$

where K is the sensitivity of the sensor (Fig. 3-16). Fig. 3-14j shows the resistance change as a function of the applied magnetic field and the sensitivity under 25°C and 200°C was derived through curve fitting.

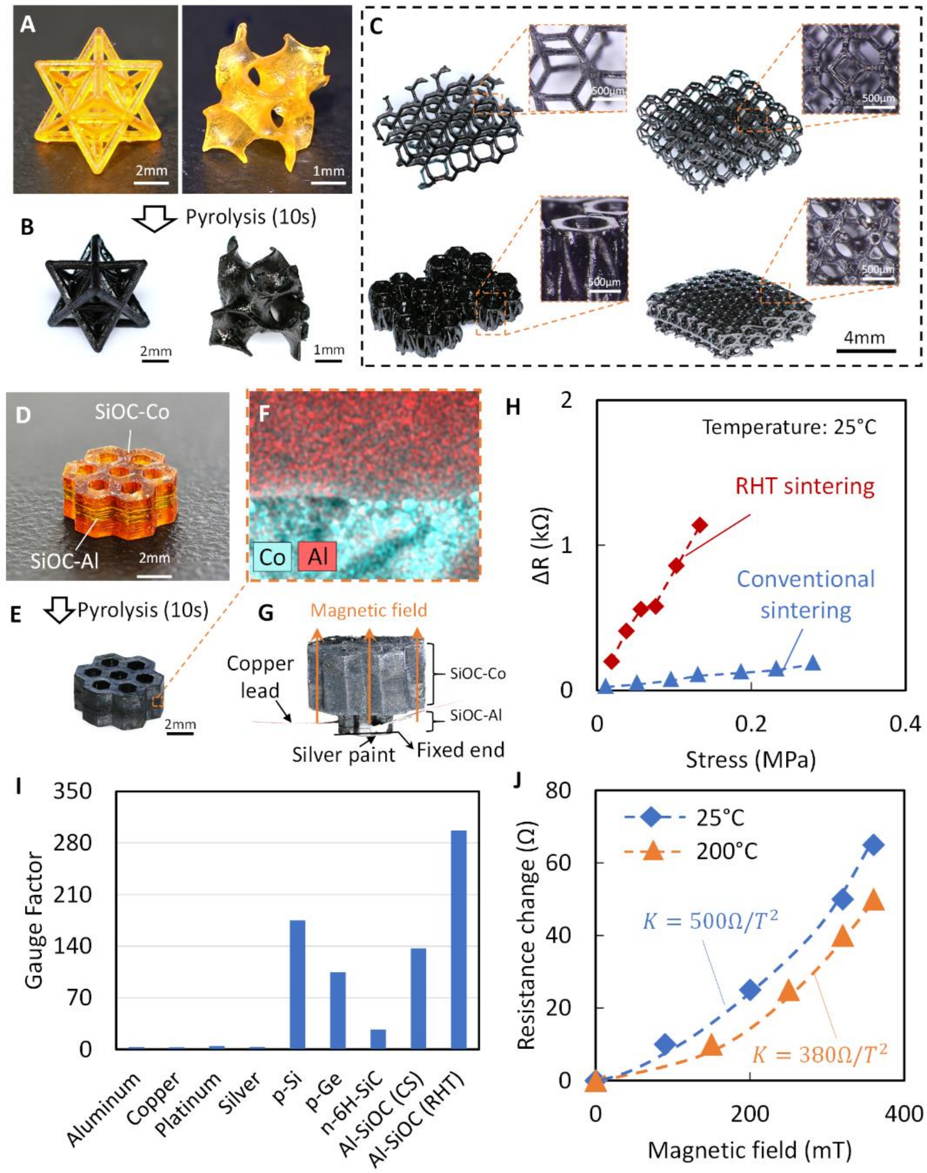

Figure 3-14 (a) Optical image of the SiOC green part printed with a single material. (b) Optical image of SiOC samples sintered by RHT method showing the uniform shrinkage and maintained shape. (c) Four complex structures with different repeating units using RHT technique. (d-e) Green part and sintered SiOC structures doped with Al and Co, respectively. (f) Elemental mapping of the boundary of the Co and Al-doped SiOC. (g) Optical image of the as-fabricated multi-material magnetic flux density sensor. (h) The resistance of the Al-doped SiOC section of the magnetic flux density sensor sintered with conventional sintering method and RHT sintering method as a function of force, respectively. The experiment was performed at room temperature. (i) Comparison of gauge factors of various materials. (j) The resistance change of the Al-doped piezoresistive section as a function of the magnetic field.

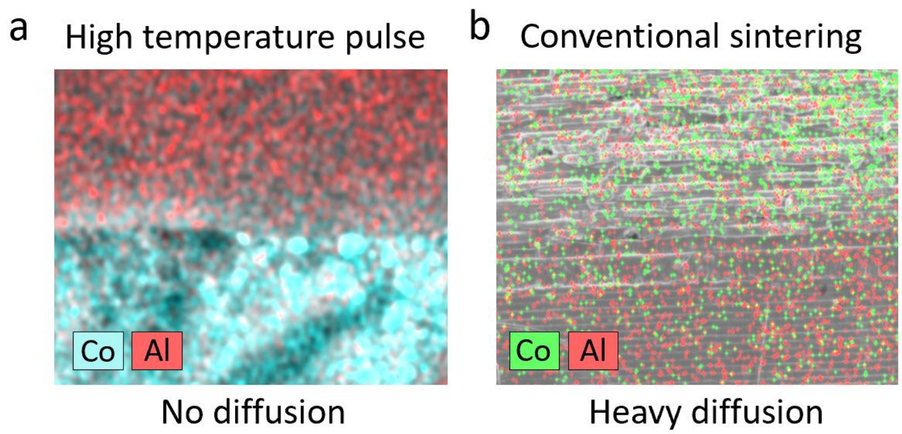

Figure 3-15 Elemental mapping of the 3D printed multi-material sample sintered by a) the high-temperature pulse method and b) conventional sintering method.

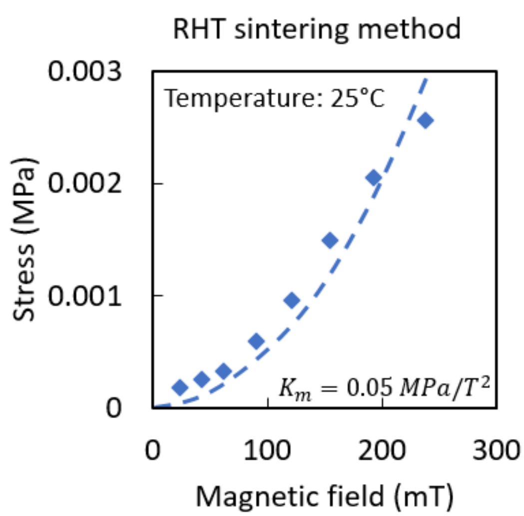

Figure 3-16 The stress applied on the Al-doped SiOC section by the Co-doped SiOC section as a function of magnetic fields.

Chapter 4 From structural to multi-functional materials

Beyond structural materials, my research then extends to the additive manufacturing of multi-functional materials. My research aims to add functionality beyond extreme mechanical properties. These functionalities can be electrodynamic, acoustic, thermal, piezoelectric and electromagnetic properties, which makes the metamaterial not only a structural material for space-filling or supporting but also a functional material that can harvest energy, respond to the environment or communicate with devices.

To achieve this, we started with the piezoelectric metamaterials. This chapter introduces the fabrication and functionalization of a piezoelectric composite material. By integrating a blade-casting process with the LAPμSL system, piezoelectric metamaterials with arbitrary micro-architectures can be fabricated. Moreover, through functionalization of the piezoelectric particles, the 3D printed piezoelectric composite can outperform the state-of-art piezoelectric polymers and other piezoelectric composites.

Notably, the 3D printing technique and functionalization process is not limited to piezoelectric materials and can be implemented to a wide range of functional materials, including piezomagnetic, dielectric and electrostrictive materials. The process introduced in this chapter allows independent tuning of matrix stiffness, allowing the creation of rigid to flexible multi-functional composite materials.

4.1 Micro-stereolithography system integrated with blade-casting process

To fabricate the multi-functional materials, nanoparticles of the active materials need to be added to the photocurable polymer to fabricate functional composites. In this section, we use piezoelectric nanoparticle (PZT) as an example to describe the upgraded LAPμSL system.

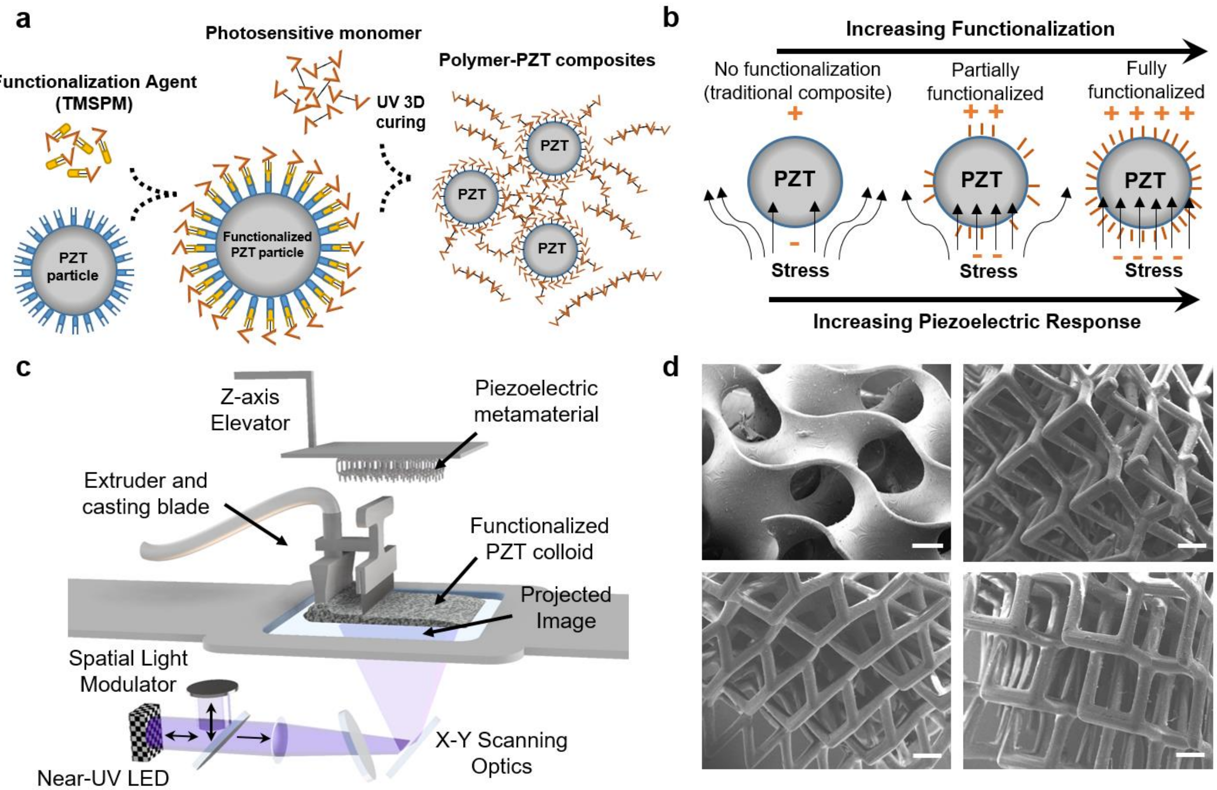

Figure 4-1 Surface functionalization of PZT with photosensitive monomers and 3D printing of piezoelectric metamaterials with complex micro-architectures. a) Schematic illustration of surface functionalization method and strong bonds between the nanoparticles and the polymer matrix after UV curing process. b) Schematic illustration of the relationship between the surface functionalization level and the piezoelectric response. The piezoelectric response increases with the surface functionalization level as a result of increasing stress transfer. c) Schematic illustration of the high-resolution 3D additive manufacturing system. d) SEM images of 3D printed piezoelectric microlattices. Scale bar: 300 μm.

The fabrication method starts by synthesizing concentrated surface-functionalized piezoelectric nanoparticles, dispersed with UV sensitive monomers as a structural matrix that can be sculpted into 3D structures by near-ultraviolet (near-UV) light[100]. While surface functionalization of ~4vol% piezoelectric nanoparticles has shown appreciable piezoelectric coefficient as compared to non-functionalized dispersion[100], the trade-off between high piezoelectric responsiveness and processability has limited the realizations of arbitrary piezoelectric 3D micro-architectures with high piezoelectric coefficients. As shown in Fig. 4-1a, a functionalization agent, (trimethoxysilyl propyl methacrylate) is covalently grafted to the PZT particle surface via siloxide bonds leaving free methacrylate on the surface. Here, the surface functionalization reaction is optimized to maximize surface coverage. These strong covalent bonds between the closely packed piezoelectric nanoparticles and the polymer matrix network enable achieving uniformity in the highly concentrated piezo-active colloidal resin (Fig. 4-2) by creating a sterically hindered surface as well as reaching the upper bound of the piezoelectricity output of the nanocomposite at a given loading concentration (Fig. 4-1b, Fig. 4-2, Fig. 4-3). Here, strict control of the thickness of the colloidal paste through a designed recoating system and reduction of oxygen inhibition enables the fabrication of complex 3D piezo-active architectures with fine features (see Section 4.1.1) from a range of concentrated colloidal particles entrapped with UV sensitive monomers (Fig. 4-1d). This versatile process is not limited to PZT. Surface functionalization can be implemented to enhance the response of a wide range of piezoelectrics (Barium Titanate, etc.) or other functional materials such as piezomagnetic (Bismuth ferrite). This nanocomposite system allows independent tuning of matrix stiffness, by changing the photo-sensitive monomer composition, allowing us to access rigid to flexible materials to convert mechanical stress to voltage signals, as well as energy harvesting.

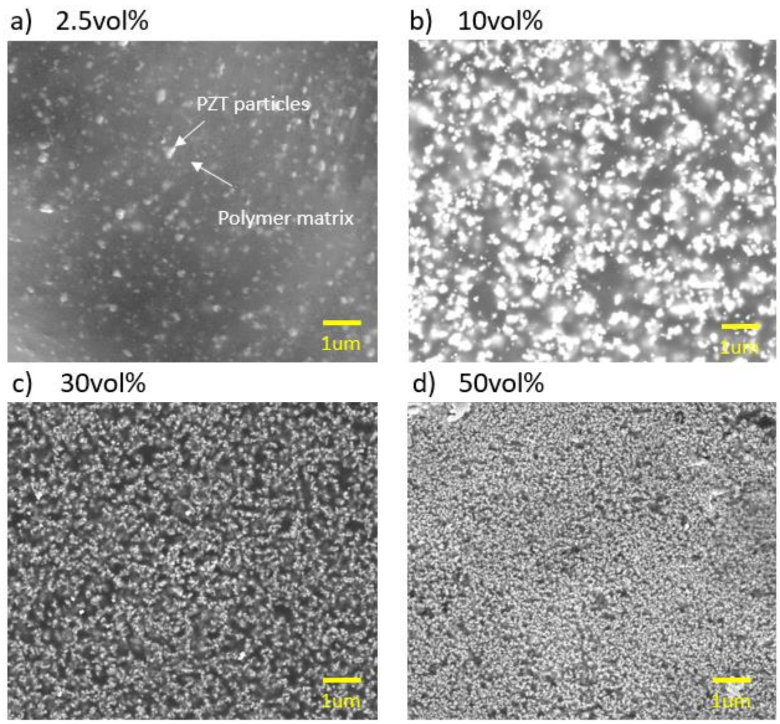

Figure 4-2 The SEM micrographs of the cross-section areas of the composite having a) 2.5vol%, b) 10vol% c) 30vol% d) 50vol% particle loading.

The system to process piezoelectric feedstock achieves a minimum printable 3D feature size of ~20um in the transverse direction, which is determined by the pixel resolution of the DMD array and the reduction lens. The resolution in the vertical direction is controlled by the layer thickness during the printing. To ensure the layer thickness is well-controlled, the layer recoating process and the cure depth of the resins with higher nanoparticle loadings are modeled and experimentally characterized during our study.

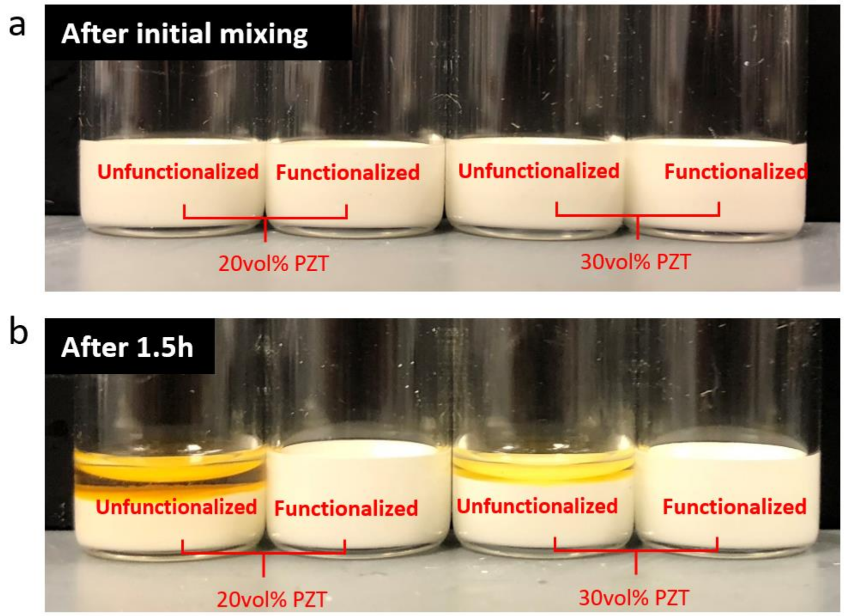

Figure 4-3 Optical images of the resins mixed with unfunctionalized or functionalized particles a) after initial mixing and b) after 1.5h.

4.1.1 Resolution and optimization of the fabrication process

After one layer of resin is cured, a recoating process is followed. The stage on which the lattices were printed is moved for a layer thickness to recoat resin for the printing of the next layer. While resin with low particle loading can be recoated within a short time between each layer, high particle loadings resin suffers from its dramatically increased viscosity as such it cannot flow into the gap uniformly within a reasonable time. To ensure the high particle loading resins can be uniformly and efficiently recoated, we used tape-casting method[101] to recoat the resin, as shown in Fig. 4-4a&b. As shown in Fig. 4-4, once a layer is cured, the Z stage moves. Right after the movement, an extruder squeezes a small amount of the resin on the oxygen permeable membrane and a doctor blade produces a thin resin film on the membrane. Then the Z stage moves back, leaving a flat layer height resin.

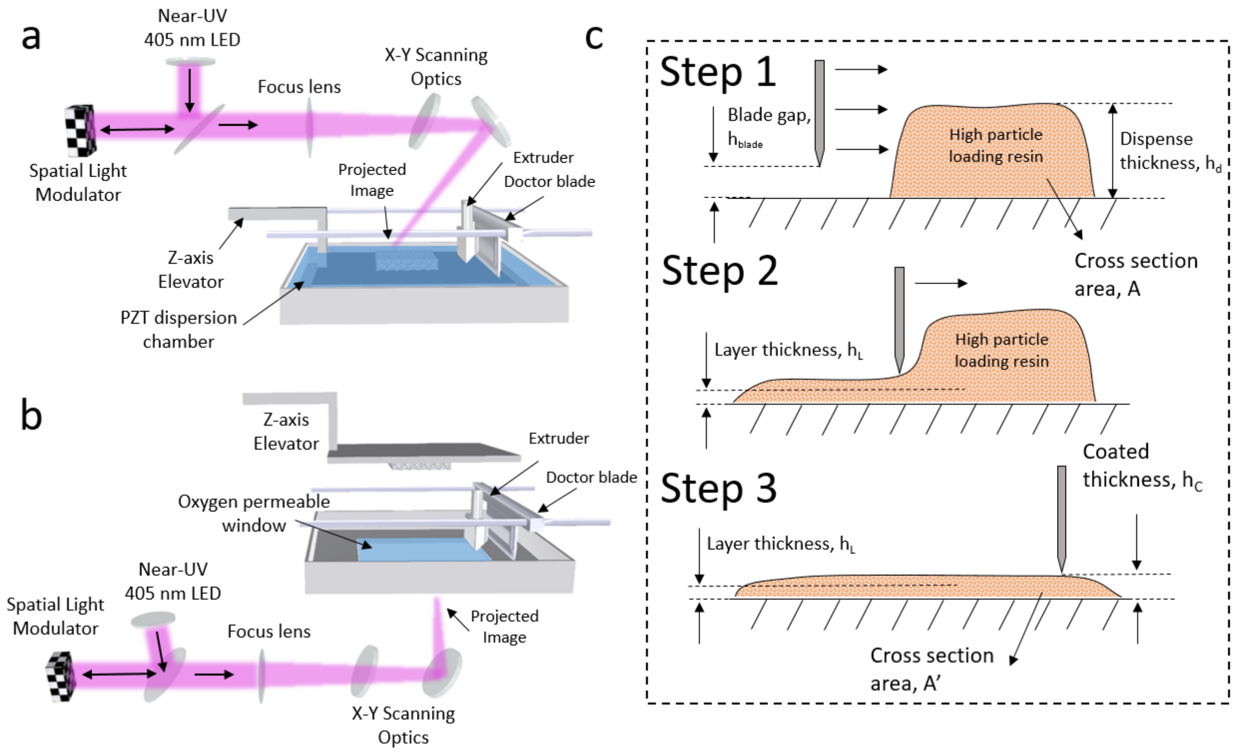

Figure 4-4 a-b) Schematics of the projection stereolithography systems used in our study with resin dispensing and flattening setup for a range of functional material loadings. c) Three steps during the recoating process.

4.1.2 Optimization of the blade height to control thickness

In our process, only a small amount of resin for each layer was dispensed. We designed the blade position such that the gap between the blade head and the substrate is sufficient to ensure 1) dispensed nanoparticle resin can spread out the printing area, 2) the spread resin height is higher than exposure thickness. Fig. 4-4c illustrates the blade design criteria to ensure adequate nanoparticle resin quality. The blade height must satisfy

$$\frac{2h_L A'}{A} < h_{blade} < \frac{Ah_d}{A'}$$

where A is the cross-section area of the dispensed resin, h_d is the thickness of the dispensed resin and A' is the cross-section area of the recoated resin (Fig. 4-4c).

We tested the recoating quality of the resins having different particle loadings and the results are summarized in Fig. 4-5. The particle loading that can yield a relatively uniform layer with high quality (without pores) for final fabrication was found to be 50vol% (~ 88 wt.%) in our study.

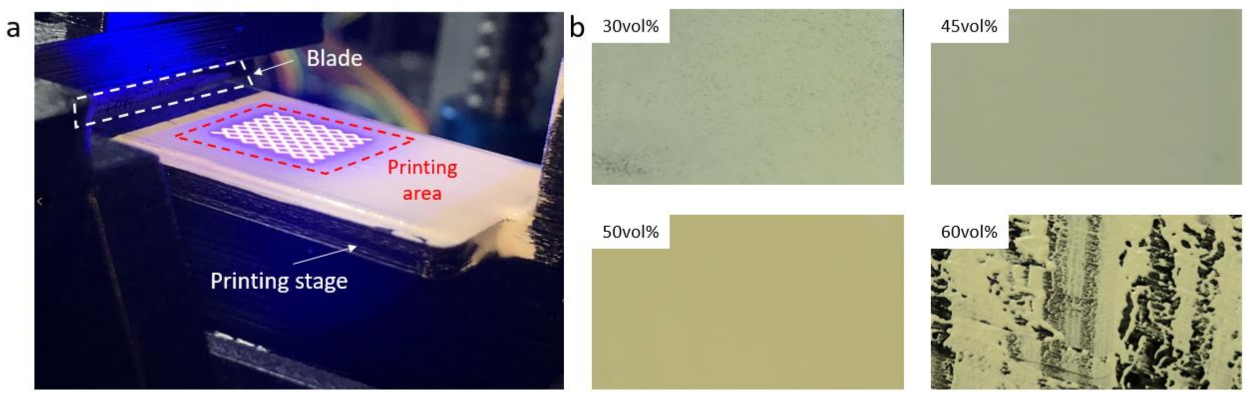

Figure 4-5 (a) Camera image of an as-cast uniform piezoelectric photosensitive resin film for Projection Micro-stereolithography; doctor blade height is 100μm. (b) Optical image of as-coated piezoelectric photosensitive resin films with different particle loadings.

4.1.3 Curing depth of highly loaded piezoelectric monomers

Another important parameter affecting the layer thickness is the cure depth of the resin. In SLA process, the curing depth is related to the Beer-Lambert law, which is formulated as[69]:

$$Z_{ct} = \frac{1}{\alpha} \ln\left(\frac{E}{E_c}\right) \qquad (4-1)$$

where α is the resin absorption coefficient, E and E_c are the actual and critical exposure respectively. E can be controlled by UV light intensity or exposure time.

For resins loaded with particles, the UV light is scattered or absorbed when it travels through the resin. The absorption coefficient of the resins, α, becomes quite large in highly particle loaded resins, and can be formulated as[102-104]:

$$\alpha \sim \frac{3S\emptyset}{2d} \qquad (4-2)$$

$$S \sim \left(\frac{\Delta n}{n_0}\right)^2 \left(\frac{d}{\lambda}\right)^2 \qquad (4-3)$$

where S is a constant related to the scattering efficiency of the particles, d is the mean diameter of particles, $\emptyset$ is the volume fraction of the particle in the high particle loading resin, n_0 is the refractive index of the rein, Δn is the refractive indice difference between the particle and the solution and λ is the light wavelength.

Empirically, we found that the layer thickness has been set to be less than half of the cure depth in order to ensure tight bonding force between neighboring layers. This creates challenges as higher particle loadings nanoparticles cause reduction of the resin penetration depth based on Eq. (4-1) due to higher resin absorption constant. For each particle loading a series of exposure time and dosage must be carefully conducted to characterize the penetration depth of the loading. Additionally, our enclosed system allows accurate control of oxygen concentration (typically below 1%), which helps to increase the cure depth of the resin via prevention of oxygen inhibition mechanism[26, 105] and promote more photopolymerization. To find the dosage and exposure time for sufficient cure depth (twice of the layer thickness) of resins with different particle loadings, an identical circle array pattern with different exposure times and dosages is used to characterize the cure depth. Excess resin is then wiped away and the thickness of the printed dot is measured under a microscope. As shown in Fig. 4-6, the number of cured disk patterns decreases as the particle loading increases under the same exposure profile, which indicates different exposure parameters are needed for each loading concentration.

As an example, we plotted the working curve of the resin with 40vol% loading particles in Fig. 4-6b. The light intensity we used is the highest intensity of the projection system, which is ~20W. Different exposure time is used to achieve different curing depth. The curing depth is 30um with 16s exposure time and starts to saturate after 16s. So we used 15um as the layer thickness during the printing of the 40vol% particle loading resin.

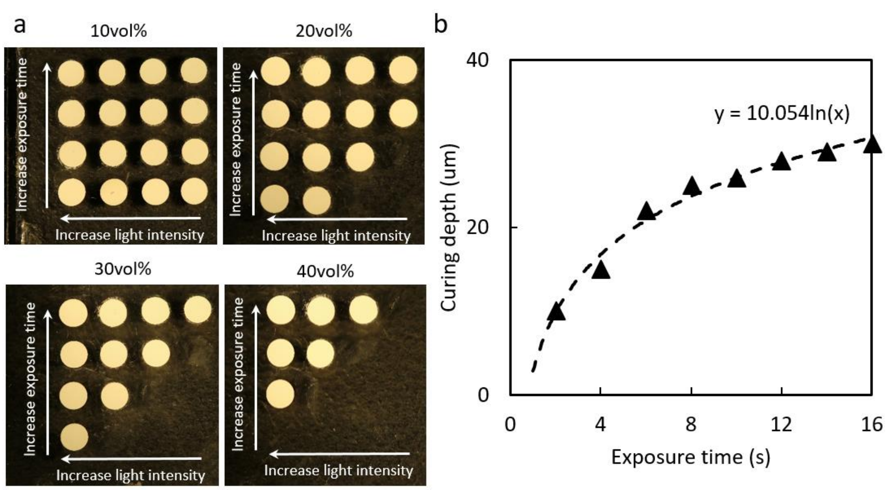

Figure 4-6 a) Optical images showing the curing depth of resins with 10vol%, 20vol%, 30vol% and 40vol% particle loadings. b) Curing depth of the 40vol% loading resin as a function of the exposure time.

4.2 Surface functionalization of the piezoelectric particles

4.2.1 Procedures of the surface functionalization

All chemicals were purchased from Sigma-Aldrich and used as received. For functionalization, 0.6g of PZT was ultrasonically dispersed (VWR Scientific Model 75T Aquasonic ~ 90 W, ~ 40 kHz) in 50g of deionized water with 1.049g glacial acetic acid for 2h. To this 1.049g of 3-(trimethoxysilyl)propyl methacrylate (TMSPM) was added. The mixture was then refluxed while stirring for 5h. Particles were cleaned by centrifugation, discarding the supernatant, and then dispersing in ethanol for at least two cycles. Particles were dried overnight under vacuum or gentle heat. The resulting 3D printable functionalized PZT nanocomposites achieved a volume loading from 2.5vol% to 50vol% (equivalent to 16wt% to 88wt%).

4.2.2 Characterization of the effect of particle functionalization

To characterize the effect of functionalization, we prepared composite samples with varying degrees of functionalization between nanoparticles and polymer matrix and probed their effect on the piezoelectric properties at different particle volume loading. The experiments confirmed that the fully functionalized systems provide the “upper bound” of properties obtainable for a particular volume fraction of the piezoelectric particles while the partially functionalized particle systems provide less.

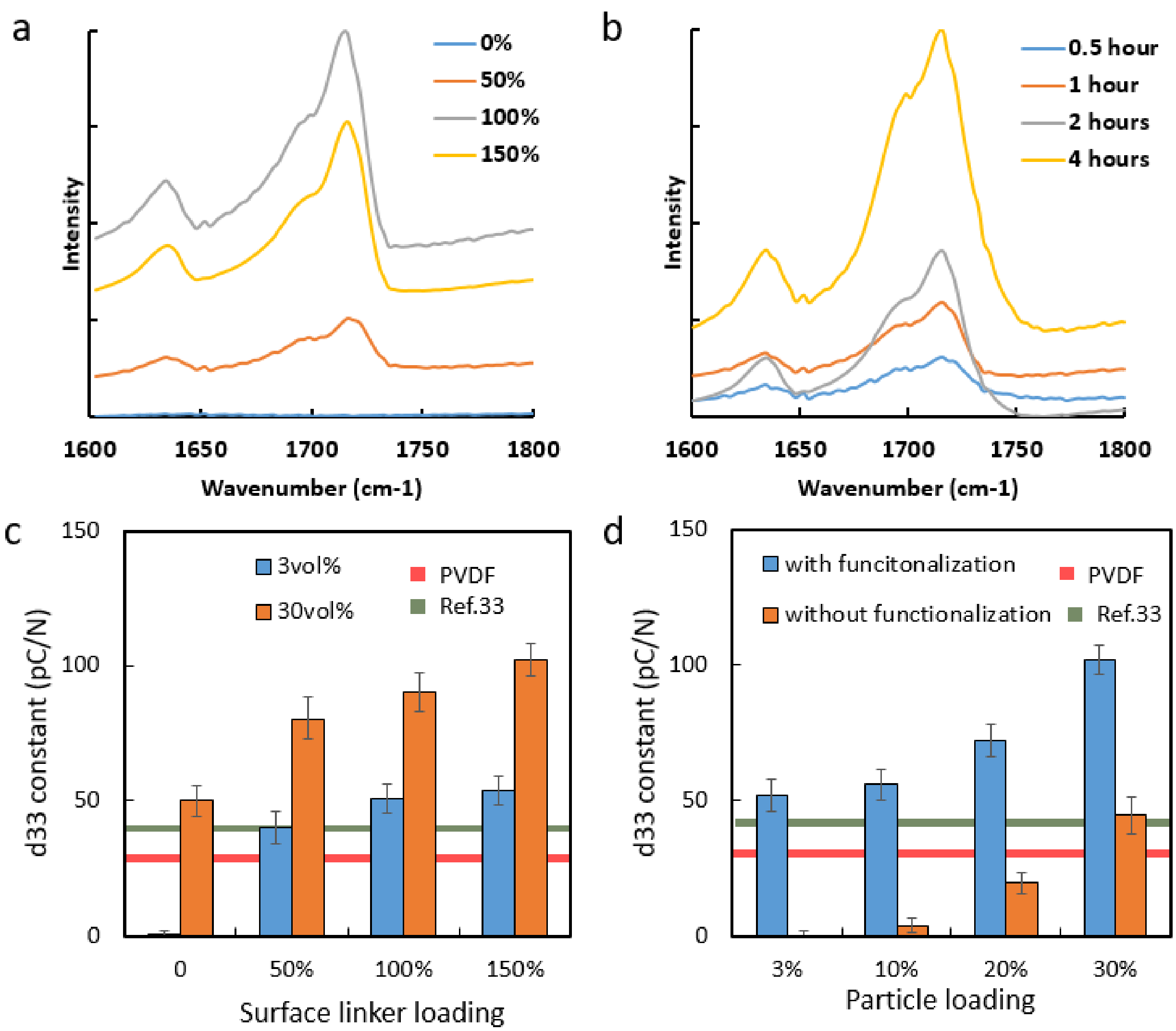

Figure 4-7 a) Fourier-transform infrared spectroscopy (FTIR) result showing the effects of different TMSPM loading. b) FTIR result showing the effects of reaction time on the surface functionalization, peaks around 4hrs. c) *d* constant as a function of the surface linker loading for functionalization of PZT nanoparticles. d) Comparison of *d* constant as a function of PZT nanoparticle volume loading percentage under two conditions: with functionalization and without functionalization.

Fig. 4-7a&b shows the Fourier-transform Infrared Spectroscopy (FTIR) of thoroughly cleaned functionalized PZT particles with different intimal loadings of the surface agent or reaction times. The spectrum focuses on the carbonyl and alkene of the acrylate surface groups nominally at 1710

cm^{-1} and 1630 cm^{-1}, respectively. It shows the functionalization level can be varied by the surface linker loading or reaction time.

The PZT particles were functionalized with 0wt% ~ 150wt% surface linker loadings. The particles with different functionalization levels were mixed with the UV curable resin with 3% to 30% volume loadings (equivalent to 18.8wt%~76.3wt% loading), and were used for fabricating cuboid samples (8mm by 8mm by 2 mm). As-fabricated samples were tested using the same apparatus described in Chapter 5. The d_{33} constants of the samples are summarized in Fig. 4-7c. For the low particle loading (3vol%) composite, the d constant is nearly zero without functionalization, and increases with the functionalization level until the particles are fully functionalized. The same trend was observed for the high particle loading (30vol%, i. e., 76.3wt%) composite, i.e., the d constant increases from ~50pC/N to ~100pC/N with fully functionalized nanoparticles.

To investigate the effect of functionalization at different particle loadings, cuboid samples having the same dimensions with 3vol%~30vol% PZT particles with and without functionalization were fabricated and tested. The results are shown in Fig. 4-7d. Within 30vol% loading, the performance of the piezocomposite is increased by the surface functionalization of the piezo particles. It can be noted that in the absence of functionalization, the baseline piezoelectric response is increased with higher volume loadings.

Chapter 5 3D printing of piezoelectric materials with designed anisotropy and directional response

This chapter reports design and manufacturing routes to previously inaccessible classes of multi-functional piezoelectric metamaterials with arbitrary piezoelectric coefficient tensor. The scheme is based on the manipulation of electric displacement maps from families of structural cell patterns. The resulting voltage response of the activated piezoelectric metamaterials at a given mode can be selectively suppressed, reversed or enhanced with applied stress. Additionally, these electro-mechanical metamaterials achieve high specific piezoelectric constants and tailorable flexibility with only a fraction of the functionalized solid. The strategy reported here can be applied to create the next generation of intelligent infrastructure, which can perform a variety of structural and functional tasks. Applications including location sensing, directionality sensing, self-stress sensing and energy harvesting are demonstrated in Section 5.3.

5.1 Design of 3D piezoelectric responses

A strategy was developed to realize the full design space of piezoelectric coefficients through the spatial arrangement of piezoelectric ligaments. The scheme involves analyzing configurations of projection patterns from a 3D node unit classified by connectivity. The evolutions of projection patterns give rise to diverse electric displacement maps (Fig. 5-1a-h), from which the piezoelectric coefficient tensor space d_{3M} ($M = 1{\sim}3$) can be designed, going beyond the limitations of the monolithic piezoelectric ceramics, polymers and their composite feedstock whose piezoelectric coefficients are located in the {- - +} quadrants[106-109] and {+ + -} quadrants[110, 111] of the dimensionless piezoelectric tensor space ($\bar{d}_{3M}$, which is defined by normalizing d_{3M} by the length of the vector, $\{d_{31}, d_{32}, d_{33}\}$). To capture the broadest possible design space, we start with a number of intersecting micro-struts at a node that can be tessellated into 3D periodic lattice. All intersecting struts are represented as vectors originating from the node, i.e., $\vec{L}_i$ ($i = 1 \sim N$, N is the node unit connectivity). In building the projection patterns, we define $\vec{l}_i^j$ as the 2D projection of $\vec{L}_i$ onto three orthogonal planes through the global 1-2-3 coordinate system of the 3D piezoelectric cube (Fig. 1a, $\vec{L}_i = \frac{1}{2}\sum_{j=1}^{3} \vec{l}_i^j$, $j =$1, 2, or 3). As an example, we use piezoelectric ceramic and its composites having $\bar{d}_{3M}$ distributed in the {- - +} quadrants[106-109] as the base material to construct the electric displacement maps. The white arrows pointing upwards or downwards against the 3-direction indicate the positive or negative electric displacement response of the strut along the 3-direction (i.e. poling direction).

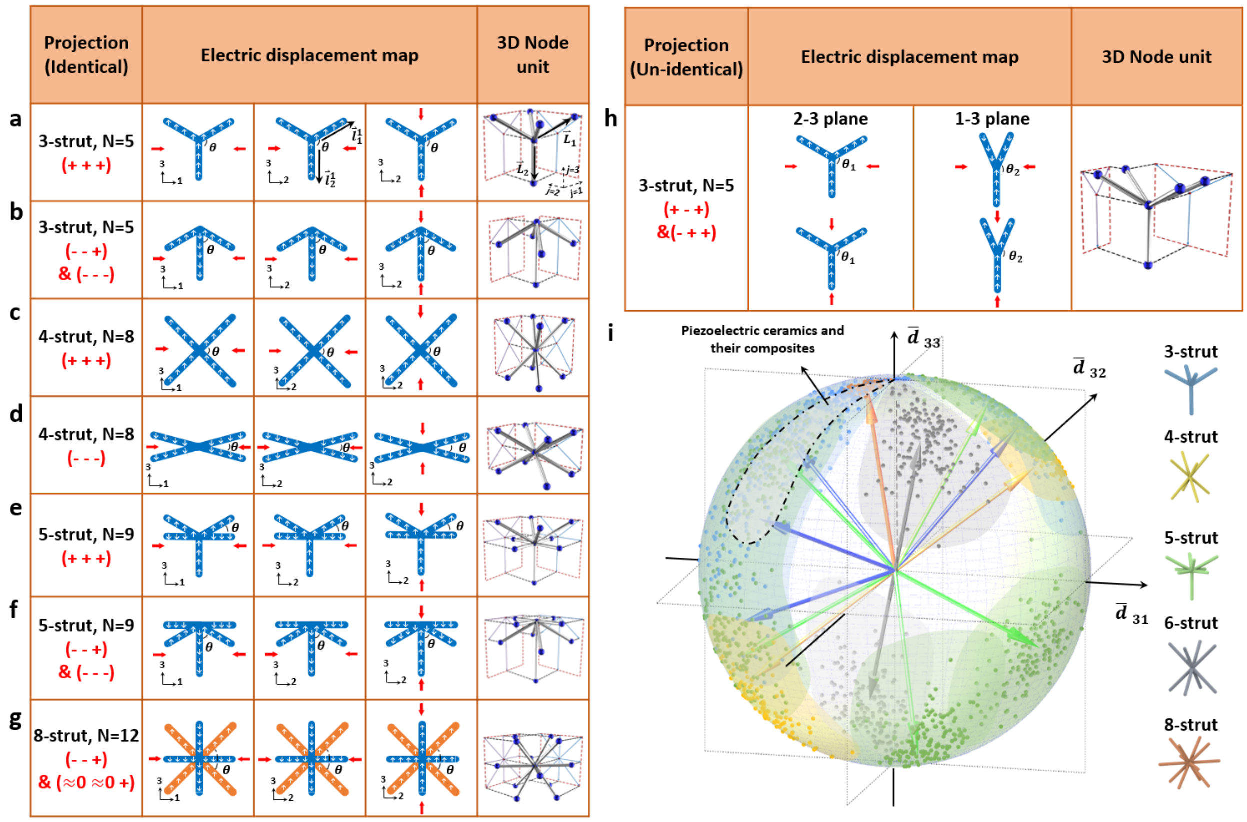

Figure 5-1 Design of piezoelectric metamaterials for tailorable piezoelectric charge constants. Designing 3D node units by configuring the projection patterns. (a-g) Node unit designs from 3-, 4-, 5-, and 8-strut identical projection patterns, respectively. Node unit with higher nodal connectivity can be constructed from superposition of projection patterns comprised of lower number of projected struts. (h) Node unit with dissimilar projection patterns showing decoupled $\bar{d}_{31}$, $\bar{d}_{32}$. The white arrows in the projection patterns pointing towards the positive or negative 3-direction indicate the positive or negative electric displacement contribution to poling direction 3. Red arrows in (a-h) indicate the compression loading along 1-, 2-, or 3-direction. (i) A dimensionless piezoelectric anisotropy design space accommodating different 3D node unit designs with distinct d_{3M} distributions; each d_{3M} is normalized by the length of vector $\{d_{31}, d_{32}, d_{33}\}$, and therefore, $\bar{d}_{31}$, $\bar{d}_{32}$ and $\bar{d}_{33}$ form a right-handed 3D coordinate system. Dimensionless piezoelectric coefficient of monolithic piezoelectric ceramics and their composite feedstock are marked in the {- - +}.

Configuring the projection patterns in these planes results in diverse electric displacement maps, allowing access to different quadrants of the d_{3M} property space. A basic 3D node unit containing 3, 4, and 5 intersecting struts on the projection patterns are illustrated in Fig. 5-1a~f. We start with

3D node unit with identical 3-strut projection patterns on 1-3 and 2-3 planes, i.e. $d_{31} = d_{32}$ (Fig. 5-1a, b). Configuring the projection pattern via rotating the relative orientations of two projected struts ($\theta = \angle \vec{l}_1^1 \vec{l}_2^1$) redistributes the electric displacement contributions as indicated by the white arrows reversing directions in the projection pattern (Fig. 5-1a, b). Rotating the projection patterns allows us to inversely reorient the intersecting spatial struts with correlations calculated in Section. 5.1.1 and 5.1.2. This results in the $\bar{d}_{3M}$ tensor shifting from {+ + +} quadrant, to highly anisotropic distribution near the positive $\bar{d}_{3M}$ axis {0 0 +}, to {- - +} quadrant with negative d_{31} and d_{32} as well as positive d_{33} (Fig. 5-1i). Further decrease of the relative orientation reverse all values of the d_{3M} to occupy the {- - -} quadrant (Table S1). Similarly, for a 4-strut or 5-strut projection pattern with two axis-symmetry, decreasing the relative orientation ($\theta = \angle \vec{l}_1^1 \vec{l}_2^1$) of projected struts results in the change of d_{3M} distribution from {+ + +} quadrant to {- - -} quadrant (Fig. 5-1i) or {- - +} due to the competitions of the opposite electric displacement contributions within the struts (Fig. 5-1c-f).

The designs can be broadened by increasing 3D node unit connectivity through superposition (Fig. 5-1g). The micro-architectures with high nodal connectivity are deformed predominantly by compression or tension[1, 41]. As reduced energy is taken by strut bending which does not contribute to the electric displacement in 3-direction, the d_{33} increases with additional nodal connectivity.

Moreover, the designs are not restricted to identical projection patterns where d_{31} and d_{32} are coupled. 3D node unit designs with dissimilar projection patterns allows independent tuning of d_{31} and d_{32} ("out of 45° plane" distribution of d_{3M}, Fig. 5-1i, $d_{31} \neq d_{32}$). We configure the dissimilar electric displacement maps via independently varying the relative orientations θ_1 and

θ_2 on 1-3 and 2-3 planes (Fig. 5-1h). The compression along 1-direction and 2-direction on the 3D node unit, therefore, generate different electric displacement maps and result in the decoupling of d_{31} and d_{32} (Fig. 5-1h).

The d_{nM} of designed units can be numerically computed through collecting the electric displacement from all intersecting strut members $\vec{L}_i$ at equilibrium under applied stress. Such model relates the configuration of the projection patterns $\vec{l}_i^j$ with the piezoelectric coefficient of interest d_{nM} of the metamaterials

$$d_{nM} = \frac{\sum_{i=1}^{N} \int_{V_i} d_{nm}^i T_{mr}^i \sigma_r^i dV_i}{\sum_{i=1}^{N} \int_{V_i} \delta_{mM} T_{mr}^i \sigma_r^i dV_i}$$

, where d_{nm}^i is the piezoelectric coefficient matrix of the base material ($n = 1, 2, 3$, $m, M = 1\sim6$), T_{mr}^i represents the stress-transformation matrix from the local x- y-z coordinate system to the global 1-2-3 coordinate system, σ_r^i is the stress vector in the local coordinate system ($r = xx, yy, zz, xy, xz, yz$), V_i is the volume of the i-th strut in the node unit and δ_{mM} is the Kronecker delta. Configuring the projection patterns generate various designs of architectures which occupy different quadrants of the $\bar{d}_{3M}$ distribution space as shown in Fig. 5-1i, where $M = 1\sim3$. These families of 3D node units constitute a broad 3D piezoelectric constant selection where d_{3M} occupy desired quadrants of the property space, in contrast to the piezoelectric coefficients obtained by piezoelectric foam models. This rich design space creates an enormous palette of novel applications as demonstrated in later sections.

5.1.1 Electric displacement manipulation via screw angle in 2D projection pattern

As shown in Fig. 5-2a&b, the plane angles θ_1, θ_2 and θ_3 obtained from projection pattern as:

$$\theta_1 = \theta_2 = \theta - 90°, \theta_3 = 45°$$

The space angle θ_4 could be expressed as:

$$\theta_4 = \arctan\left(\sqrt{2}\tan\,(\theta - 90°)\right)$$

From the two equations above, all the angles θ_1, θ_2, θ_3 and θ_4 invoked in the analytical analysis could be tuned through adjusting angle θ in the projection pattern. Therefore, the stress matrix of each strut in the global coordinate system could be conveniently manipulated through configuring its orientation in the projection pattern. Subsequently, the effective electric displacement and effective charge constants are manipulated through the configuration of strut orientation in the projection patterns.

5.1.2 Comparison between the theoretical prediction and the FEA results

ABAQUS 6.14 was used to conduct the finite element analysis on all the designs shown in Fig. 5-2. Comparison between analytical derivations and finite element analysis shows great agreement between the two. We listed the calculated results in Fig. 5-2. The minimal difference between the analytical model and FEA result can be explained by the difference of stress calculation of vertical struts during calculation of d_{31}^{eff} and d_{32}^{eff}. The axial stress on the vertical strut $\vec{L}_5$ is considered zero in the analytical derivation of equilibrium state[112], whereas the FEM analysis indicated the stress within vertical strut still takes approximately 5% of that of the diagonal strut ($\vec{L}_1, \vec{L}_2, \vec{L}_3, \vec{L}_4$) due to stress transferred from the node.

5.2 Measurement of 3D piezoelectric responses

To evaluate the piezoelectric responses of the designed piezoelectric metamaterials, a poled cubic lattice is constructed by periodic packing of the unit cell along its three principal directions. A shaker with integrated force sensor in contact with the surface of the samples exerts cyclical loadings on the samples. We measured the generated voltages (in 3-direction) induced by the applied stress with a resistor connected to data acquisition system. We found excellent agreement of the measured $\{d_{31}, d_{32}, d_{33}\}$ signatures with the designed response to force from different directions. Here, *N*=5 designs (3-strut projection pattern, Fig. 5-1a, b) are used to demonstrate the different voltage output patterns due to the distinct distributions of d_{3M}. As identical cyclic loadings (~0.5N, sawtooth loading profile) are applied along three orthogonal directions, significant differences in the voltage output patterns are observed for three distinct designs (Fig. 5-3a-c). The *N*=5 piezoelectric metamaterial of $\theta = 75$º (Fig. 5-3a) outputs a positive voltage when loaded in 3-direction (the polarization direction), while the sample generates a negative voltage as loaded in 1- or 2- direction. In contrast, Fig. 5-3b shows voltage outputs of our N=5, $\theta = 90°$ lattice in 3-direction being positive while voltage output in 1- or 2- direction being suppressed, exhibiting highly anisotropic response. By further increasing θ to 120º, the voltage outputs in all 1, 2, 3 directions are positive when loaded in any directions, as shown in Fig. 5-3c, due to its all positive d_{3M} distribution.

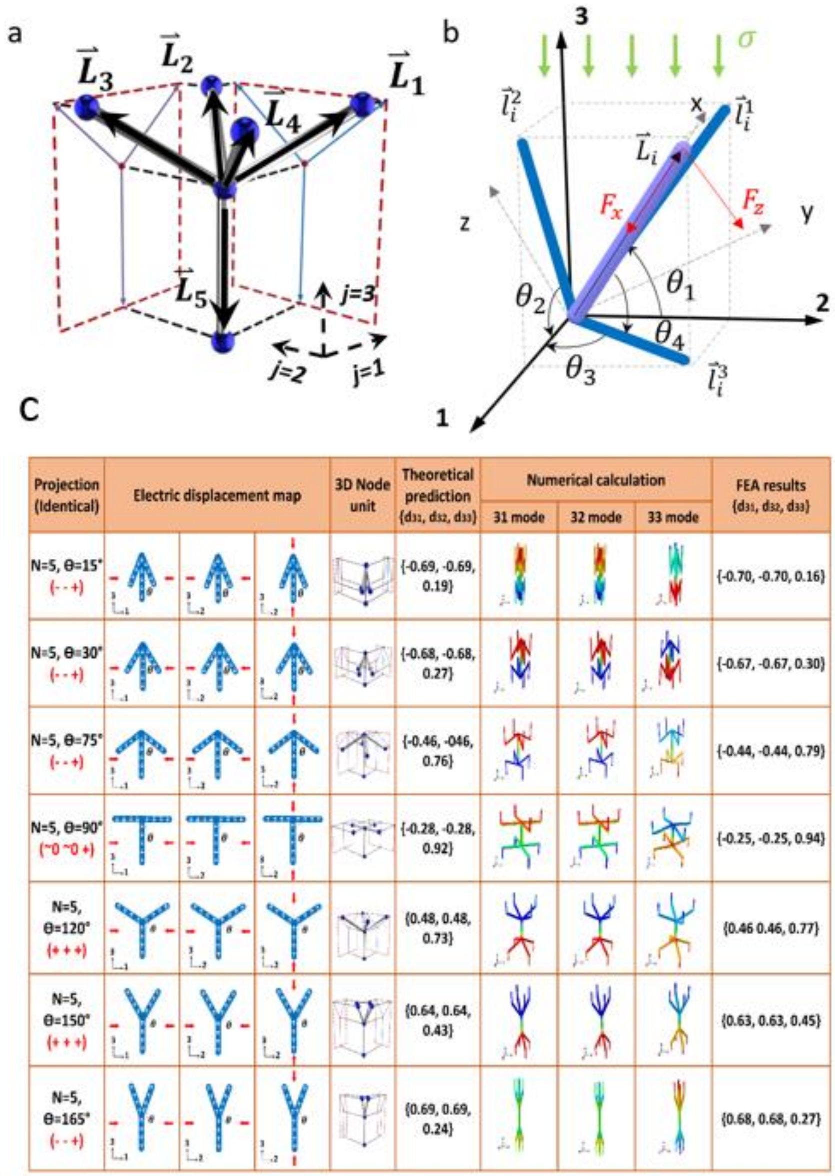

Figure 5-2 a) Schematic of the N=5 design. b) Schematic of a single strut with two coordinate systems. c) The comparison between analytical results, experiment results and numerical results of the N=5 lattices.

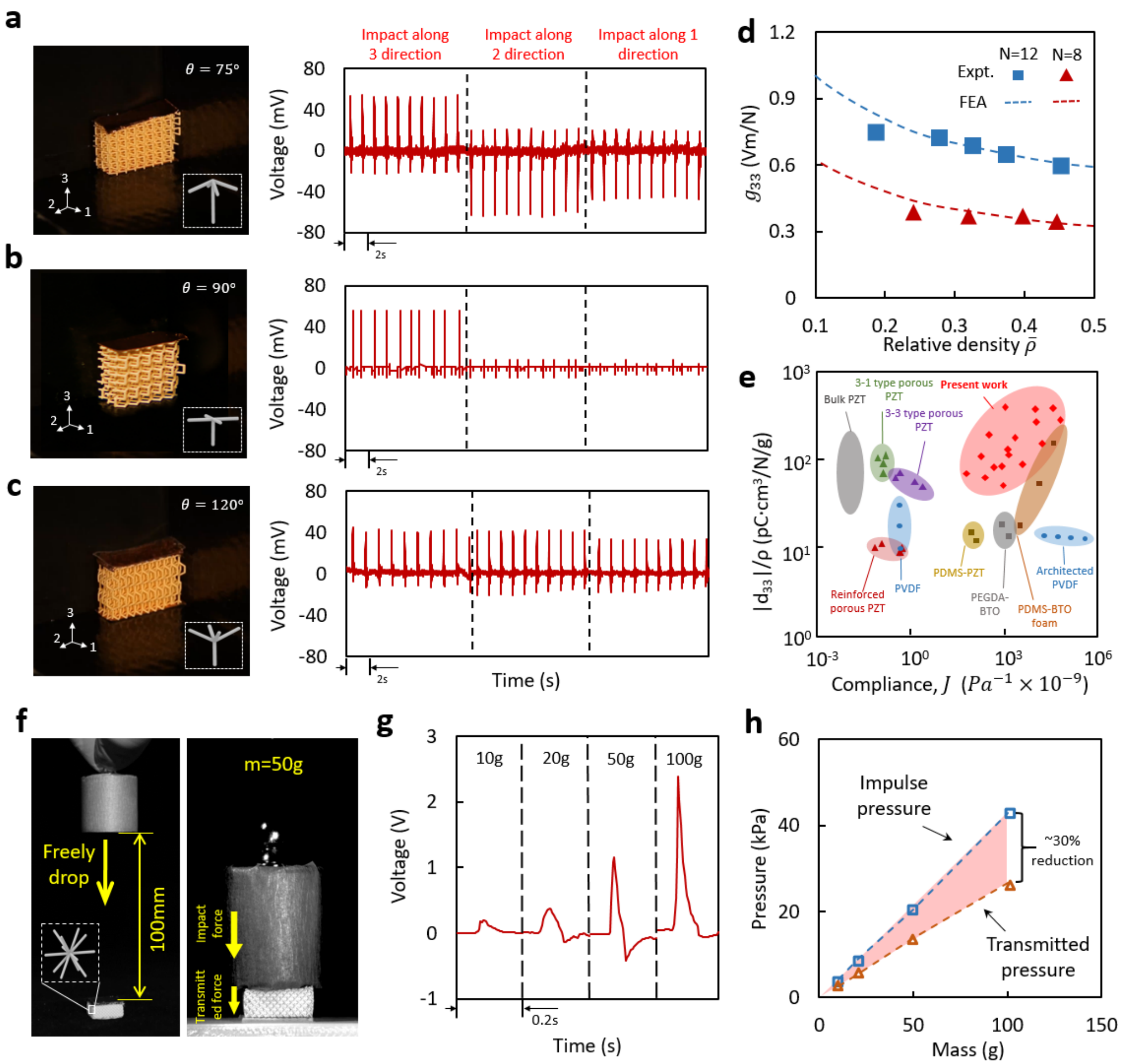

Figure 5-3 Measurement of 3D piezoelectric responses. a-c) Optical images of representative piezoelectric metamaterials comprised of N=5 node units and their corresponding real-time voltage outputs under impact coming from 1, 2, and 3 directions, respectively. d) Effective piezoelectric voltage constant g_{33}^{eff} versus the relative density of N=8 and N=12 lattice materials. e) Comparison of specific piezoelectric charge coefficients and elastic compliance between the piezoelectric metamaterials presented in this study and typical piezoelectric materials[100, 113-119]. f) Drop-weight impact test on the as-fabricated piezoelectric lattice (N=12). g) The real-time voltage output of the lattice corresponding to various drop weights. The transient impact stress activates the electric displacement of the metamaterial in the 3-direction, shown as the trace of the voltage output against the impact time. h) Impulse pressure and transmitted pressure versus the mass of

the drop weights. The significant gap (shaded area) between the detected impulse pressure and transmitted pressure reveals simultaneous impact energy absorption and self-monitoring capability of the 3D piezoelectric metamaterial.

To assess the mechanical-electric conversion efficiency, the effective piezoelectric voltage constant g_{33} defined as the induced electrical field per unit applied stress, was quantified by measuring the d_{33} of the as-fabricated metamaterials and the permittivity of the metamaterials. The resistor used in the apparatus is replaced by a circuit to quantify the charge generated in response to applied stress (Fig. 5-4). The d_{33} and g_{33} are then quantified by the ratio of the applied load and the generated charge. The g_{33} results of the metamaterial comprised of highly connected structure (N=12) and N=8 structure are shown in Fig. 5-3. Remarkably, g_{33} increases with the decreasing relative density, indicating the potential application in simultaneous lightweight and highly-sensitive sensor. The measured d_{33} over their mass density (i.e. $|d_{33}|/\rho$) and compliance are plotted against all piezoelectric materials (Fig. 5-3e). We found that these low density and flexible piezoelectric metamaterials achieve over 2 times higher specific piezoelectric constant than piezoelectric polymer (PVDF) and a variety of flexible piezoelectric composites (Fig. 5-3e, Fig. 5-5). Additionally, enhancement of the hydrostatic figures of merits can be obtained via unit cell designs with all identical signs of the $g_{3M}\{+ + +\}$ and $d_{3M}\{+ + +\}$ coefficients. This enhanced piezoelectric constant along with the highly connected 3D micro-architecture makes the 3D piezoelectric metamaterial an excellent candidate for simultaneous impact absorption and self-monitoring. A series of standard weights ranging from 10g to 100g were sequentially dropped onto the as-fabricated 3D piezoelectric lattice (N =12) attached on a rigid substrate (Fig. 5-3f) to impact the piezoelectric metamaterial. The transient impact stress activates the electric displacement of the metamaterial in the 3-direction, shown as the trace of the voltage output against the impact time (Fig. 5-3g). The impulse pressure on the piezoelectric metamaterial calculated using the measured d_{33}, and measured pressure transmitted to the rigid substrate against time are traced in Fig. 5-3h. The significant gap (shaded area) between the impulse pressure and transmitted pressure reveals the impact energy absorption and protection capability of our piezoelectric 3D metamaterial as a potential smart infrastructure[120, 121].

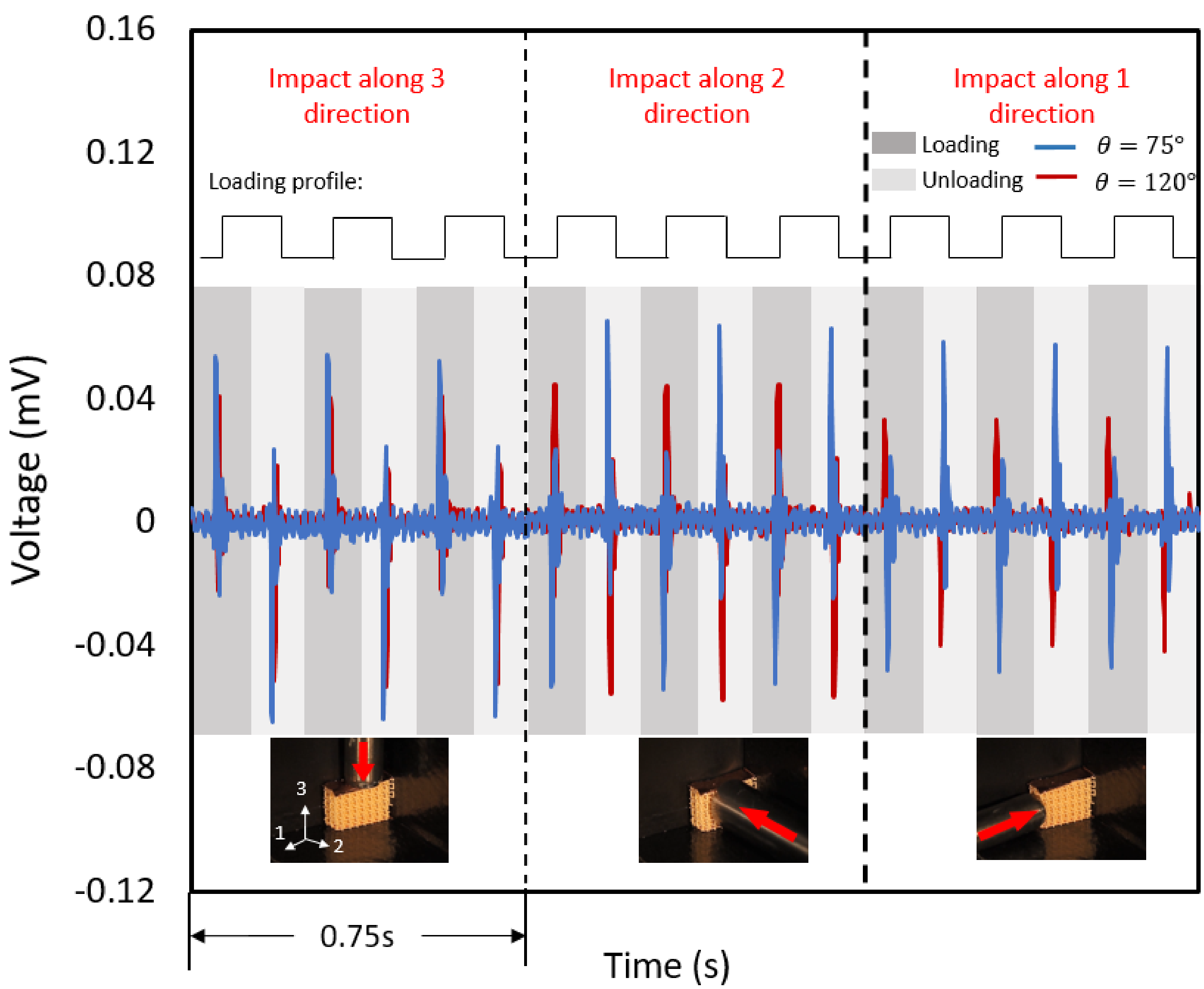

Figure 5-4 Real-time loading and release voltage outputs of two N=5 designs [$\bar{d}_{3M}$: {- - +}, $\bar{d}_{3M}$: {+ + +} respectively], with square loading profile stimulated from different directions. All samples are polled against 3 direction.

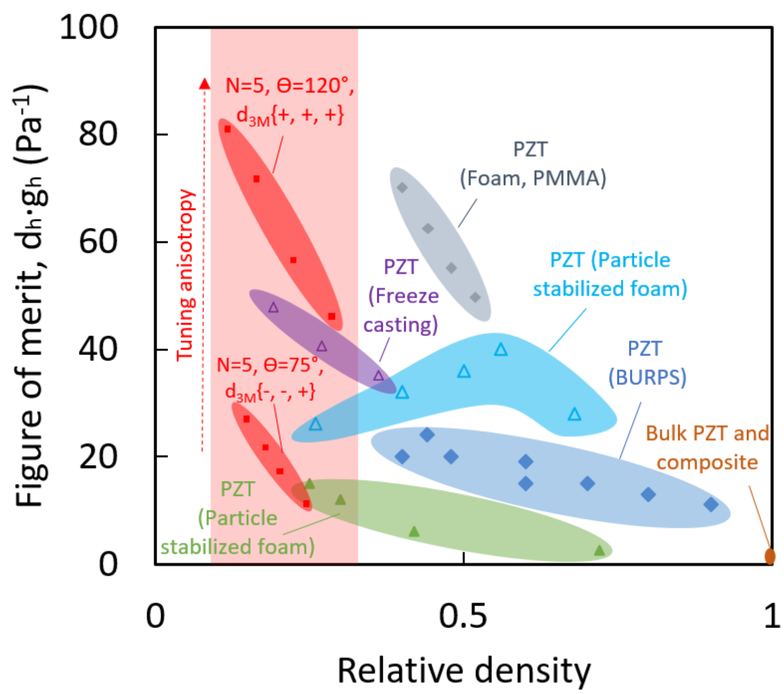

Figure 5-5 FOM of porous and bulk piezoelectric materials.

5.2.1 PZT particle properties

In the present work, commercial piezoelectric material particles (APC 850) were used. The size of the PZT particles was measured by dynamic light scattering (Malvern Zetasizer Nano ZS), and the average diameter to be 220.9 nm in acetonitrile solvent. The Curie temperature of the PZT (APC 850), used in this work, was 360°C.

5.2.2 Polarization method and results

We used the standard corona poling method[122] that has been commonly used for poling PZT composites[123]. A schematic of the poling fixture is shown in Fig. 5-6. We performed the poling process at the elevated temperature (~110^{o}C) for some of our samples in contact mode and did not observe any appreciable change in the physical properties. As such, we performed the poling process at room temperature for most of the samples. The corona process is a non-contact poling process and it involves application of very high field through a needle, while the sample is attached below on the grounded plate. Under the application of high field, the surrounding air is ionized. These ions are collected on the top surface of the sample generating the effective field across the thickness of the sample. This resulted aligning the dipoles (i.e., poling) in the direction of the applied field. The applied voltage during the poling process is 32kV and the height of needle from the sample surface is 2cm.

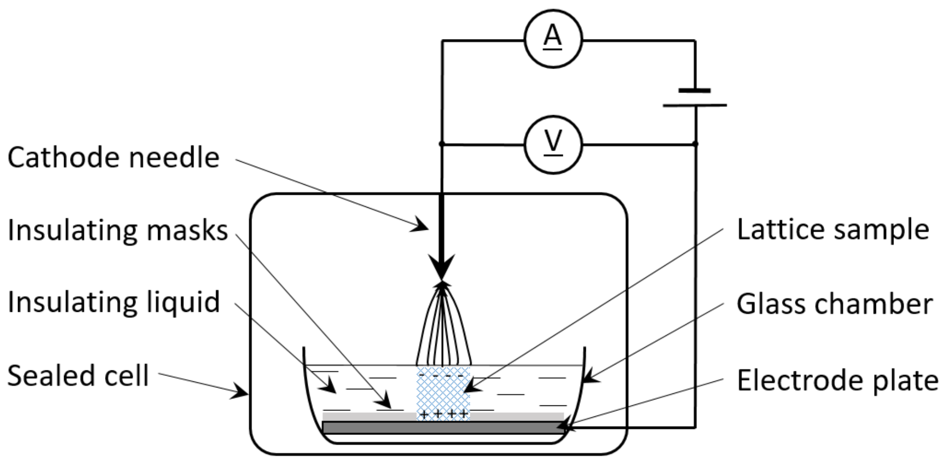

Figure 5-6 Schematic of the experimental setup for the corona poling.

Our testing results for tactile mapping also confirmed good uniformity of the poling process. We prepared an N=12, ϴ=90º lattice with four electrodes attached at different positions across the lattice surface (Fig. 5-7) The electrodes were connected to 4 resistors (10MΩ) with a data acquisition system for reading output voltages from different positions. Identical, calibrated loadings (2.2N) from a shaker (Model V203, Ling dynamic systems LTD) were applied along 3-

direction on the electrodes, the peak voltage generated from four positions were nearly identical, which indicates uniform polarization in lattice upon poling.

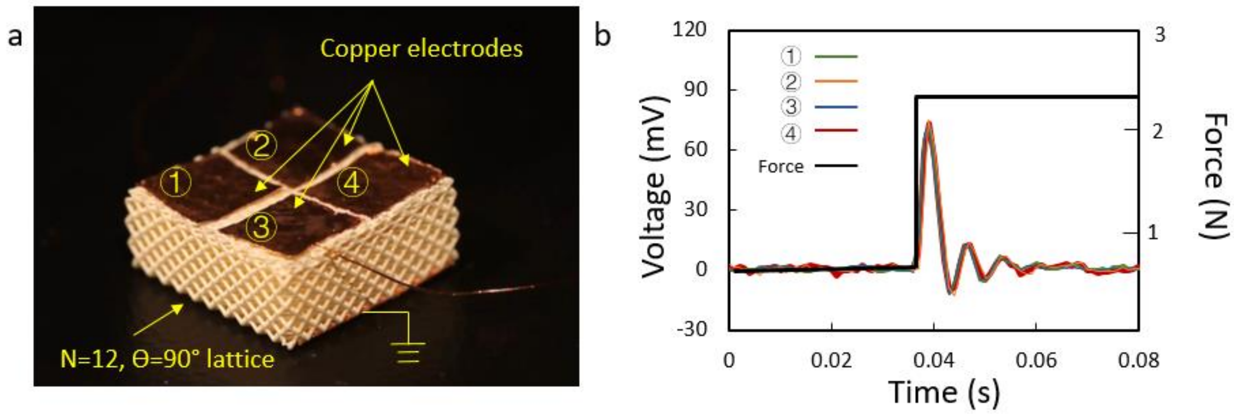

Figure 5-7 a) Optical image of the N=12, ϴ=90º lattice with 4 electrodes attached at different positions. b) Voltage output on the 4 electrodes as a function of time.

5.2.3 Assembly and calibration of the piezoelectric testing apparatus for 3D piezoelectric metamaterials

The piezoelectric metamaterials were first activated by a polarization process in strong electric fields as described in the Method section. After the poling was completed, the electrodes coated with the composite resin was attached to the sample to eliminate triboelectric effects. The sample was compressed with the electrodes to ensure the sample is fully attached to the electrodes (Fig. 5-8a). Leads were connected to the electrodes through copper wires. The sample was put on the top of a high precision force sensor (APPLIED MEASUREMENTS LTD. DBCR-20N-002-000) from which the impact force was read, and a shaker (LING DYNAMIC SYSTEMS, LTD. V203) having a sawtooth voltage input was used to applied impact on the sample. One side of the electrodes was grounded while another side is connected to the circuit shown in Fig. 5-8b[100]. The voltage readout from the circuit was recorded by a data acquisition system (LabView myDAQ) and multiplied by the reference capacitor to calculate the charge generated from the sample. Fig. 5-8d shows the response of the non-polarized and polarized samples with ~0.5N periodic impact force.

The measurement of the piezoelectric coefficient was calibrated using a standard calibration piezoelectric sample provided by APC International, Ltd. Wide-Range Piezo d_{33} Tester Meter. Fig. 5-8c shows the generated charge as a function of impact force for two standard samples having 540pC/N and 175pC/N standard piezoelectric materials. The slope equals the piezoelectric constant. The error of measured results is below 5% comparing with values reported from the manufacturer. Zero voltage output of the non-polarized sample indicates the triboelectric effects have been eliminated from the system.

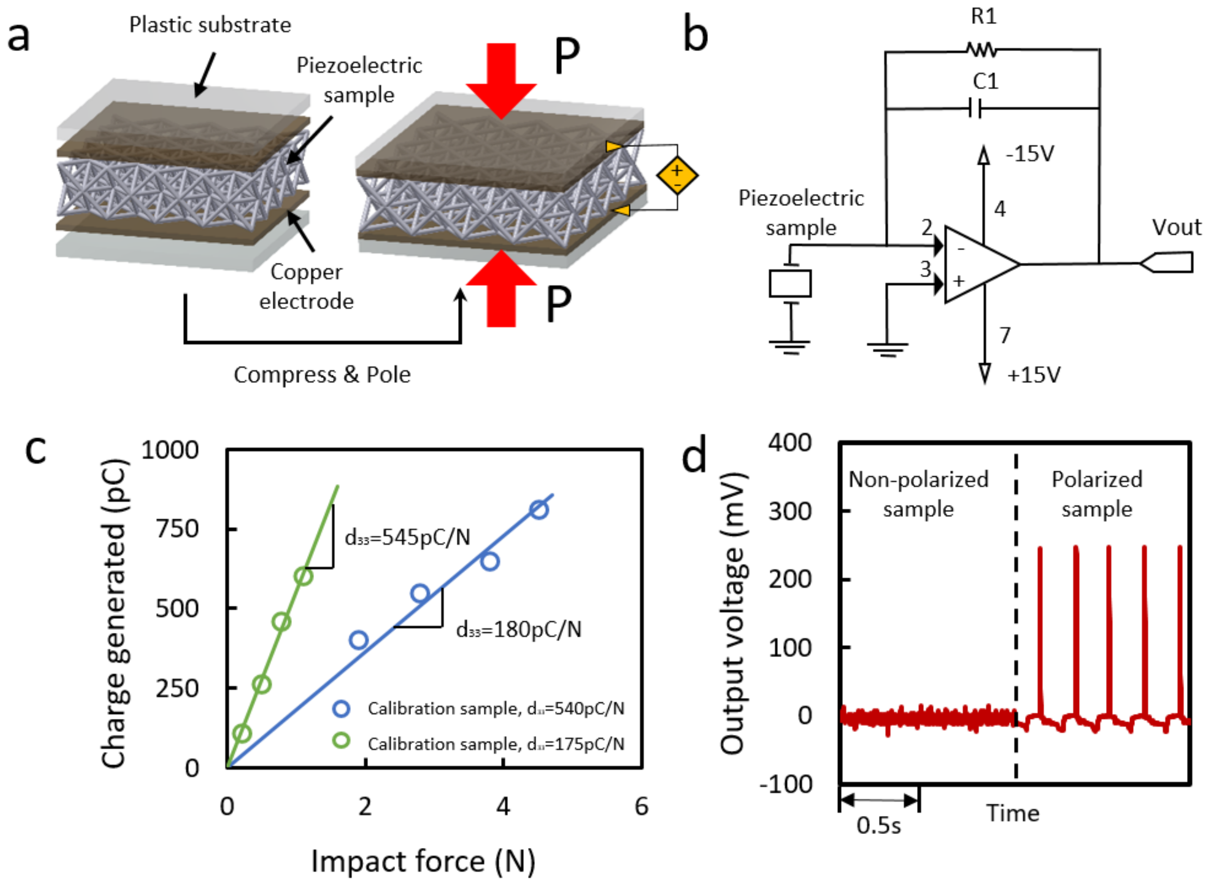

Figure 5-8 Direct piezoelectric coefficient testing and system calibration (a) Schematics of the system setup for measuring piezoelectricity on the as-fabricated architected metamaterials. (b) Circuit diagram for measuring the charges generated from the sample with applied stress. Electric charges generated from the piezoelectric metamaterial are collected by the capacitor, C1 (100pF). The output voltage, V_{out}, is measured through a data acquisition system (NI myDAQ) via R1 (40MΩ). The piezoelectric coefficients of the metamaterials is calculated from $d = (V_{out} \times 100pF)/F_{applied}$. (c) Charge versus applied force plot of two piezoelectric material samples as calibration of the testing fixture whose piezoelectric charge constants are measured by a piezo d_{33} test system (APC International, Ltd. Piezo d_{33} Test System). (d) Voltage output of non-polarized sample and polarized sample under ~0.5N compressive force.

5.3 Applications of the piezoelectric metamaterials

5.3.1 Location sensing

The 3D digital metamaterial building blocks can be further stacked or printed as smart infrastructures capable of time-resolved pressure self-sensing and mapping without application of an external sensor. Here, piezoelectric metamaterials of N=12 are selected and 3D printed into a four-pier piezoelectric bridge with a non-piezoelectric bridge deck (Fig.5-9a, b). The external closed circuits with a data acquisition system are connected to the top and bottom surfaces of the piers to monitor the voltage outputs. The 3D printed piezoelectric metamaterial bridge can directly map the magnitude as well as location of potentially damaging deformations throughout its structure. To demonstrate, steel balls with a mass of 8g are sequentially dropped at random onto the deck. The resulting voltage is collected at each of the four electrodes with the amplitude depending on the electrode proximity. The envelope of the voltage outputs is plotted in Fig. 5-9c, d which independently monitors the strain amplitude. Impact strain map on the deck can be plotted to determine the impact location (Fig. 5-9e, f). These 3D piezoelectric infrastructures allow one to obtain time-resolved self-monitoring information (e.g. displacements, forces, strain mapping) throughout a structure[124, 125] without additional external sensors.

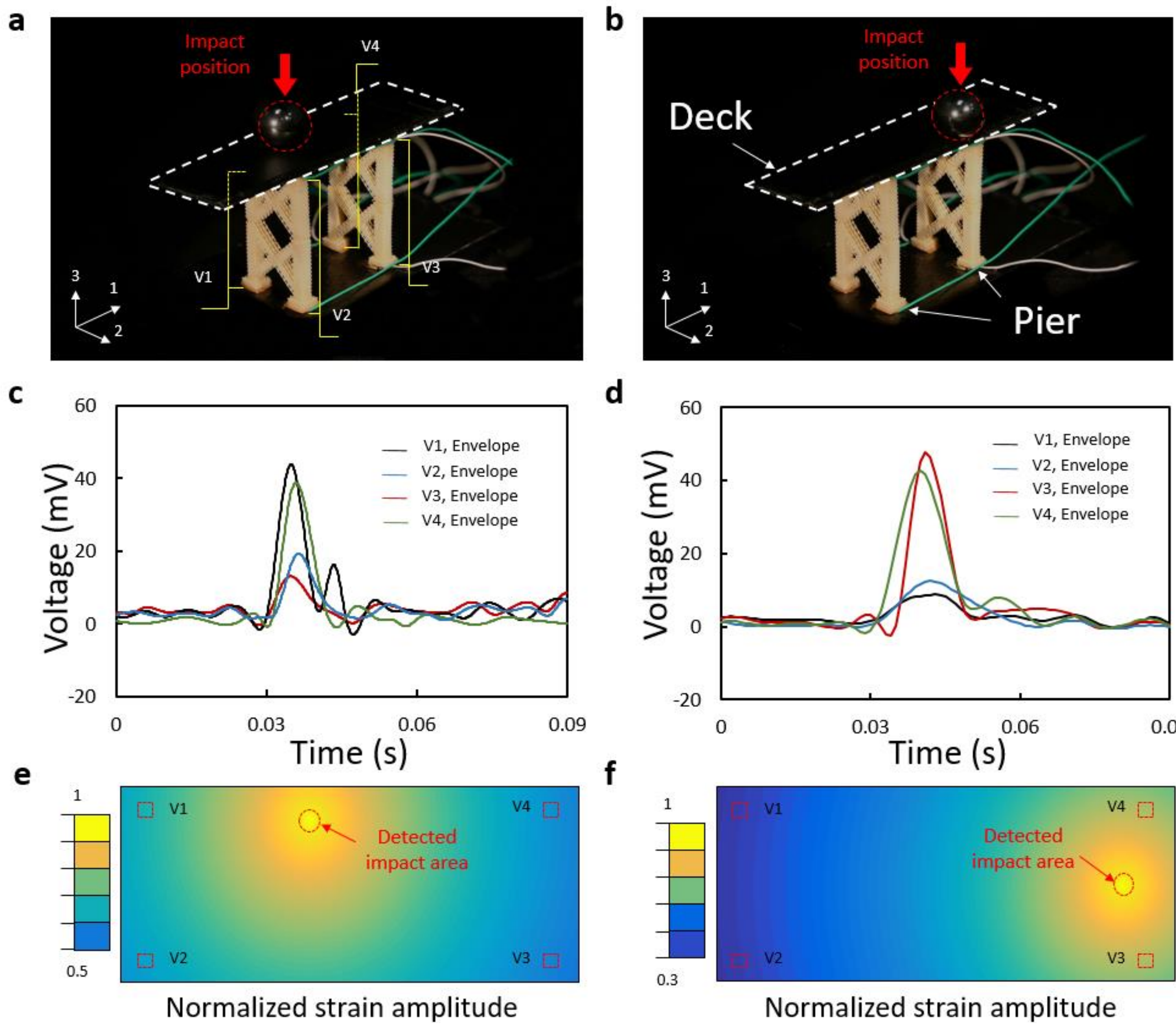

Figure 5-9 Assembly of architected metamaterial blocks as intelligent infrastructures. a-b) Camera image of a self-monitoring 3D printed piezoelectric bridge infrastructure. All four piers are poled together along 3-direction and the electrodes are attached to the top and bottom surface of the piers. The locations of the dropping steel ball are indicated with dashed lines. c-d) Real-time voltage outputs from the self-monitoring piezoelectric piers. e-f) Normalized strain amplitude map converted from the voltage map indicates different locations of the impact.

We first predict the impact point on the bridge-like structure by using four known displacements at the piers and relative positions among piers. A wave propagation and attenuation theory within the planar boundary (the deck) is utilized. The amplitude of the induced response at a given position within the boundary could be simplified to follow an exponential attenuation relation as:

$$u = Ce^{-Dr} \; (5-1)$$

, where u is the induced response amplitude (displacement) of the point of interest (at the pier), C and D is a coefficient depending on the amplitude of the impulse and the damped frequency of the deck, r is the distance between the pier and the impact point. To obtain the displacements at four piers, the proportional relationship between peak voltage output and pier displacement is used due to the linear deformation of the piers:

$$u = A \cdot V_{peak} \quad (5-2)$$

, where A is the coefficient of proportionality, V_{peak} is the peak voltage output at the pier. Combining Eq. (5-1) and Eq. (5-2) yields the direct relationship between voltage output and distance r. A coordinate system is then set originating from pier 1, and therefore, the coordinates of each pier are defined (Fig. 5-10). Let the unknown impact point as (x, y), with four r's in terms of voltage outputs given by Eq. (5-1) and Eq. (5-2), four relationships between r's and (x, y) are denoted as:

$$r_k^2 = (x - x_k)^2 + (y - y_k)^2 \quad (S13.3)$$

, where r_k is the distance between k-th pier and the impact point, x_k and y_k are coordinates of the k-th pier, $k = 1\sim4$. With four circles defined by Eq. (5-3), one intersecting point (i.e., impact point (x, y)) is determined while the maximum displacement induced by the impact force is also determined. By knowing the impact point, using Eq. (5-1), the strain at each point on the deck normalized by the maximum strain is thus solved.

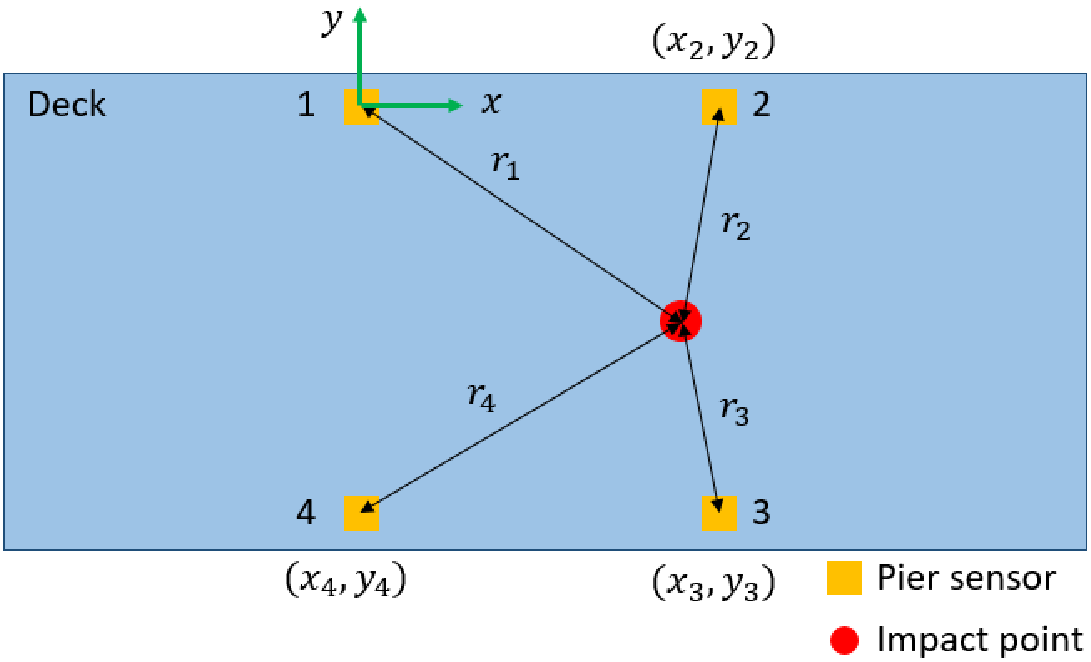

Figure 5-10 Geometric relationship between impact point and pier locations for determining the location of the impact point.

5.3.2 Directionality sensing

Taking advantage of the distinct directional d_{3M} design space, stacking multiple piezoelectric building blocks, each with a tailored directional response, allows one to program the voltage output patterns as binary codes, i.e. *positive* or *negative* voltage. These stackable metamaterial blocks provide a unique method to determine directionality which we leverage to sense pressure from arbitrary directions[126]. Fig. 5-11a shows the directionality sensing concept using sensing infrastructure assembled from an array of piezoelectric metamaterial cubes with pre-configured d_{3M} tensor signature $\{d_{31}, d_{32}, d_{33}\}$ distributed at different quadrants. Piezoelectric metamaterial cubes on the outer surface of the cube (①~⑤ surfaces) are connected to voltage output channels, with intersecting faces of the cube sharing one voltage output channel (see Fig. 5-12 for details). Pre-program stacked d_{3M} combinations with each face of the cube allows the output voltage binary map to be uniquely registered with a given pressure applied on that face. The direction and magnitude of any arbitrary force can then be super-positioned and determined from the collected voltage maps (Fig. 5-11a).

As a proof-of-concept demonstration of directionality sensing, we stacked a piezoelectric metamaterial infrastructure comprised of four cubic units with their unique 3D piezoelectric signatures by design (Fig. 5-11b, c). The output voltage binary map uniquely registers the corresponding force direction. When impacted from 1-, 2- and 3-direction (labeled as I, II, III, IV, Fig. 5-11d), three distinct voltage outputs are detected each correlated with the original respective impact direction (Fig. 5-11d). The impact force in 1-direction is registered with permutation voltage matrix [-, -, +, +], while [+, +, -, +] for 2- and [-, -, -, +] for 3-direction, respectively (Fig. 5-11d). These digitalized, binary output voltage maps originated from the preconfigured piezoelectric constant signatures decode directionality of the impact as well as its magnitude.

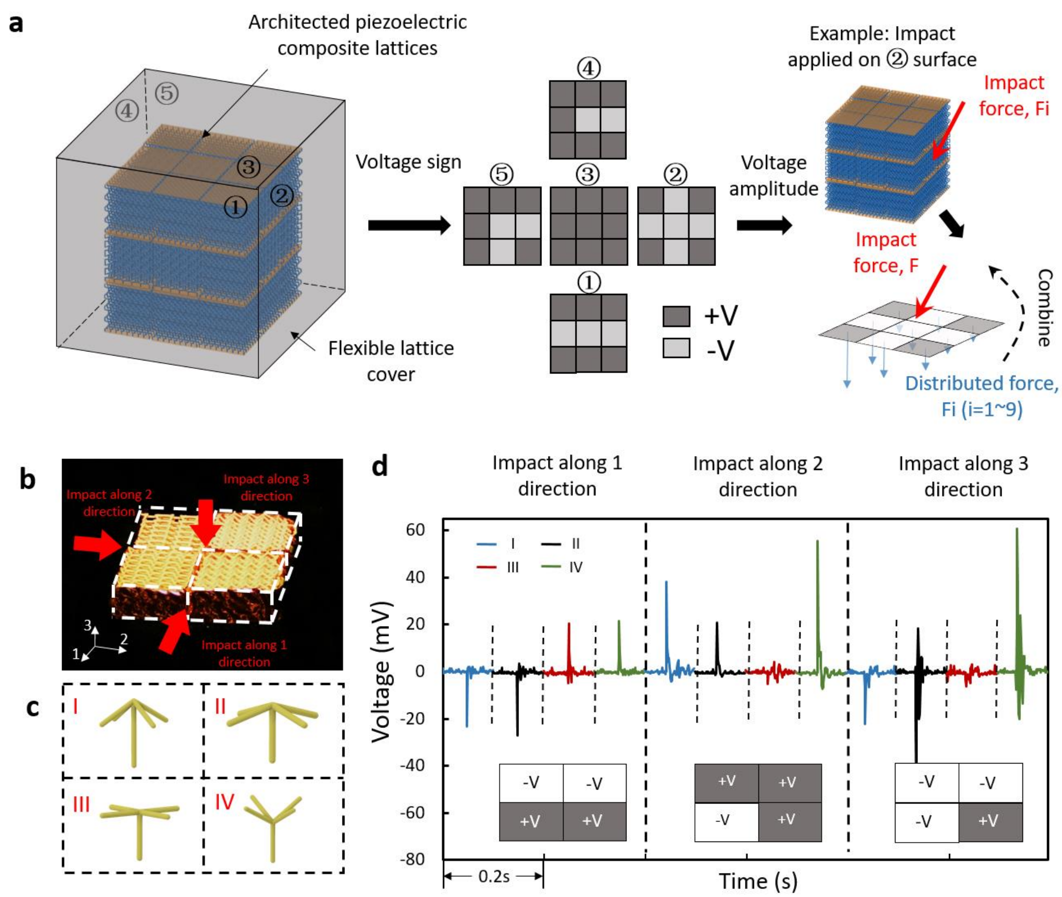

Figure 5-11 Force directionality sensing. a) Illustration of force directionality sensing application using piezoelectric metamaterials stacked from four types of designed building blocks to achieve arbitrary force directions. b) As-fabricated piezoelectric infrastructure comprised of stacked architectures with encoded piezoelectric constants. c) Voltage output patterns corresponding to different impact directions indicated by red arrows. The insets show the binary voltage patterns registered with different impact directions. The impact force in 1-direction is registered with permutation voltage matrix [-, -, +, +], while [+, +, -, +] for 2- and [-, -, -, +] for 3-direction, respectively.

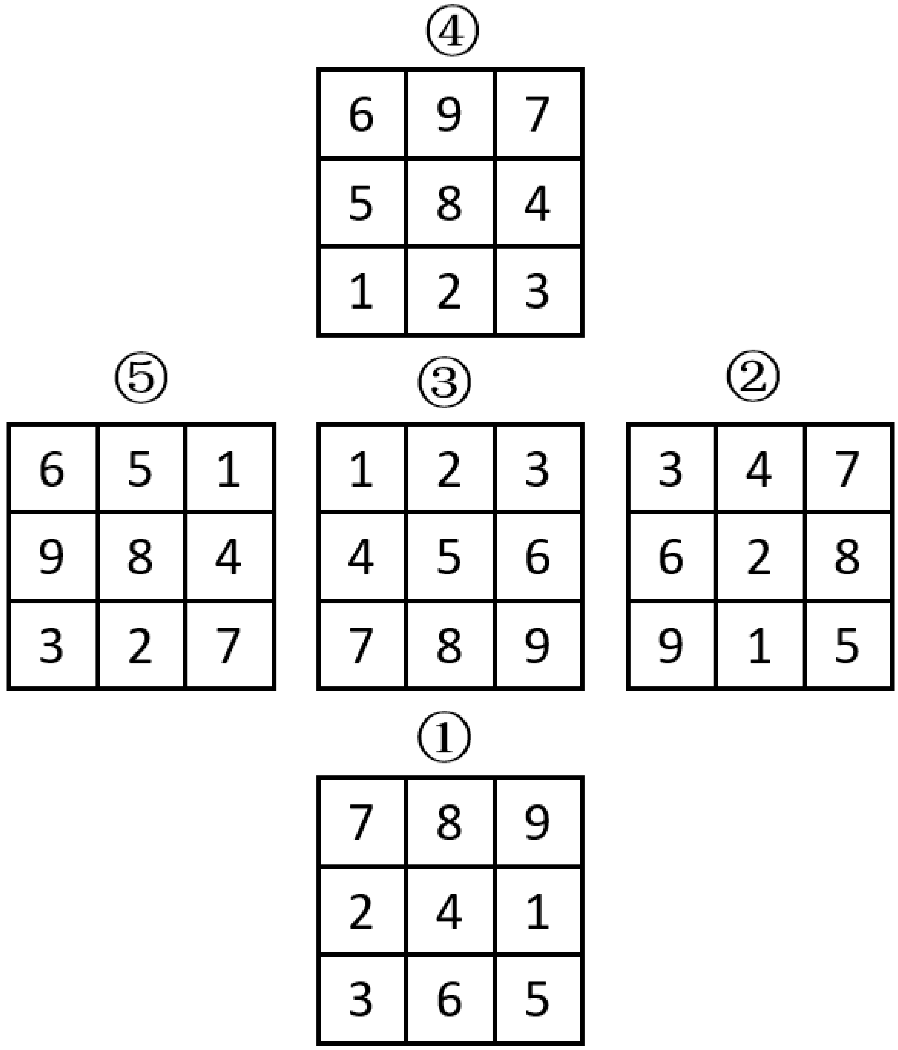

Figure 5-12 Schematics of the wiring method of the spatial stacking of multiple piezoelectric building blocks. The 25 building blocks are connected to 9 voltage channels of a data acquisition system (NI USB-6356). The blocks labelled as the same number are parallel and connected to the same voltage channel.

5.3.3 Tailorable compliance and sensing on a curved surface

Fig. 5-13 shows the compliance measurement of the metamaterial having different relative densities and monomers with different elasticity. These metamaterials were compressed using INSTRON-5944 with 0.05/min strain rate. The compliance is calculated from the reciprocal of the slope of the stress-strain curve. The testing results show that these groups of piezoelectric metamaterials possess tailorable compliance over three orders of magnitude. Fig. 5-14 shows the voltage output of a flexible piezoelectric metamaterial when it is attached to a curved surface and compressed by fingers.

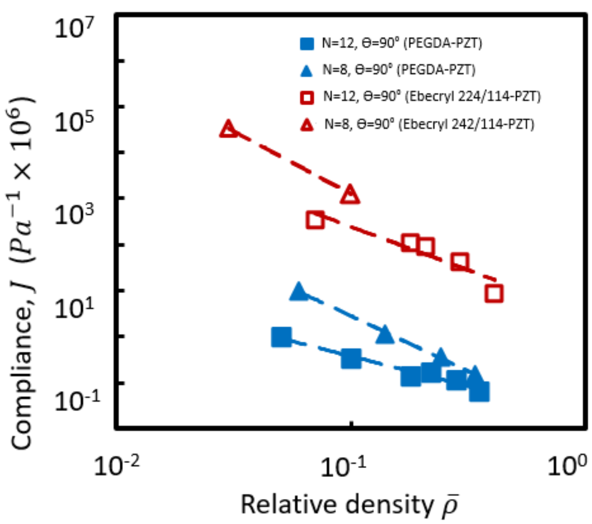

Figure 5-13 The tunable elastic compliance as a function of the relative densities.

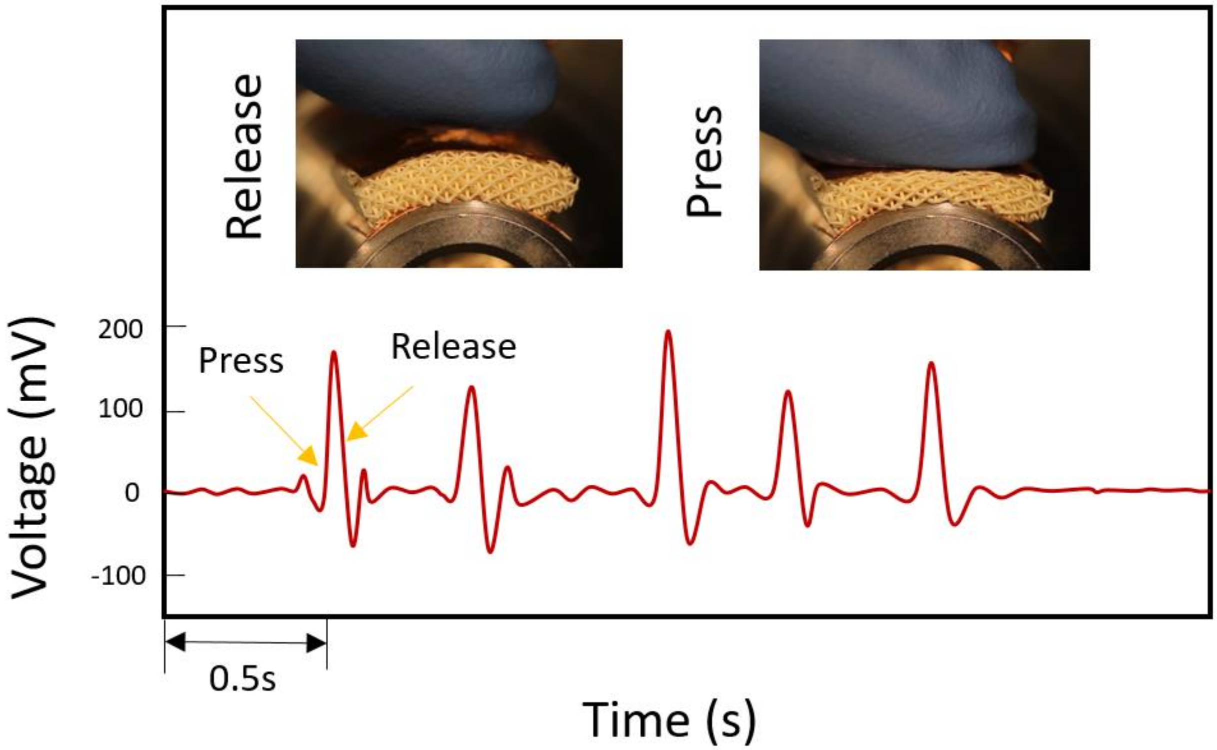

Figure 5-14 Hand tapping induced voltage response of the N=12 flexible piezoelectric metamaterial conformally attached to a curved surface.

5.3.4 3D architected flexible tactile sensor

As shown in Fig. 5-15a~b, the 3D architected piezoelectric metamaterial can be stretched and bent by fingers with ease without fracture, and are highly conformable to different shapes, e. g., fingers and joints, suggesting their applicability in wearable devices and skin-like sensors. As a demonstration, a ring-like sensor was prepared and tested to show the voltage output during the folding and unfolding process of the author's little thumb, as shown in Fig. 5-15c~d. When the finger was folded, the architected sensor is under 3-3 working mode, which means the pressure is applied along the 3-direction (polarization direction) and the voltage is generated on the electrodes along the 3-direction. Fig. 5-15e displays the real-time waveforms of the folding and unfolding pressure pulse recorded from the sensor.

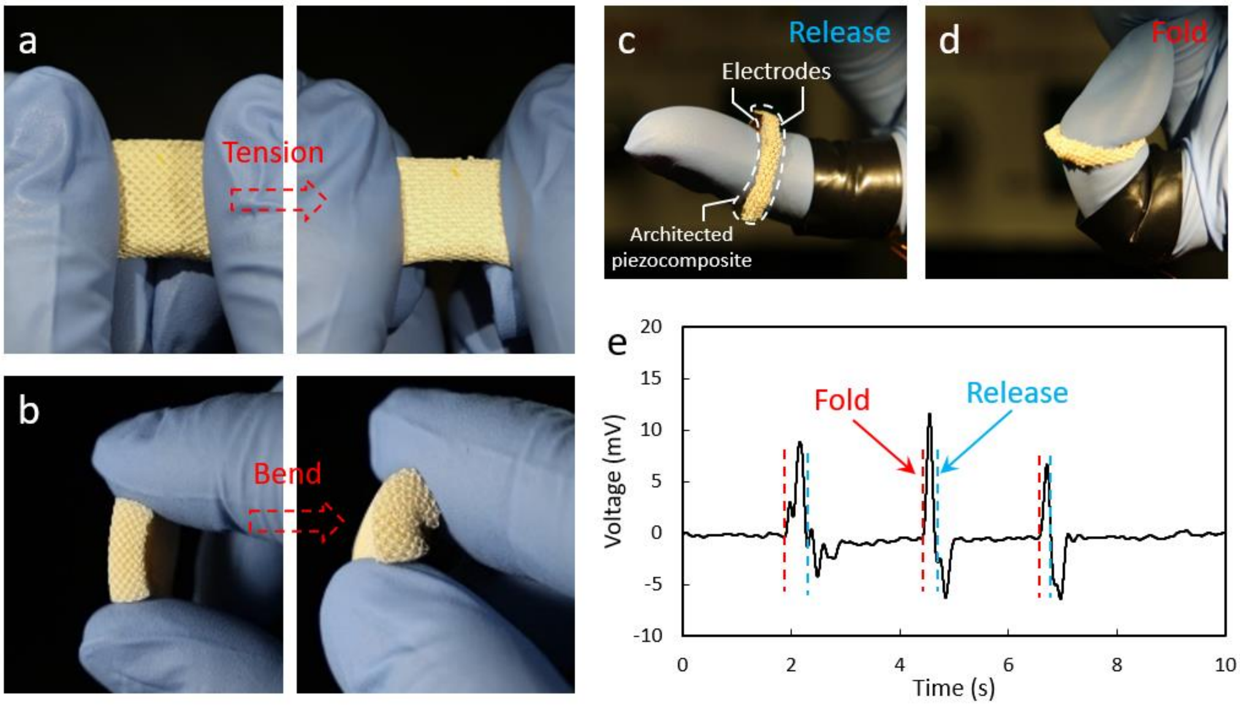

Figure 5-15 a~b) The optical images of the flexible 3D architected piezoelectric composite sensor with the N=12, ϴ=90° structural design. Tensile and bending forces are applied to the lattice by fingers, showing mechanical flexibility. c~d) A ring-like flexible 3D architected sensor attached to the finger. The sensor is compressed during the "fold" status of the finger. e) Voltage generated from the sensor during three cycles of finger folding and unfolding.

5.3.5 Energy generation and stability of the piezocomposite energy harvester

To demonstrate the energy harvesting capability of our piezocomposite, we used the piezoelectric metamaterial to harvest energy from the external impacts. An architected film with 40% porosity was printed using the 50vol% PZT composite, as shown in the inset of Fig. 5-16a. The as-fabricated sample was then poled with a 4V/um electric field under room temperature for 1 hour.

After poling, two silver electrodes with cables were attached to the sample to form the piezoelectric energy harvester.

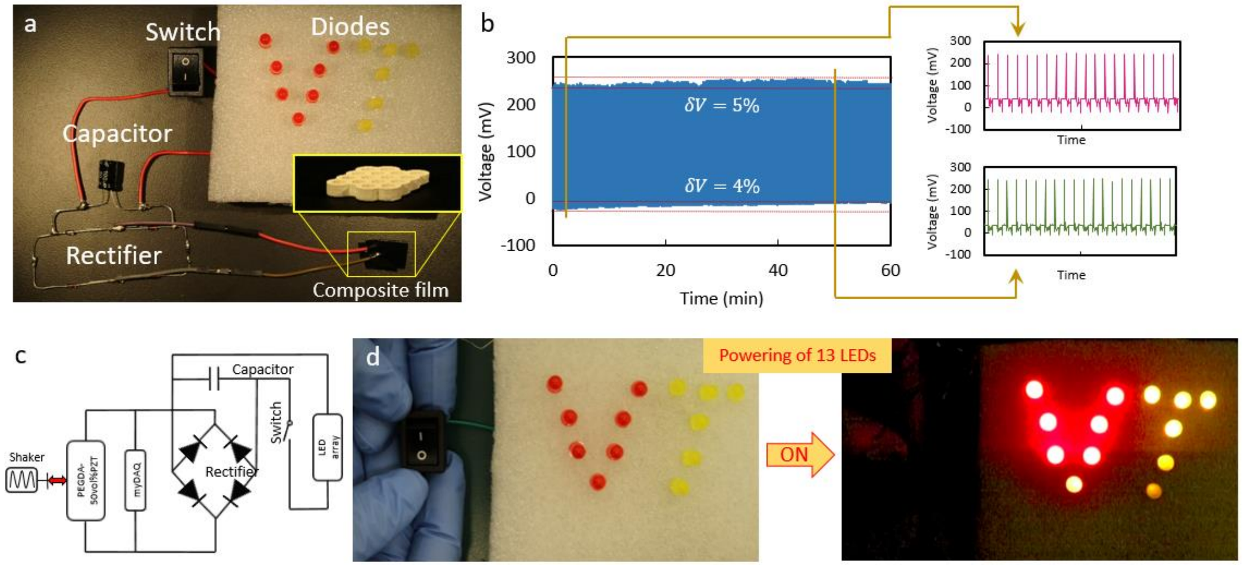

Figure 5-16 Energy Harvesting Experiment a) Camera image of the energy harvesting setup with architected piezoelectric metamaterial film. b) Energy generation and stability of the generator over time with voltage output. The result of the voltage output durability test over 60 min for verification of the energy harvesting stability. The magnified views of the regions highlighted by yellow lines represent clear and stable generated output voltage from the energy harvester. c) Schematic circuit diagram for measuring the output performance of the energy harvester. d) A photograph of the LED signboard with 13 high-intensity LEDs powered by the energy harvester.

A rectifier and charge storage circuit including the bridge rectifier, a capacitor (C=100μF), a switch and the LED array were connected to the piezocomposite energy harvester, as shown in Fig. 5-16a&c. A shaker with an integrated force sensor in contact with the surface of the energy harvester applied a small cyclical loading (~1N peak to peak) on the sample. The generated voltage was measured through myDAQ, while the generated charge was stored in the capacitor. The voltage output of the harvester was relatively stable over 360000 cycles, as shown in Fig. 5-16b. We observed a small variation in the generated voltage ($\delta V = 7 \sim 8\%$), showing the stability of our piezoelectric composite. The stored energy was then used to illuminate a pattern formed by 13

LEDs. Fig. 5-16d shows the illumination of the LEDs after turning on the switch between the capacitor and the LED pattern. The LEDs are illuminated for 0.5s with a 2.85V voltage (U) on the capacitor.

5.4 Discussion and outlook

We have presented 3D piezoelectric metamaterials with piezoelectric polarization tailorable from virtually all directions relative to applied stress. The concept is based on designing electric displacement of strut members within periodic nodal structures of given connectivity and then tessellate them in three-dimensions, forming 3D architected piezoelectric metamaterials. We see this as a step toward rationally designed 3D piezoelectric materials for which we can choose specific components of the effective piezoelectric coefficient tensor through configuring topology. We implement the concept through additive manufacturing of photo-sensitive piezo-nanocomposite feedstock to create 3D piezoelectric metamaterials with any free-form architectures. The poling process on the as-fabricated metamaterials in one direction activates the piezoelectricity described by the designed piezoelectric coefficient tensor. Experimental measures confirm exceptional voltage constant and voltage coefficient at low volume fractions. This allows several previously unachievable opportunities. Metamaterial blocks are assembled or 3D printed into bulk infrastructures capable of self-monitoring pressure, directionality sensing and location mapping. The 3D piezoelectric lattice structures decouple several distinct physical attributes to achieve: 1) high specific piezoelectric voltage constants via a fraction of active piezoelectric materials; 2) tunable compliance across three-orders of magnitude; and 3) filling the white space unoccupied by conventional porous piezoelectrics, flexible piezoelectric composites and polymer. The developed method and highly concentrated piezoelectric feedstock can be adapted to virtually any commercially available light-based 3D printing platforms, allowing potential new generation of smart infrastructure, force sensing and impact shielding applications. This tailorable system opens new opportunities to tune final structural compliance and electro-mechanical coupling coefficients, for applications ranging from soft, stretchable, skin-like sensor arrays and energy harvesting to more robust, structural materials integratable as sensors into fixed buildings.

Chapter 6 Additive manufacturing of micro-architected underwater transducers

6.1 Hydrostatic figure of merit of the architected piezoelectric metamaterial

While the mechanical properties (strength, stiffness) in architected metamaterials scale down with volume fractions, creating volume fractions (low relative density) in these piezoelectrics invoke many unique advantages for piezoelectric properties as compared to their bulk material[3]. Based on the design theory, d constants are not sensitive to relative density in the linear elastic regime, therefore at low volume fractions, their mechanical-electro coupling factors remain consistent with higher volume fractions of the same architecture. Our study has found that, the piezoelectric voltage constant, g, another key piezoelectric property constant, increases with the reduction of relative density and outperform their original starting material. g constant is the most relevant piezoelectric constant characterizing electro-mechanical coupling for transducer and sensor performance[127]. The g_{33} constants are related with d_{33} and electric permittivity via,

$$g_{33} = \frac{d_{33}}{\varepsilon_{33}}$$

where d_{33} and ε_{33} are the piezoelectric charge constant and permittivity in the 3-direction, respectively. The permittivity of the lattices has a nearly linear relationship with the relative density and can be calculated using the following equation[128]:

$$\varepsilon_{33} = [\bar{\rho}(k_c - 1) + 1]\varepsilon_0$$

where $\bar{\rho}$ is the relative density of the lattices, k_c is the dielectric constant of the bulk composite and ε_0 is the permittivity of vacuum. For the bulk composite, the relative density can be considered as 1. The relationship between the permittivity and relative density was further verified using a commercial capacitance meter (KEYSIGHT, E4990A). The capacitance of the lattices was measured, and the permittivity can be calculated from the following equation:

$$\varepsilon_{33} = \frac{Cd}{A}$$

where C is the capacitance of the lattice, d is the distance between the electrodes and A is the cross-section area of the lattice.

As a result, it can be seen that the lower electric permittivity inherent within the piezoelectric metamaterials contributes to the increased piezoelectric voltage constant g. For example, the g_{33} constant of the N=12, Θ=90° lattices increases as the relative density decreases, as plotted in Fig. 5-3d. Therefore, the voltage constants of the low relative density lattices outperform that of the bulk composites, indicating superior sensing capabilities.

Additionally, these micro-architected metamaterials outperform its base material and other piezoelectric materials regarding their hydrostatic properties. For hydrophone applications, an important parameter is the hydrostatic figure of merit (FOM)[129], which defines the material's suitability for underwater sonar applications,

$$FOM = d_h \cdot g_h \ (Pa^{-1})$$

where,

$$d_h = d_{33} + (d_{32} + d_{31})(CN^{-1})$$

$$g_h = \frac{d_h}{\varepsilon}(Vm^{-1})$$

As shown in Fig. 6-1, the FOM of the piezoelectric metamaterials can be tuned in a large range by tuning the piezoelectric anisotropy via architecture and exceeding other piezoelectric materials and other piezoelectric foams[114, 129-135]. This beneficial property is attributed to, i) through changing the micro-architectures, the anisotropy of the d and h constants of these piezoelectric metamaterials can be tuned from {-, -, +} to {+, +, +} leading to the increase of d_h. ii) higher overall g_h at lower densities as compared to the base material and other piezoelectric materials, attributed to the low electric permittivity ε. This benefit of lower densities (e.g., lower permittivity) also validates predictions obtained from piezoelectric foam structures.

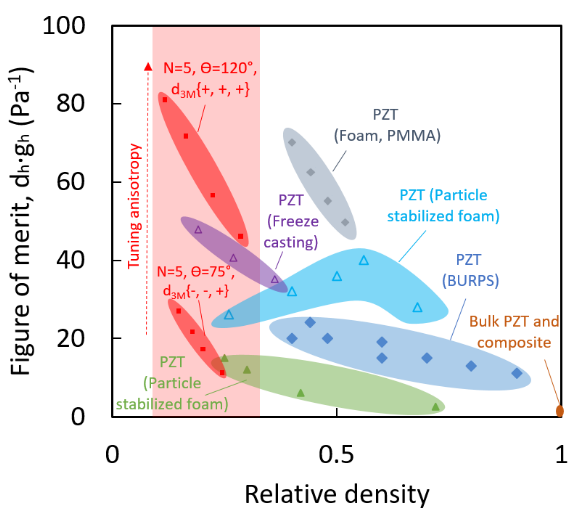

Figure 6-1 FOM of porous and bulk piezoelectric materials.

6.2 A novel multi-material system for the printing of piezoelectric transducers and high-performance multi-material packaging

A novel multi-material projection stereolithography system enabled the fabrication of both the "green part" of the transducer elements (directly printed piezocomposite without post-processing such as sintering) with particle loading up to 50vol% and the packaging materials which includes acoustic matching material, conductive material, backing material and the encapsulation. A schematic of the multi-material is shown in Fig. 6-2a. The system consists of a multi-material feeding system and a projection stereolithography system which solidifies UV curable resin in a layer-by-layer manner. The system is highly versatile and can print a broad range of materials including highly loaded nanoparticle composites (lead zirconate titanate (PZT), silver (Ag), carbon fiber) and polymers with various Young's modulus (5kPa-5GPa) and acoustic properties.

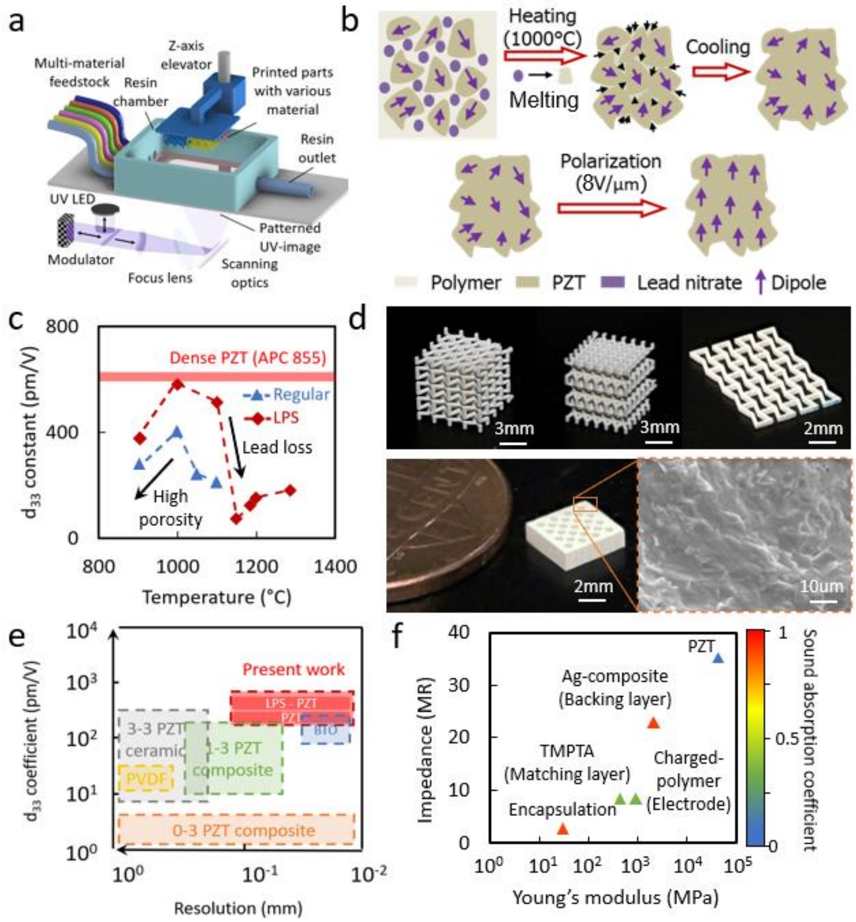

Figure 6-2 a) Schematic of the novel multi-material 3D printing system. b) Schematic of the LPS process and polarization process. c) Comparison of the d constant between the piezoelectric material sintered with conventional sintering method and LPS method under various temperatures. d) Optical image of as-fabricated piezoelectric ceramic transducer elements with microarchitectures and low porosity. e) Benchmark d coefficient with the state-of-art 3D printed piezoelectric materials. f) Summary of impedance, Young's modulus and sound absorption coefficient of materials used for the packaging and transducer.

To achieve high-resolution additive manufacturing of piezoelectric materials, we first investigated the printing of high-loading nanoparticle colloids, as aforementioned in Chapter 4. We achieved minimum printable 3D feature size of ~20μm with up to 50vol% (86wt%) nanoparticle loaded composite, which is named as the green part of the sintered piezoceramics. The green composite is functional as a piezoelectric transducer, and we also investigated sintering the 3D printed nanocomposites to form dense ceramic samples with a higher response. Typical 3D printed composite sintered samples suffer from high porosity and low mechanical and piezoelectric performances. We exploited the liquid phase sintering (LPS) method to reduce the porosity of the sintered sample (Fig. 6-2b), and by using an optimized temperature profile, we achieved sintered samples with over 97% density of the solid piezoelectric materials (Fig. 6-2d). Utilizing the optimized liquid phase sintering method, we increased the piezoelectric coefficient of the sintered parts by ~3 times compared to that of regularly sintered samples (Fig. 6-2c). Fig. 6-2e compares the piezoelectric coefficient, d33, and the fabrication resolution of 3D printed piezoelectric materials including ceramics, polymers and composites, showing our approach outperforms state-of-art methods in terms of fabrication resolution and piezoelectric coefficient.

The packaging of the underwater transducers consists of various materials that have specific properties required by their functionality. For instance, the packaging of ultrasonic transducers includes matching layer, backing layer, conductive leads and flexible encapsulation. The matching layer requires impedance between water and the PZT element and low sound absorption factor. The backing layer requires high stiffness and high absorption factor. The electrode material needs to be highly conductive and have minimal effect on the thickness of the matching and backing layer. The packaging material requires high flexibility so that the ultrasonic transducer can accommodate various situations and form conformal shapes. Additionally, the electrode and leads arrangement becomes extremely complicated when there is a large number of transducer elements in an array (10 x 10 array requires 101 leads at least). Our multi-material fabrications system provides us the opportunity to fabricate various materials through one-time printing and simple post-processes. Fig. 6-2f summarizes the impedance, Young's modulus and sound absorption coefficient of printable materials, including PZT as sensing element, Ag-composite as backing layer, TMPTA as matching layer, charged-polymer to direct copper (Cu) deposition for electrodes and FLEX (a highly flexible urethane acrylate blend) as encapsulation.

Utilizing our fabrication system, we describe the successful design, 3D printing, and demonstration of a series of self-powered micro-architected underwater transducers with various micro-architecture designs and frequency responses covering both the low-frequency range (50kHZ~100kHz) for underwater communication (hydrophone) and high-frequency range (500kHz~4MHz) for ultrasonic imaging.

6.3 Fabrication and characterization of micro-architected hydrophones

6.3.1 Design of micro-architectures of the hydrophones

As shown in Fig. 6-3a-b, the FOM of the piezoelectric metamaterials can be tuned in a large range by tuning the piezoelectric anisotropy via architecture and exceeding other piezoelectric materials and other piezoelectric foams. This beneficial property is attributed to, i) through changing the micro-architectures, the anisotropy of the d and h constants of these piezoelectric metamaterials, {d_{31}, d_{32}, d_{33}}, can be tuned from {-, -, +} to {+, +, +} leading to the increase of d_h. ii) higher overall g_h at lower densities as compared to the base material and other piezoelectric materials, attributed to the low electric permittivity.

Utilizing the microarchitecture designs in our previous study, we fabricated hydrophones with high sensitivity and characterized their performance. Fig. 6-3c shows the 3D printed assembly of our hydrophones. Copper deposited electrodes were used to cover the upper and bottom of the sintered

PZT lattices, which were then polarized under 8V/um electric field. Two layers of packaging were printed on the multimaterial system with PEGDA to package the lattice. Between the two layers of packages, there's a selectively deposited copper mesh layer to eliminate the underwater RF noises and reduce the noise floor during the data acquisition process. Copper leads were used to connect the hydrophone with cables. Although made of polymer and piezoelectric ceramics, acoustically, the as-designed hydrophone assembly behaves similarly to water, due to the high porosity and lightweight design, inducing ultra-low pressure loss caused by reflection and refraction.

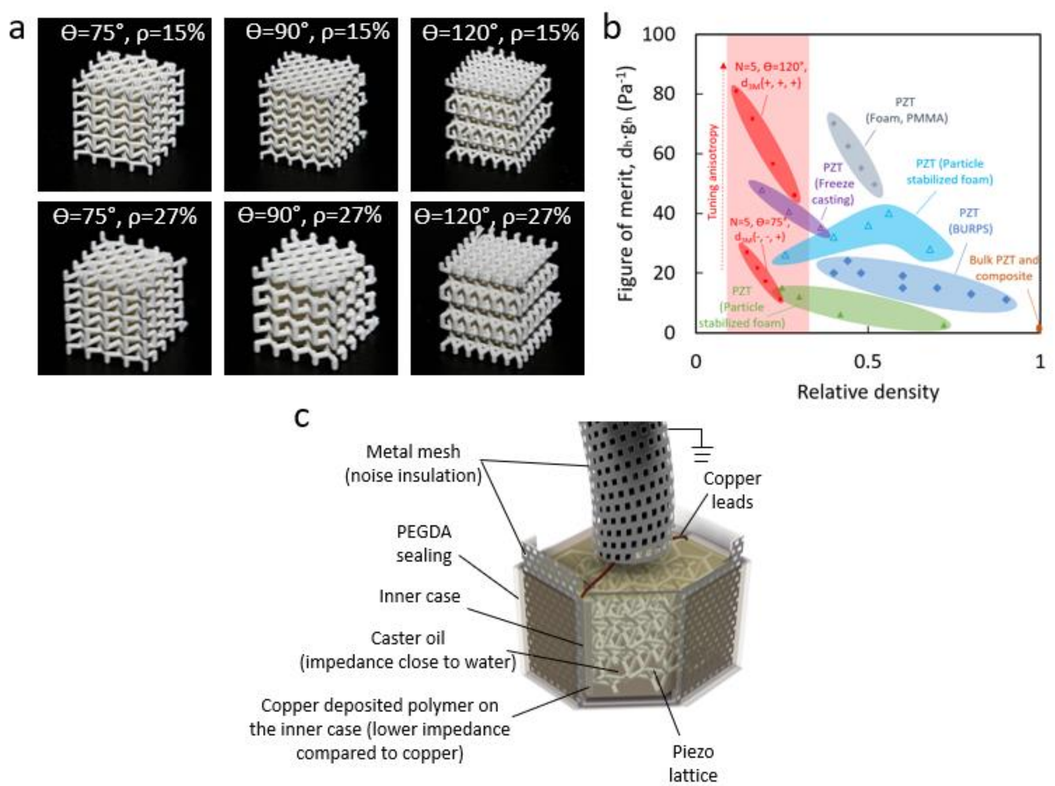

Figure 6-3 a) Optical image of the as-fabricated piezoelectric hydrophone sensing elements with various micro-architecture designs. b) Comparison of hydrostatic figure of merit of different sensing elements. c) Schematic of the packaging of the hydrophones.

6.3.2 Characterization of the hydrophones

For preliminary testing, the hydrophones were placed in a large water pool with 5m diameter and 1.5m depth. A commercial piezo speaker (Kemo L010) was used to generate underwater pressure and one of our hydrophone (with screw angle of 90 degree and relative density of 27%), along with a commercial hydrophone containing piezoelectric ceramic sensing elements, were both placed on the opposite side of the water pool, as shown in Fig. 6-4. A sweep voltage with 100Hz to 10kHz frequency was input to the piezo speaker through a function generator and a voltage amplifier. The voltage output of our hydrophone (blue curve) and the commercial hydrophone (red curve) was recorded by an oscilloscope. Fig. 6-4 shows that our hydrophone has higher voltage output within the testing frequency range and outperforms the commercial hydrophone with a dense piezoelectric sensing element.

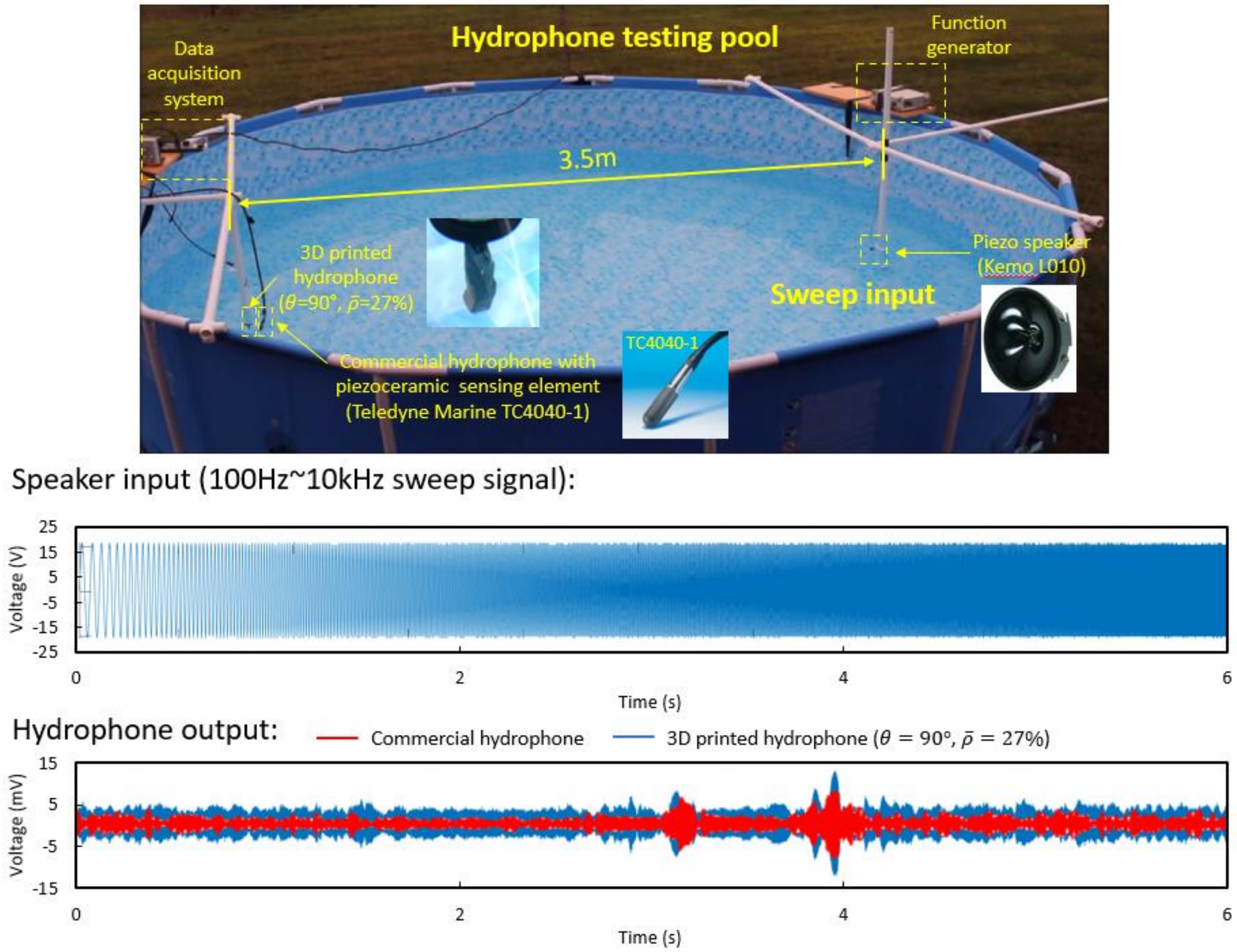

Figure 6-4 Optical image of the testing set-up, speaker sweep input voltage plot as a function of time and hydrophone outputs as a function of time.

To further characterize the performance of our hydrophones, a testing frame was set up with adjustable distance and angle between the hydrophone and the underwater speaker. A function generator was used as the power supply of our hydrophone and a commercially available amplifier was used to magnify the voltage signal and feed to an oscilloscope for data acquisition.

Fig. 6-5a demonstrated the testing fixture and methods of measuring the sensitivity and working range of our hydrophones. To measure the sensitivity of our hydrophone, a standard hydrophone was used as a reference to capture the underwater pressure by the following equation:

$$p_0 = \frac{V_0}{10^{\frac{M_0+120}{20}}}$$

where V_0 is the voltage reading and M_0 is the sensitivity of the commercial hydrophone. The sensitivity of the architected hydrophone was then calculated by

$$M_h = 20\log\left(\frac{V_h}{p_0}\right) - 120$$

where V_h is the voltage reading from the architected hydrophone. During testing, a sweep signal input (1Hz~100kHz) was used for the commercial speaker with a duration of 60s. The signal from the standard hydrophone and the architected hydrophone was captured and recorded.

Fig. 6-5b and Fig. 6-5c summarize the working range and sensitivity of architected hydrophones with various geometrical designs, respectively. By adding micro-architectures to the piezoceramic sensing element, we can achieve higher sensitivity and a larger range of tunable frequencies compared to commercially available hydrophones with solid sensing elements.

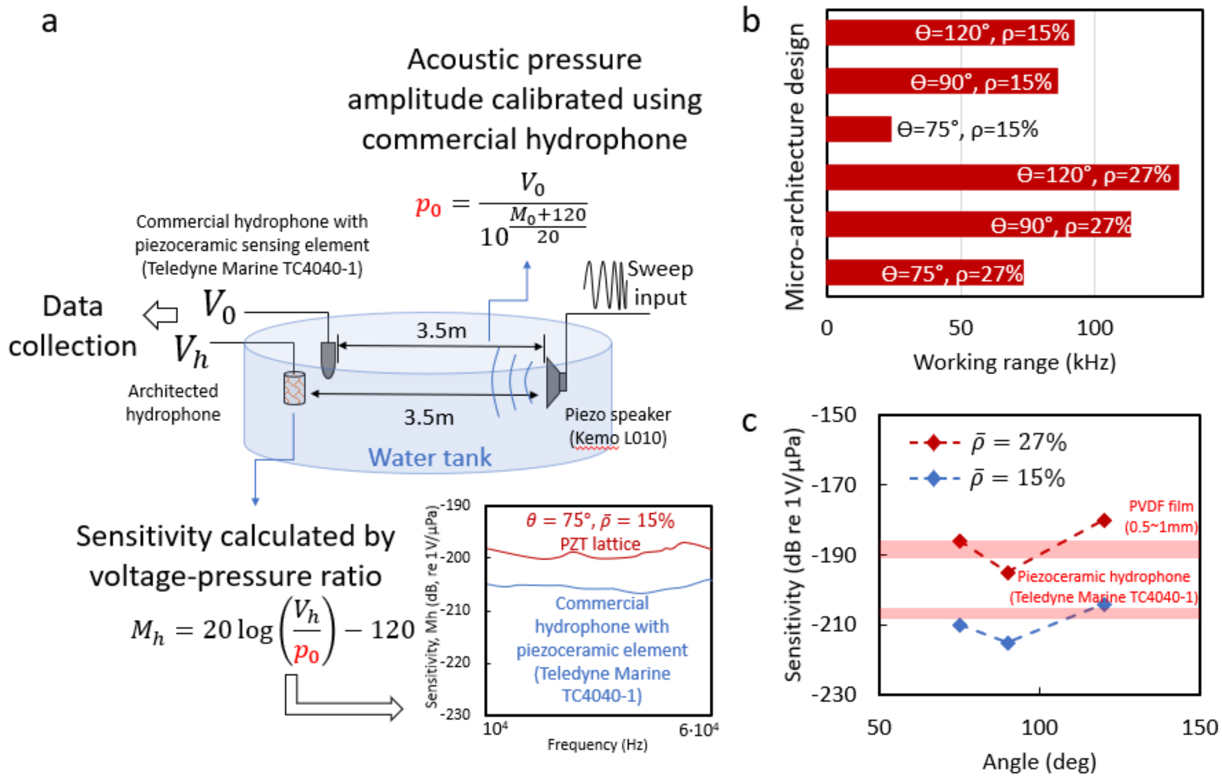

Figure 6-5 a) Schematic of the process of sensitivity measurement and working range measurement. The sensitivity of the hydrophones starts to drop when the input frequency is higher than the resonant frequency of the sensing element. We use -5dB threshold to define the dropping point and define the working range as frequencies lower than the dropping point. b-c) Working range and sensitivity of micro-architected hydrophones with representative micro-architecture designs.

6.3.3 Rational design of the directivity patterns of the hydrophones

With our advanced fabrication capabilities, various micro-architectures with different sensitivities and working ranges can be combined into one hydrophone having rationally designed directivity patterns. Unlike earlier works that used hydrophone arrays, in this work, single-piece hydrophone can achieve the desired directivity pattern, which reduces the circuit complexity and noise range. From the previous sections, we know that the sensitivity of architected hydrophones varies with micro-architecture designs and covers a range of -215dB to -180dB. Taking the advantage of our fabrication capability, we can combine lattice designs with various sensitivities to form hydrophones with controlled directivity pattern, since the sensitivity of the hydrophone can be controlled through micro-architectures. To test the directivity pattern, the hydrophone was placed at the center of the water tank. The commercial speaker was placed in various directions of the hydrophone to generate sound pressure. The sensitivity of the hydrophone in various directions was then calculated.

Fig. 6-6 shows the optical image of two architected hydrophones with a designed beam pattern. The hydrophone combined $\theta = 120°$, $\bar{\rho} = 27\%$ and $\theta = 90°$, $\bar{\rho} = 15\%$ architecture designs having a sensitivity of -204dB and -195dB. The directivity pattern is plotted in Fig. 6-6, respectively. The directivity pattern shown on the left can be used for underwater communication since it eliminates the noise from the surface reflection and seafloor reflection, while the directivity pattern shown on the right can be used to detect underwater pressures from a specific direction.

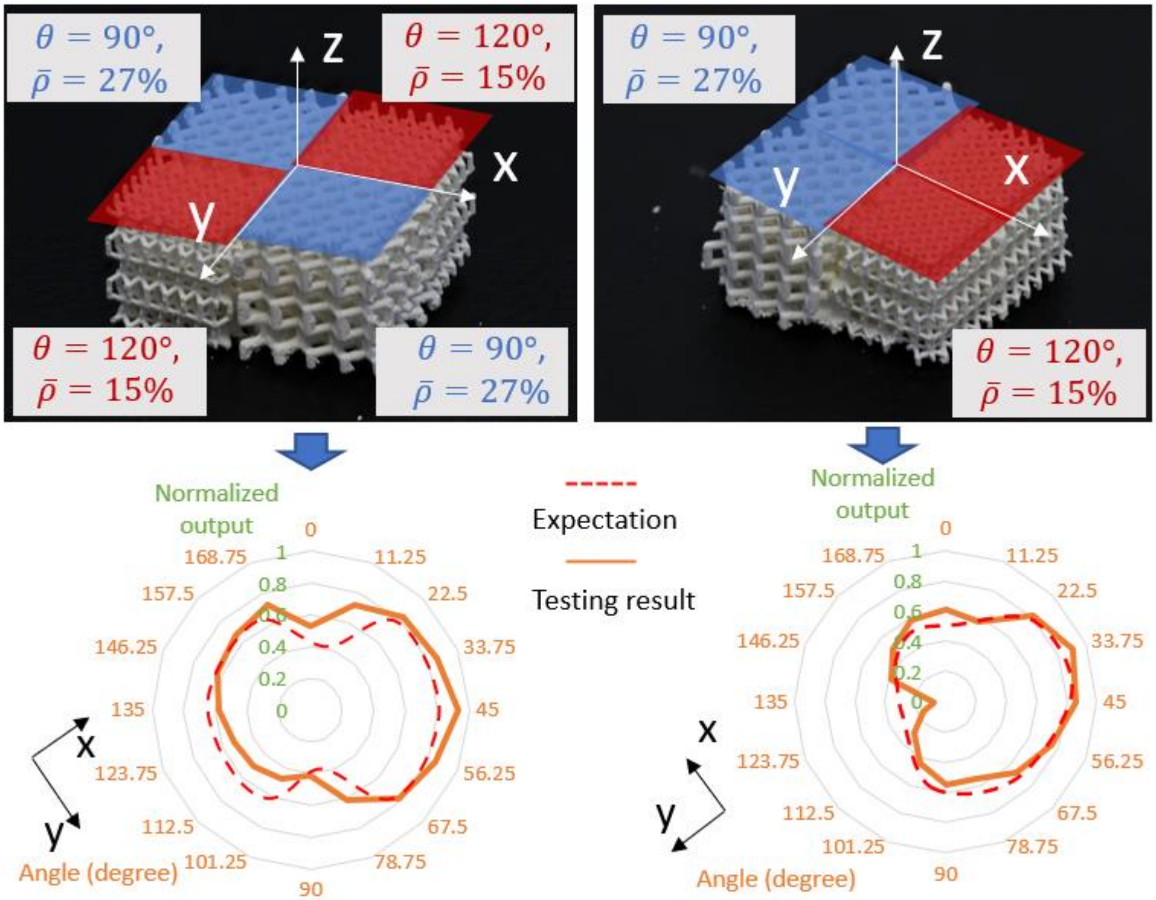

Figure 6-6 Hydrophones with rationally designed 2D directivity patterns and corresponding testing results.

In addition to hydrophones with rationally designed 2D directivity patterns, we can also design and manufacture hydrophones with 3D controllable directivity pattern. Here, we show a spherical micro-architected hydrophone with 3D beam pattern, as shown in Fig. 6-7a. The inset shows the two architectures used in the spherical hydrophone that is only highly sensitive within the center section. Fig. 6-7b shows the schematic of the 3D directivity pattern measuring fixture. The metamaterial hydrophone is suspended in a water tank. A self-developed frame can manipulate the position and direction of the speaker (the same model as the one shown in the previous section) in the water tank so that sound waves can be projected from different directions of the hydrophone. Fig. 6-7c shows the as-measured directivity pattern of the spherical hydrophone. The color of the plot denotes the signal magnitude in dB. Fig. 6-7d-e shows the side view and top view of the 3D directivity pattern.

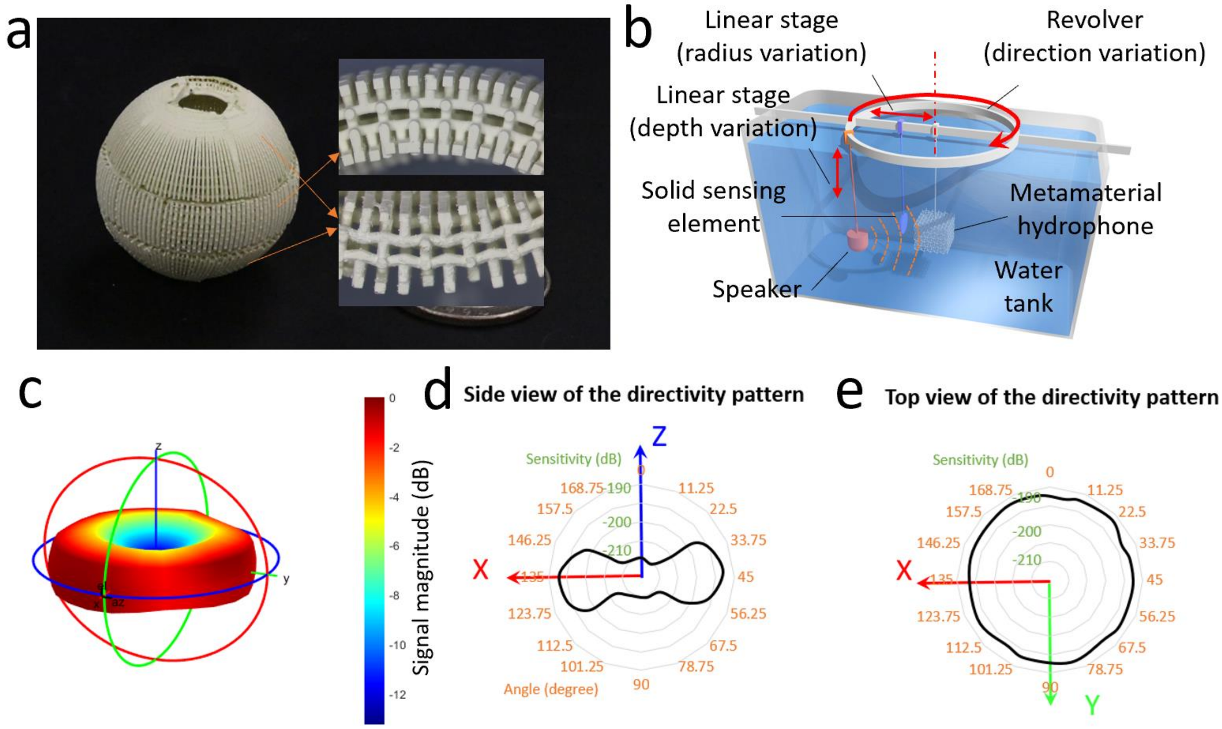

Figure 6-7 (a) Optical image of the spherical micro-architected hydrophone with rationally designed directivity pattern. (b) Schematic of the testing fixture. (c) Directivity pattern of the spherical hydrophone. (d-e) Sideview and top view of the 3D directivity pattern.

With a rationally designed directivity pattern, the spherical hydrophone can eliminate the noise generated by surface reflection during underwater communication, as shown in Fig. 6-8a-b. As a demonstration, we used an impulse signal to test the noise elimination capability of the spherical hydrophone. A commercial hydrophone with a solid PZT sensing element was used as a control sample for comparison. As shown in Fig. 6-8c, the direct transmission signal received by the spherical hydrophone is narrower and contains less noise. The following reflective noise received by the spherical hydrophone is also several times lower than that received by the control sample, indicating that the spherical hydrophone can be employed in underwater communication and will highly reduce the reflective noises.

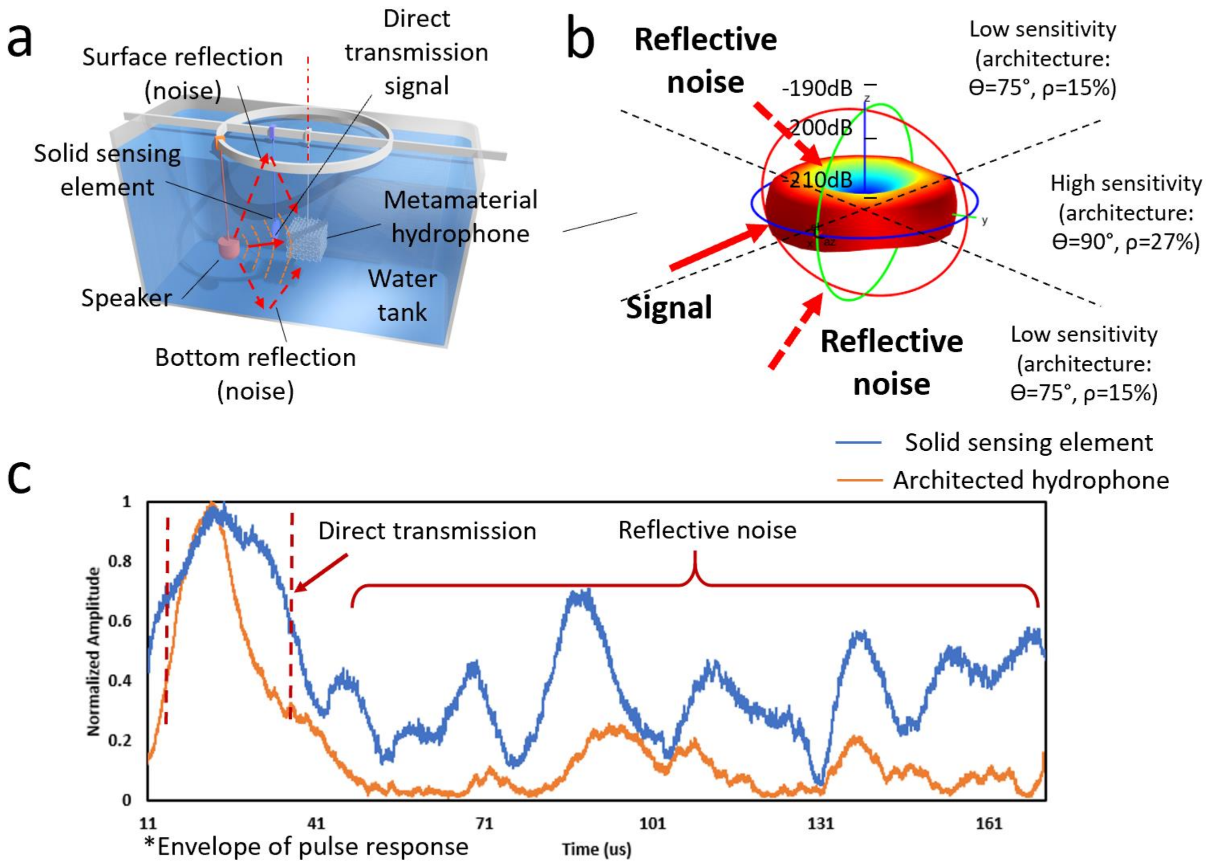

Figure 6-8 (a) Schematic of the testing fixture for underwater communication. (b) Directivity pattern of the spherical hydrophone showing the various sensitivity. (d) The response of the solid sensing element and architected hydrophone to an impulse signal.

6.4 Generation of stretchable ultrasonic arrays for short-range, precise underwater imaging on complex surfaces.

6.4.1 Fabrication and assembly of an ultrasonic array

The optical image of an ultrasonic array consisting of 4 by 4 PZT elements with micropores is shown in Fig. 6-9a (before sintering) and Fig. 6-9b (after sintering). Each element has a 3mm by 3mm cross-section area and a 1mm thickness. As shown in the zoom-in view, there are predesigned micro-pores along the thickness direction of the transducer, which was filled with epoxy to make the sintered element 1-3 composite. Compared to the bulk PZT element, the 1-3 composite has excellent electromechanical coupling coefficients that convert the majority of electrical energy to vibrational energy. Additionally, the epoxy filler suppresses transverse vibrations of the PZT element, allowing enhanced longitudinal waves that go into the target objects. A block of the silver-epoxy composite was bonded to the bottom of the PZT element and serves as a backing layer, which eliminates the ringing effects of the elements, shortening the pulse length and broadening the bandwidth of the transducers (with backing) to provide a better axial resolution.

A large number of transducers require a complex circuit to collect signals. The fabrication of a complex 3D embedded circuit was enabled by our multi-material system. Based on our previous reports of the charge programmed deposition method, the negatively charged polymer was printed in the 3D circuit design, as shown in Fig. 6-9c. The negatively charged polymer is selectively deposited with copper, while the other sections remain undeposited, and serves as leads, as shown in Fig. 6-9d. The charged polymer which has a ~2 megarayleigh (MR) impedance also performs as a matching layer, allowing a gradient when pulse wave transmits from transducer (PZT composite, ~18 MR) to the load (water, ~1.5 MR). The top electrodes are all interconnected and grounded during testing while the 16 bottom electrodes are individually addressable, enabling simultaneous data acquisition from all 16 piezoelectric transducers, as shown in Fig. 6-9e. The rigid transducer was encapsulated in a flexible matrix with embedded 3D circuits. Thus, the ultrasonic array has local rigidity and global flexibility, allowing over 200% strain and accommodation with a diverse class of complex surfaces, as shown in Fig. 6-9f.

6.4.2 Electromechanical characterizations

After assembly, the piezoelectric transducers were poled with an 8V/um electric field under gradient temperatures and the piezoelectric properties were activated upon polarization. Ultrasonic emission and sensing performances are dependent on the conversion between mechanical and electric energy. Thus, the electromechanical coupling factor, k_t, is a key metric to evaluate the ultrasonic transducers. Fig. 6-9g plots the electrical impedance as a function of frequency, from which we can derive the electromechanical coupling factor. The dip and peak shown on the blue curve represent the resonant frequency, f_r, and anti-resonant frequency, f_a, of the as-fabricated piezoelectric transducers. The coupling factor, k_t, can be calculated by[136]

$$k_t = \sqrt{\frac{\pi f_r}{2 f_a} \times cot \frac{\pi f_r}{2 f_a}}$$

The averaged resonant frequency, anti-resonant frequency and coupling factor are 1.56MHz, 1.73MHz and 47%. Fig. 6-9h benchmarks the coupling factor of our transducers with those from the state-of-art 3D printed ultrasonic transducers, indicating that our transducer reaches the same coupling factor while outperforming other transducers over 3 times in terms of piezoelectric charge constant, d_{33}. Fig. 6-9i shows the experimental results of a representative pulse-echo response and its frequency spectrum. The pulse-echo response, with a narrow spatial pulse length (~2.1us), a wide bandwidth (~47%), and a high SNR (-13dB), shows the excellent performance of the ultrasonic transducers induced by the high electromechanical coupling factor and the optimized 3D printing of backing layers and encapsulation. To further validate the reliability of the ultrasonic array, the crosstalk between elements with different spacing was also measured, as shown in Fig. 6-9j. The crosstalk between elements are all lower than -18dB, showing the capability of eliminating interference noise between elements.

6.4.3 Spatial resolution characterization

For the application performance evaluation of an ultrasound imaging system, spatial resolution in both axial and lateral directions are standard metrics[137]. Theoretically, the axial resolution of an array remains constant under fixed resonant frequency and bandwidth. The axial resolution is taking the full width at half maximum of the signal envelope after Hilbert transform. The device geometry, which affects the focal length and aperture size, will determine the lateral resolution. In ultrasonic transducer research, the ratio between the focal length and the aperture size is defined by the f number. Based on the fixed aperture size, we explored the lateral imaging resolution with a series of different f number. The array was bent to different curvatures to image thick metal wire at the focal lengths of 5, 10, 15, 20mm, respectively. The resolution curves spread functions are shown in Fig. 6-9k (average value of all testings). As the dashed lines indicated, the measured axial resolutions at -6 dB were calculated for both directions. The axial resolution, following the expectation, keeps a constant value of 910 um. The relatively precise spatial resolution which is comparable to many previous reports in which implement traditional crafts is due to the precise 3D printing technology.

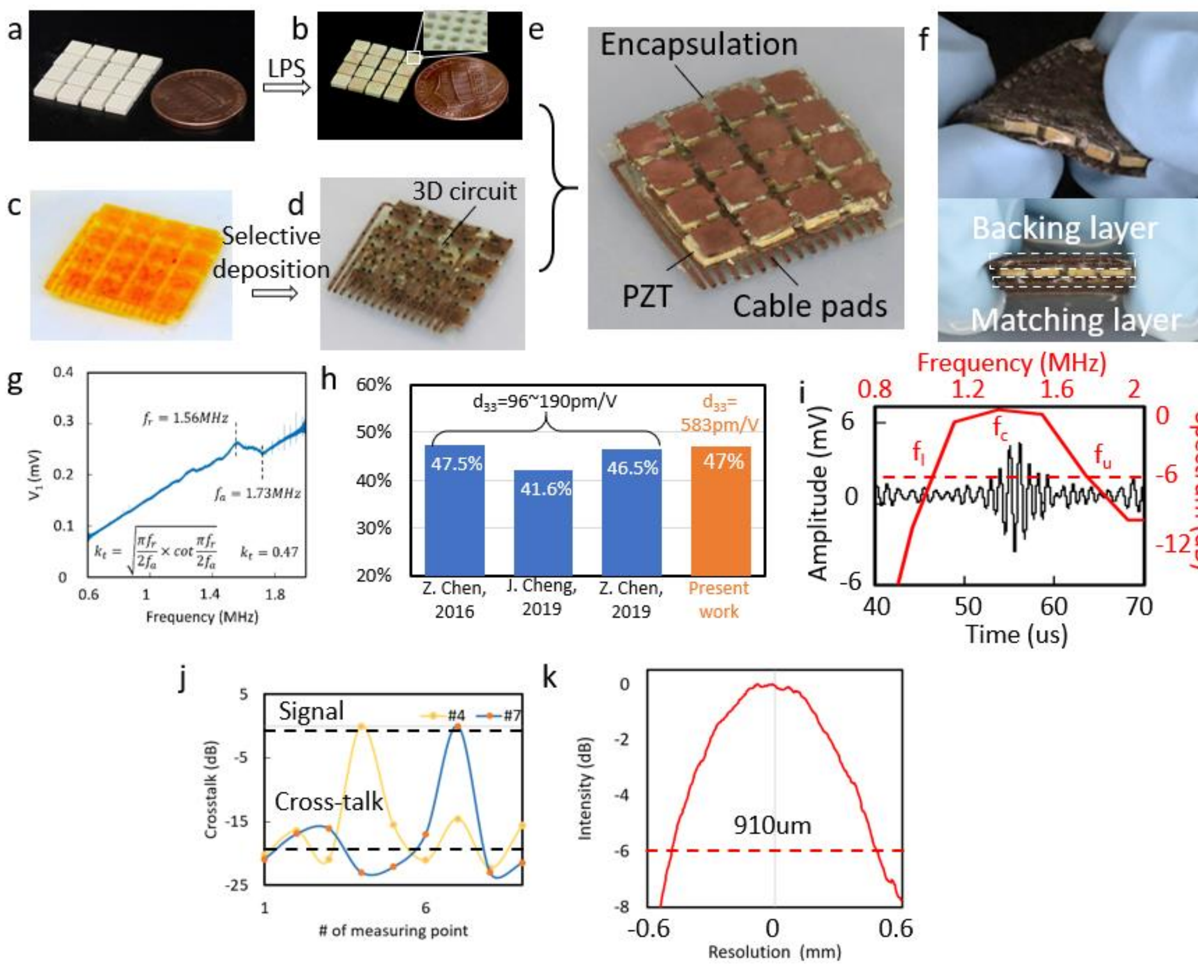

Figure 6-9 a-f) Optical images of the piezoelectric elements, 3D printed circuits and the assembly of the ultrasonic array. g) Measurement of the resonant and anti-resonant frequency. h) Benchmark the d constant and coupling factor with that of the state-of-art 3D printed ultrasonic transducers. i) Bandwidth measurement of the transducer. j) Crosstalk measurement between two elements. k) Resolution measurement based on -6dB threshold.

As a verification of the resolution of the ultrasonic array when employed to perform ultrasonic imaging, a stepped target with 0.5mm to 1mm step height was designed, as shown in Fig. 6-10a. During the testing, the ultrasonic element was moved from one side to the other side of the target while outputting pulse (1.2MHz) and receiving echos, as shown in Fig. 6-10b. Based on the signal received by the ultrasonic element, a B-mode image was generated to reconstruct the shape of the target, as shown in Fig. 6-10c. The result shows that the B-mode image matches well with the target design and the ultrasonic element can distinguish distances as small as 0.5mm.

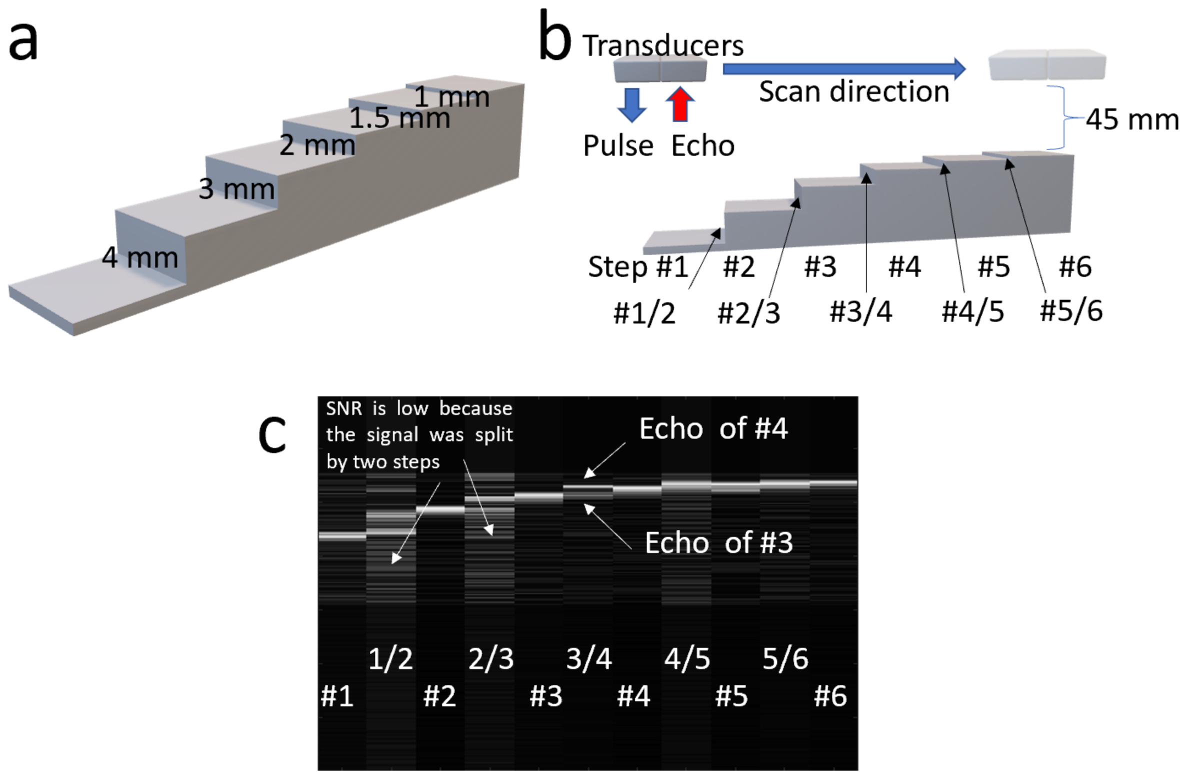

Figure 6-10 (a) Computer aided schematic of the stepped target. (b) Schematic of the resolution test of the ultrasonic element. (c) B-mode image for the stepped target.

6.4.3 Ultrasonic imaging of 3D objects underwater

To test the assembled array's actual performance and evaluate its imaging capability for objects with complex composition, a more complicated target was designed, as shown in Fig. 6-11a. The targeting object contains multiple steps and an angle on its imaged surface. The array was fixed on the side of a water tank and the different positions are labeled, as shown in Fig. 6-11b. The ultrasonic array was put in front of the target and performed the shape instruction, as shown in Fig. 6-11c. When the ultrasonic wave hits the stepped surface, part of the signal echoes back and was received by the ultrasonic array. Every element of the array can capture the echoes from its corresponding part of the object. With the detected echo signal information, we can reconstruct the target 3D image and match the actual structure. By taking the wall where the array was fixed as the x-y plane and using the echo travel distance as the z value, we reconstructed the B-mode image which is shown in Fig 6-11d and the grayscale indicates the signal intensity. All the signal points of the corresponding transducers of the array accurately reconstruct and fit the actual surface, thereby demonstrating the potential capabilities of the array to image objects with complex composition.

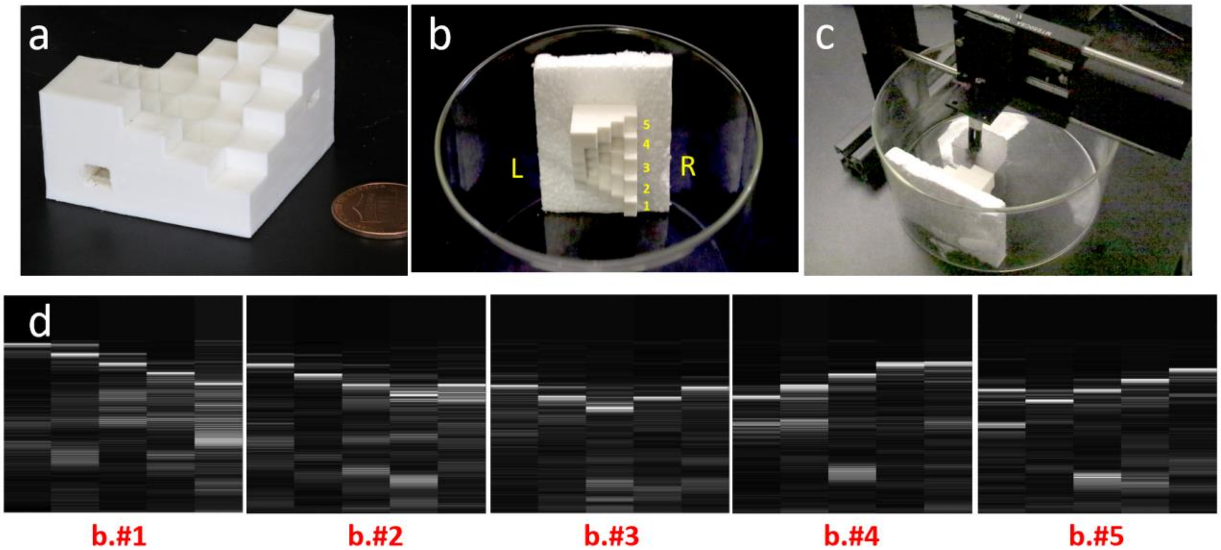

Figure 6-11 (a) 3D-printed object for detection. Complex steps and two internal holes were designed with it to verify array's detection precision. (b) Front view of the object. From the bottom layer to the top layer, the number of the layer was defined in #1 – #5 layer. (c) Underwater scanning experiment set-up. The transducers controlled by motor are scanning the object from right side to left side, and from layer #1 to layer #5. (d) B-mode images for the object. It clearly shows the step arrangement which is precisely in line with the real object surface.

Chapter 7 3D micro-architected piezoelectric metamaterial with rationally designed actuation modes

Piezoelectric ceramic material has been widely implemented in actuation systems due to their stability, high blocking force and precise motion control[52, 53, 138]. Piezoelectric strain coefficient (d_{nm}, n=1-3, m=1-6), defined as the ratio between the strain of piezoelectric material in m direction and the electric field applied along n direction, quantifies the performance of piezoelectric materials when used as actuation elements. However, the crystal structure of conventional piezoelectric materials features a macroscopic transversely isotropic symmetry, leading to only five nonzero piezoelectric strain coefficients, d_{33}, d_{31}, d_{32}, d_{24} and d_{15}[139]. These five coefficients also denote five working modes that can be categorized into normal strain modes (33 mode, 31 mode and 32 mode, Fig. 7-1a) and shear strain modes (24 mode and 15 mode). Although recent studies prompted strategies to obtain arbitrary ratios among coefficients[3] and excite all naturally nonzero coefficients[140], the deformation modes of the piezoelectric materials are still limited to normal strain modes or shear strain modes. To enable more complicated deformation modes, including twisting and bending, transmission mechanisms must be employed. These mechanisms, however, reduce the accuracy, loading capability and energy efficiency of piezoelectric actuation elements[141, 142]. Furthermore, these mechanisms suffer from large-dimension, high weight and low reconfigurability, imposing restrictions on the application of automatic devices and mesoscale robotic systems.

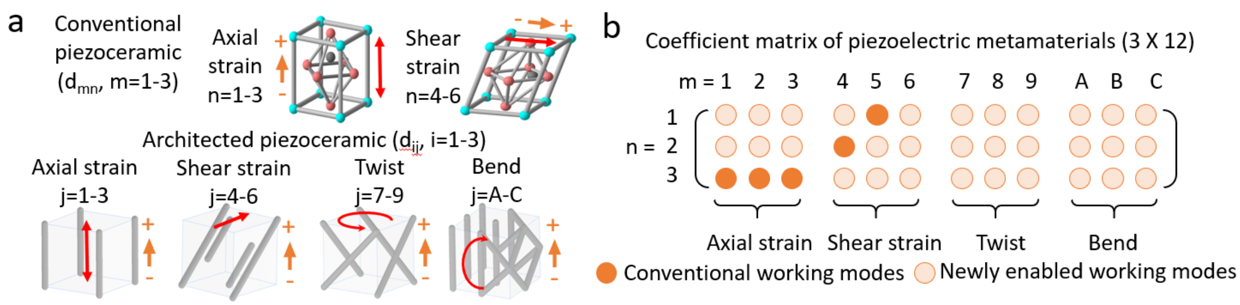

Figure 7-1 (a) Two representative working modes of conventional piezoceramic and newly enabled working modes via designing architected piezoceramics. (b) Extended piezoelectric coefficient matrix.

In this chapter, we demonstrate the design rationale and additive manufacturing of novel kinds of architected piezoelectric metamaterial with previously unattainable performances and deformations modes. With rationally designed micro-architectures, we can not only enhance the strain of conventional working modes by orders of magnitude but also obtain previously unachievable working modes, including twisting and bending (Fig. 7-1a). Our design strategy starts by arranging piezo-active and passive ligaments within a representative volume element (RVE), which is also referred to as the "unit cell" of the metamaterial. A variety of working modes of piezoelectric metamaterials can be achieved via configuring the geometrical parameters, number and spatial orientation of the ligaments to satisfy necessary conditions for each deformation mechanism of the ligament. The unit cells are then tessellated in three dimensions and form metamaterial blocks with different working modes. Since the conventional piezoelectric strain coefficient matrix cannot describe complex working mode, we invoke micropolar mechanics and introduce an extended matrix (Fig. 7-1b) to characterize the twist and bend strain of architected piezoceramics per driving electric field.

The fabrication of these metamaterial designs is enabled by an additive manufacturing technique capable of fabricating both high-performance low porosity piezoceramics with high resolution and passive ceramic frames with selectively deposited 3D circuits. Four representative metamaterial designs with normal strain, shear strain, twisting and bending modes were fabricated and experiments were carried out to verify the deformation modes. The integration of 3D circuits allows localized polarization and electric field of our designs, which enhances the strain of piezoelectric metamaterials and enabled decoupling of conventionally coupled working modes.

As a consequence of our freeform design and fabrication, different types of metamaterials can be modularized and combined into a single-piece material block and construct multiple degrees-of-freedom modular actuation elements. The stackability of the modularized actuation elements allows the generation of complex coupled or decoupled motion without any transmission systems, which increases the energy efficiency of actuation systems generated by the piezoelectric metamaterials. We demonstrate the ease of implementation and utility of the piezoelectric metamaterials in three applications: (i) A high-speed, high-resolution beam steering system consisting of twisting metamaterials. (ii) A precision 6DOF piezoelectric actuation element, which achieves multi degrees of freedom motion on a single piece element within a compact space. (iii) A small scale (<20mm), energy-efficient, high-speed locomotion robot with a self-sensing element and closed-loop control.

7.1 Design strategy of various deformation modes

Our design theory starts with the arrangement of a representative volume element (RVE) with N spatially oriented piezoelectric ligaments, which are further interconnected via in-plane structural frames. Via manipulating the position and orientation of the piezoelectric struts within the given design volume, we can achieve an arbitrary loading-condition combination of the effective force and moment induced by the external electric field. This design freedom further allows us to explore all feasible deformation mechanisms that go beyond the limitation of the conventional piezoelectric actuation elements, which are constrained by the intrinsic crystal structure of the piezoelectric materials. To quantitatively characterize each feasible deformation modes, we expanded the conventional piezoelectric charge constant matrix d_{nm}. Constrained by the deformation of the bulk piezoelectric ceramics, the conventional piezoelectric coefficient matrix only takes into account extension and shearing deformation and cannot quantify twisting and bending modes. Therefore, we invoked the micropolar mechanics and introduced 18 additional terms to expand the coefficient matrix, which could comprehensively characterize all four categories of deformation modes of the RVE. As shown in Fig. 7-1b This expanded d constant matrix can be divided into four sections with m=1-3, m=4-6, m=7-9, m=A-C, which is corresponding to four deformations, respectively, including normal strain, shear strain, twist strain and bending strain. Evaluation of the piezoelectric coefficient matrix enables rational design of the micro-architecture of the piezoelectric unit volume, that achieves arbitrary piezoelectric actuation performances.

As a demonstration, we generated four representative micro-architecture designs with four working modes, 33, 35, 39 and 3A mode, from each section of the extended coefficient matrix. The unit cell designs within RVE are shown in Fig. 7-2a-d. The in-plane ligaments are made from passive structural material while the out-of-plane ligaments consist of piezoelectric ceramic. The unit cell designs are then tessellated in 3D space to form the corresponding architected piezoelectric metamaterial blocks, as shown in Fig. 7-2e-h.

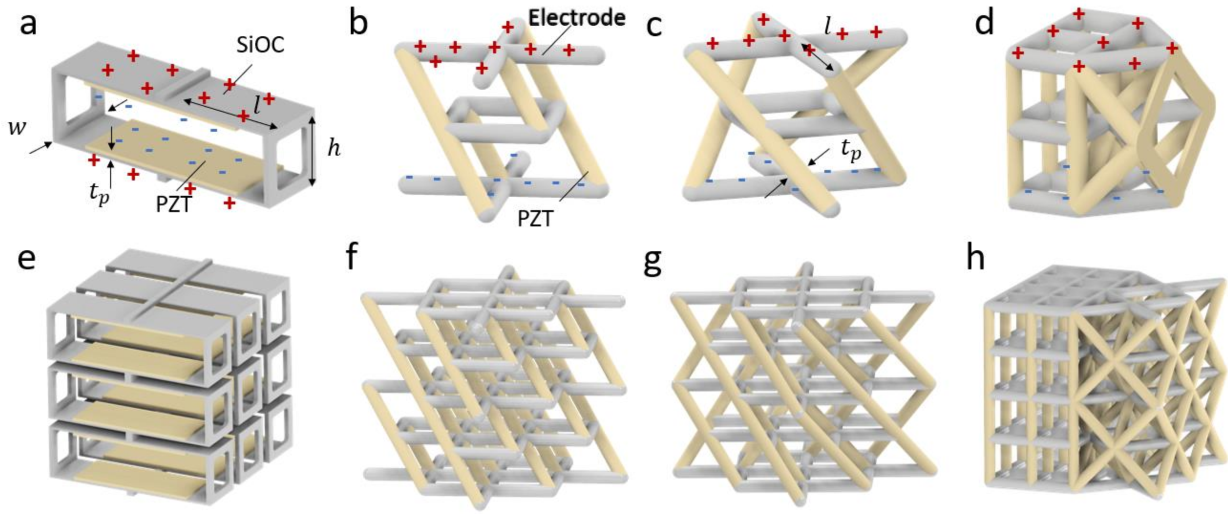

Figure 7-2 (a-d) Schematic of the unit cell designs allowing axial strain magnification, shearing, twisting and bending working mode. (e-h) Schematic of an architected piezo material block generated by tessellation of unit cells in a three-dimensional space.

7.2 From piezoelectric composites to piezoceramics

The fabrication of four representative architected piezoelectric metamaterials is enabled by a multi-material additive manufacturing system (Fig. 7-3a) capable of printing both highly loaded (up to 50vol% particle) piezo particle composites with high resolution (50um) and passive ceramic frames that can be selectively deposited with 3D circuits. During the fabrication, PZT particles (APC 855) and a liquid phase sintering agent, $Pb(NO_3)_2$ are dispersed with ultraviolet-sensitive monomers into highly concentrated (50vol% particle loading) uniform colloids and then sculptured into 3D structures by near-ultraviolet light in a layer-by-layer manner. The as-printed piezoelectric composites are then sintered in the air to generate dense PZT ceramics. During the sintering process, the photosensitive monomer is burnt out and the lead nitrate salt melts. The PZT particles contract to form a denser part due to the surface tension of the melted lead nitrate, as shown in Fig. 7-3b. Additionally, lead nitrate also compounds and generate lead oxide and creates a lead-rich environment at high temperature (>850C), which prevents performance reduction due to lead evaporation. Fig. 7-3c-f shows some as-fabricated representative structures with feature sizes down to 10um and highly dense cross-section with only 3% porosity. After sintering, the piezo part was poled under 8V/um electric field with an optimized temperature profile. The as-fabricated piezoceramic yields a piezoelectric coefficient that is close to bulk ceramic and outperforms the state-of-art 3D printed piezoelectric composites or ceramics, as shown in Fig. 7-3g.

The passive structural frame was fabricated with a polymer-derived ceramic, silicon oxycarbide, (SiOC), printed together with a charged pre-ceramic monomer, as shown in Fig. 7-3h. The multi-material green part was then dipped into charged solutions and selectively deposited with electroless metal to form a 3D circuit (Fig. 7-3i). The deposited conductive material was then co-sintered with SiOC under argon environment (Fig. 7-3j). The resulting passive structural material has both high stiffness and 3D circuit, which enables the localized electrode.

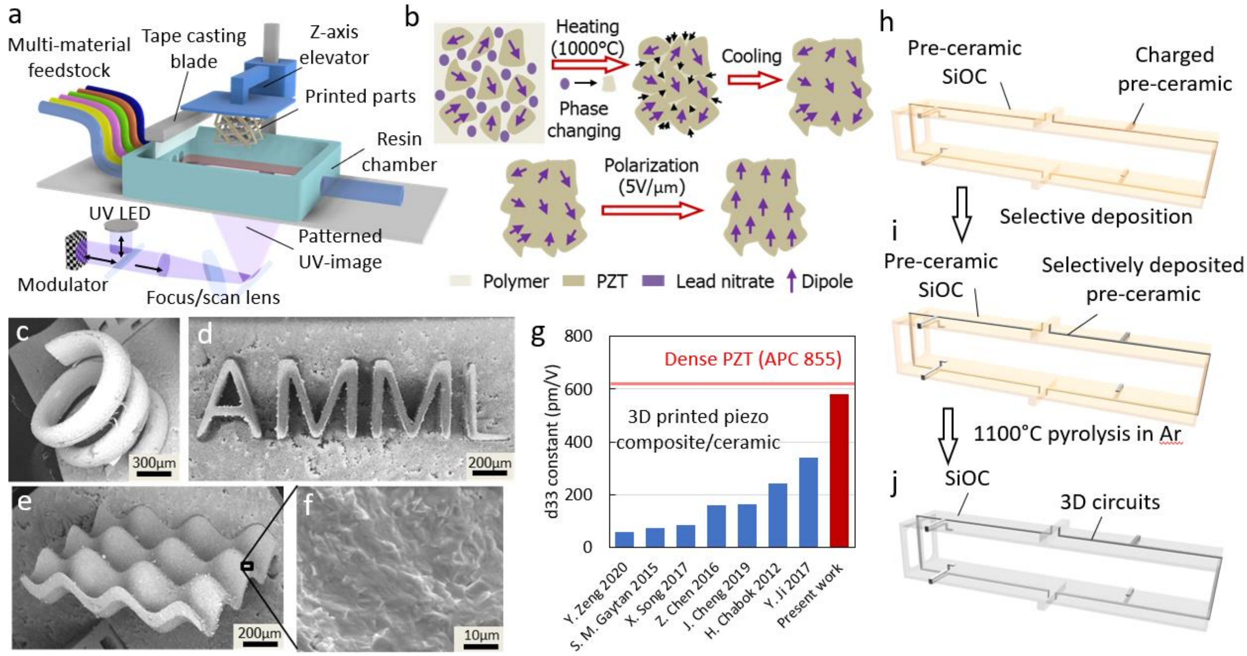

Figure 7-3 Additive manufacturing and post-processing of piezoelectric ceramic with ultralow porosity and passive materials with 3D circuits. a) Schematic illustration of the high-resolution multi-material additive manufacturing system capable of printing highly loaded piezoelectric composites and multi-material pre-ceramic polymers. b) Schematic illustration of liquid phase sintering and polarization process. c-f) Scanning electron microscope images of 3D-printed piezoelectric geometries and zoom-in image of the as-fabricated PZT structures. g) Comparison of piezoelectric charge coefficients and fabrication resolution between the additive manufactured piezoceramics presented in this study and the state-of-art 3D printed piezo materials. h-j) Schematic illustration of the selective deposition and pyrolysis process of the multi-material pre-ceramic polymer structures.

7.3 Verification of rationally designed deformation modes

To experimentally verify the working modes of the piezoelectric metamaterials, we 3D printed four piezoelectric lattices that work under expansion (d_{33}), bending, shearing and twisting mode with an applied electric field (Fig. 7-4a-d). Fig. 7-4e presents the displacement output of solid PZT materials (blue curve) and material with strain magnification architectures (red curve) with the d33 working mode under increasing driving voltages. We found the effective d33 constant of architected piezoelectric material can reach 10050pm/V, which is over 17 times higher than its constituent material having a 583pm/V d33 coefficient. We verified the other three working modes by capturing the deformation of the side surfaces of the lattices. During the testing, the deformation of the side surface induced by a voltage input was captured with a high-precision full filed laser vibrometer and then recorded by a data acquisition system. The side surface deforms in different ways due to the nature of the corresponding deformations and the color maps in Fig. 7-4f-h capture the normalized deformation of the side surface when the input voltage reaches the peak value. Through comparing the surface deformation of the as-fabricated lattices with that of the solid beams under corresponding deformation modes, we confirmed that four lattices all showed the designed working modes.

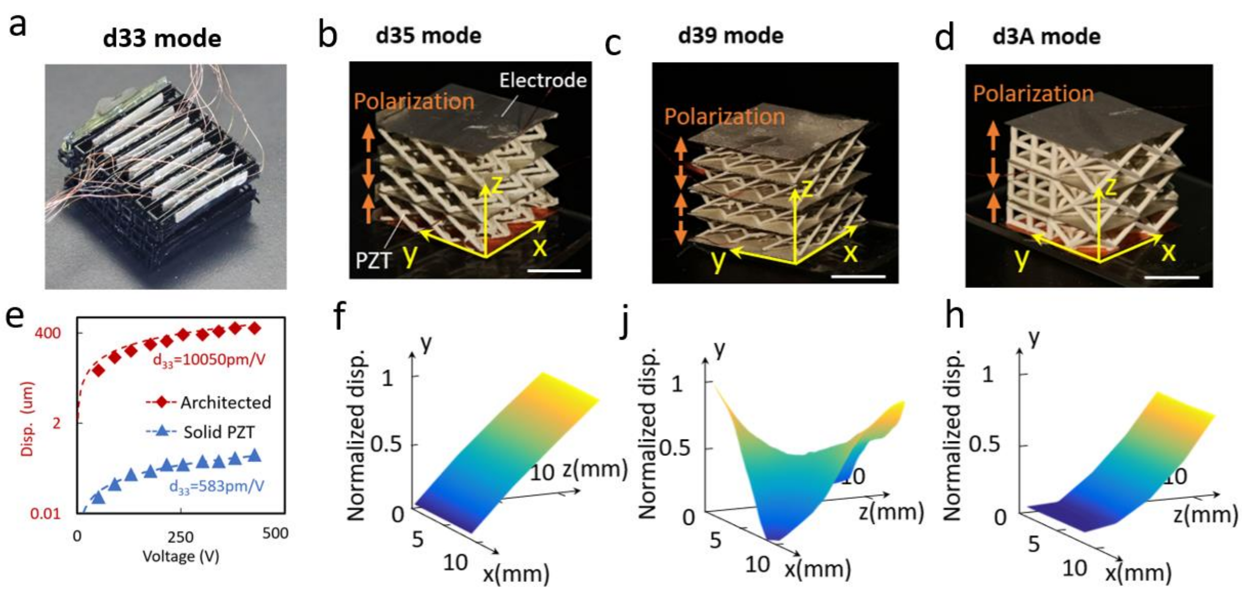

Figure 7-4 a-d) Optical image of additive manufactured architected piezo materials. e) Displacement of the solid PZT ligament and d33 mode metamaterial as a function of applied electric field. The displacement generated by the d33 mode metamaterial achieves 621um with a 3.3V/um electric field, demonstrating a ~18 times higher d33 constant compared to solid PZT element. f-h) The deformation of the side surface (x-z plane) of the as-fabricated metamaterials with shear, twisting and bending mode.

7.4 Localized electric field and deformation enabled by localized electrode

Our programmable multi-material manufacturing platform makes it possible to seamlessly integrate piezo-active and conducting phase in 3D architectures, which can be applied to our metamaterial designs and enhance their performances.

Due to the discontinuity of the active material in the d33 actuation architecture, each active PZT element requires two leads, which increases the weight of the actuator and limits the deformation of the actuator. By adding 3D programmed electrodes, all elements can be interconnected and only two leads are required for the whole actuator, which highly reduced the complexity of the wiring, as shown in Fig. 7-5a. Additionally, the localized electrode induces a higher electric field with the same driving voltage compared to conventional electrode configuration (external electrodes, Fig. 7-5b), thus enlarges the piezo deformation. Fig. 7-5c-d shows a representative unit cell with localized electrodes. The electric field applied to the active material changes from V/h to V/t when the electrode configuration changes from external electrode to localized electrode, where V is the driving voltage, h is the height of the unit cell, t is the thickness of the piezo ligaments and $h >> t$.

Here, we use the shearing and twisting lattice (Fig. 7-5e&h) as two representative cases and demonstrate the improvement of corresponding piezoelectric coefficients by localized electrodes. Fig. 7-5f-i shows that the twisting angle and shear displacement are improved by over 10 times compared to the conventional electroding method, indicating a 10 times improvement in effective piezoelectric shearing and twisting coefficient enabled by the localized electrode. Furthermore, the localized electrode enables the decoupling between different modes. For conventional piezoelectric materials, actuation modes d_{31}, d_{32} and d_{33} are coupled with a voltage applied along 3-direction. We show the localized polarization allows decoupling of different modes. Fig. 7-5g&j plots the twisting angle and shearing displacement as a function of time of lattices with and without localized polarization. Without localized polarization, the expansion mode is coupled with the other two modes. With localized polarization, the expansion mode is decoupled with the shearing and twisting mode, which is not achievable for conventional piezoelectric materials.

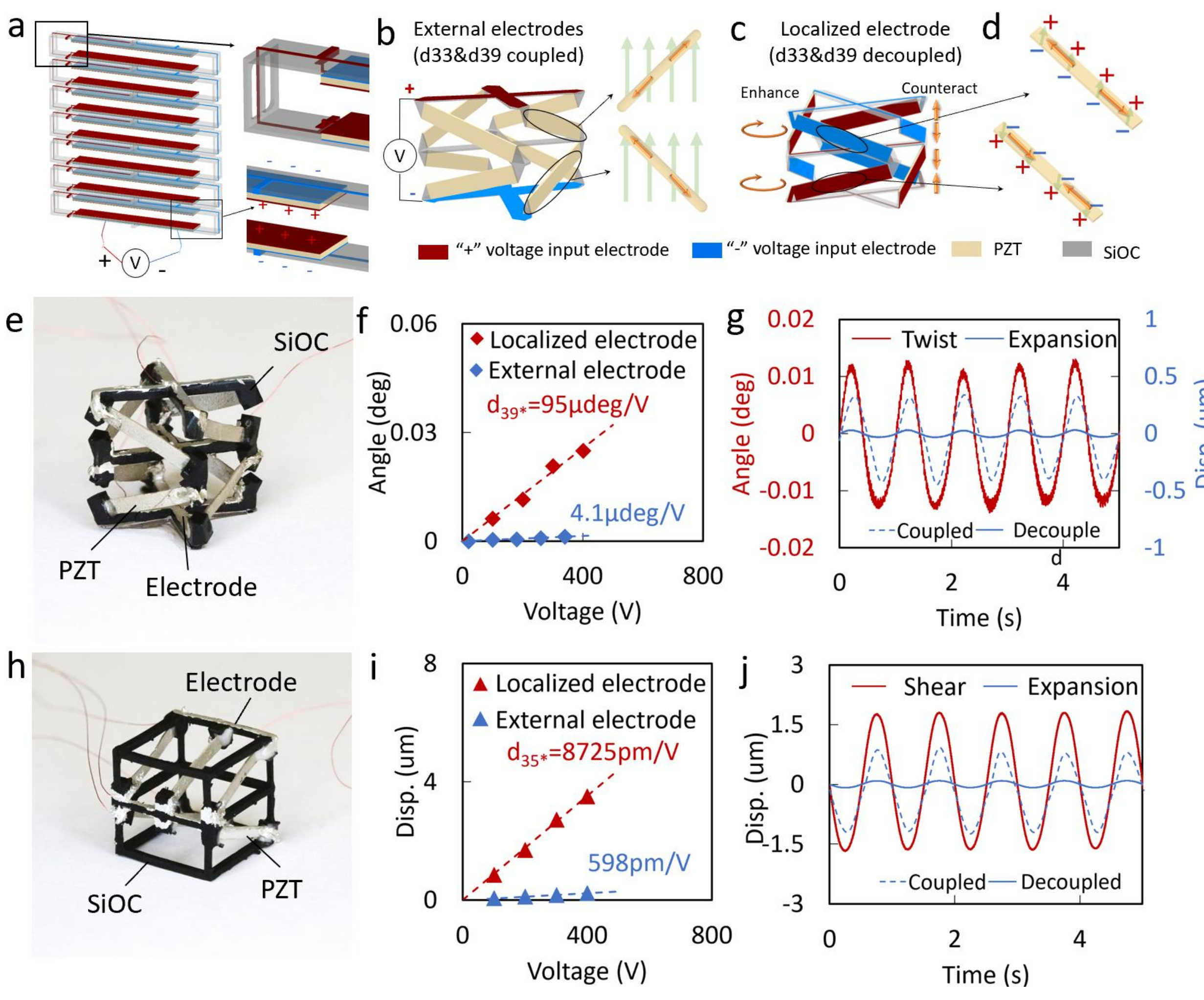

Figure 7-5 Piezoelectric metamaterials with localized electrode and decoupled working modes. a) Schematic illustration of the d33 mode strain magnification metamaterial with localized

electrode. The localized electrode interconnects the discrete piezo ligaments, leading to only one voltage input regardless of unit cell numbers. b) Schematic illustration of metamaterial design with external electrodes. c-d) Schematic illustration of metamaterial design with localized electrode. By rationally switching the directionality of polarization and electric field, d33 and d39 mode can be decoupled. e) Optical image of the as-fabricated piezoelectric twisting metamaterial with localized electrode. f) Twisting angle of the metamaterials with an external electrode and localized electrode as a function of input voltage. g) Twisting angle and expansion of metamaterial with coupled and decoupled working with a 500V p-p 1Hz sinusoidal voltage input. h) Optical image of the as-fabricated piezoelectric shearing metamaterial with localized electrode. i) Shear displacement of the metamaterials with external electrode and localized electrode as a function of the input voltage. j) Shear displacement of metamaterial with coupled and decoupled working with a 500V p-p 1Hz sinusoidal voltage input.

7.5 Modular actuation elements consisting of piezoelectric metamaterials

The modular nature of these piezoelectric metamaterials allows them to be composed in various arrangements to achieve arbitrarily complex actuation modes. A single actuation element consisting of different metamaterial designs can obtain a variety of different motion and multiple degrees of freedom depending on working conditions. Herein, we applied the modular actuation elements consisting of piezoelectric metamaterials to both a beam steering system and a multiple-degrees-of-freedom nanomanipulator.

We developed a light-weight beam steering system that achieves high-precision high-speed control of the laser spot. Fig. 7-6a-b shows the actuation element composed of the piezoelectric twisting metamaterial and the set-up of the beam steering system, respectively. A laser source shoots a laser beam onto the actuation elements and the laser is reflected to a laser sensor with a 15mm diameter. The motion of the reflected laser spot can be captured by the sensor. To demonstrate the high precision of the beam steering system, the laser sensor was put four meters away from the actuation elements. The tilting angle of the mirrors is controlled by the voltage applied to the actuation element and the mirrors turn to the original position when the field is removed. Since the displacement of the laser spot is negligible compared to the distance between the actuation elements and the laser sensor, the displacement of the laser spot can be linearly related to the twisting angle. The tilting angle of the two mirrors controls the displacement of the laser spots in two directions, respectively. To demonstrate the repeatability and precision of the beam steering system, we draw a square shape laser trajectory for 10cycles at 20Hz, as shown in Fig. 7-6c. The results show the RMS precision of the square shape is 50um±11um, showing the accurate control of the tilting angle of the reflective mirrors.

We combined our piezoelectric metamaterials with multiple working modes and designed a piezoelectric actuation element (PAE) capable of 6-degrees-of-freedom motion, as shown in Fig. 7-6d. The device was printed with embedded electrodes and each layer of the PAE can be activated individually. To verify the performance of the 6DOF PAE, the deformation of the side surface of the PAE was captured. Fig. 7-6e plots three representative working modes of the 6-DOF PAE when bending, twisting and shearing lattice was actuated individually. The step resolution of the nano manipulator under varying voltage amplitudes was evaluated with shearing as a representative mode by a laser displacement sensor. The stepwise excitation signal magnitude and corresponding displacement generated are presented in Fig. 7-6f. The minimum displacement of 1.5nm was found under the voltage change of 8V. The ultrahigh resolution of the nano manipulator should be attributed to the non-resonant working mechanism of the nanomanipulator. Implementation of high accuracy positioning at the scale of nanometer brings lots of benefits to future MEMS and NEMS field. Our PAE consisting of piezoelectric metamaterials is the most compact design compared to the conventional configurations of piezoelectric actuators for nanomanipulation, as shown in Fig. 7-6g.

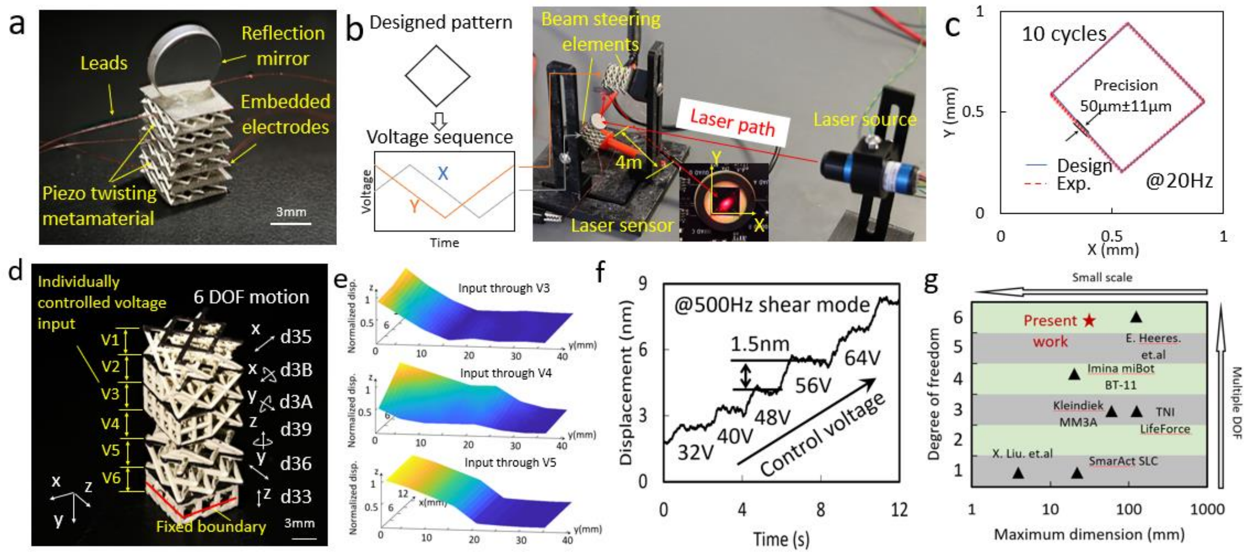

Figure 7-6 Modular actuation elements consisting of stackable mode switching piezoelectric metamaterials**.** a) Optical image of the piezo twisting metamaterial with embedded electrodes and reflection mirror. b) Set-up of the beam-steering system. The voltage sequence is generated based on the designed laser spot pattern and applied to the twisting elements. c) Designed and experimental laser spot trajectories for a square pattern executed at 20Hz. d) Optical image of a modular 6-DOF PAE consisting of six layers of piezo metamaterial blocks with different working modes. Each layer of the PAE can be individually controlled through the corresponding voltage input. e) The deformation of the side surface (y-z plane) of the 6DOF PAE with three representative working modes (d3A, d39 and d36). f) A representative displacement resolution plot of the 6DOF PAE under shear mode and 500Hz voltage input. g) Comparison between the 6DOF PAE enabled by architected piezoelectric metamaterials and conventional multi-degree-of-freedom manipulators.

7.6 Energy efficient locomotion robot with multiple walking modes

To enable locomotion, the displacement of the actuation elements needs to be leveraged. Conventional methods rely on flextensional joints and levers to increase the displacement output and thus enable locomotion. However, the energy efficiency of the whole robotic system is highly reduced due to the leverage mechanism. Utilizing the piezoelectric architectures, we can combine multiple actuation elements into one actuator with outputs in multiple directions. Therefore, there is no transmission needed in our robotic system, which highly increased the efficiency of the robotic system and reduces the cost of transport. As a demonstration, we used three 33 mode actuation elements to develop a locomotion robot. The actuators were rationally located to obtain strain in the directions required to produce locomotion. Two actuators were located vertically in the rear and front of the robot and a central actuator was placed diagonally, as shown in Fig. 7-7a. Four legs, two in each front and rear actuator are the interfaces between the robot and the ground. The legs are designed to produce anisotropic friction when the actuator is activated. As a result, the robot can work under different modes depending on the actuation sequence of three actuators. Each actuator is activated via an independent PWM signal with variable frequency and duty cycle, and amplitude of 500V. The activation of the legs following pre-determined sequences and PWM modulation allows for different locomotion modes. Fig. 7-7b&c shows the driving voltage and working principle of the locomotion robot under walk mode and jump mode. Each mode only has two levels of voltage inputs corresponding to the two statuses of the robot. When functioning in walk mode, the body actuator and rear leg expands with a 500V input and pushes the robot forward. When the driving voltage is removed, the body actuator and rear leg contracts and the anisotropic frictional feet prevent the robot from moving backward. These two processes repeat to move the robot forward. When the robot works in jump mode, an impulse driving voltage with 500V amplitude is first applied to the front leg and kicks the robot off the ground. Before the front leg touches the ground again, the body actuator and rear leg are actuated with an impulse voltage and the robot jumps forward. Utilizing jump mode, the robot can jump over barriers with large height, as shown in Fig. 7-7c, which is not achievable for many other piezo robots having micrometer range deformations.

We then characterized the frequency and payload dependency of the locomotion speed with walk mode. Before testing, a small basket (1.1g) was put onto the robot so that various weights can be steadily loaded on the robot. Fig. 7-7d shows the speed of the robot as a function of the driving voltage. With 220Hz driving voltage, the speed of the robot was maximized and reaches 110mm/s (4.4 body length/s). The high driving frequency is a result of the elimination of transmission systems and low system compliance. Also, at frequencies higher than 260Hz, the actuator body reaches a mode where the body actuator bends during actuation-deactuation phases, producing turning motion. Fig. 7-7e shows the speed of the robot as a function of the payload. With 13g load (13 times robot weight) the speed is only reduced by half. The high payload of the robot is a result of the high blocking force of the actuation element. Due to the modularized design and elimination of transmission mechanisms, our robot is one of the lightest and most energy-efficient among the state-of-art locomotion robots, as shown in Fig. 7-7f.

In the literature, we can find many cm-scale robotic crawlers using different types of actuation elements including shape memory alloy [143, 144], pneumatic [145, 146], dielectric electro active polymers (EAP), and thermally actuated morphs. However, piezoelectric materials have a comparative advantage compared to the mentioned actuation systems. They can transfer electric energy to mechanical energy and also perform the inverse transformation. Thus, the actuation elements can also be used as a sensing element which enables mimicking the proprioceptive feedback in animals and provides robots with an element to interact with the environment. Generally, robots aiming for environmental interaction such as the prototype in [147], require additional sensing elements and the integration with the actuation mechanism increases the complexity of the system. Here, we embedded a self-sensing element to the rear leg of the robot and set up a closed-loop control system in Simulink Real Time. We attached the basket on top of the rear leg, such that when a load is applied to the basket, the piezo ligament under the basket would deform producing a voltage in response. Since all actuation elements are interconnected, their deformations are mechanically coupled and the sensing element also responds to the actuation of the central actuator. As a result, the robot sensing ligament can monitor the gait in real time. We perform experiments trying to mimic basic survival instincts of the insects. We programmed the robot to change working mode after it encounters a stimulus. The stimulus used is a drop weight load applied on the basket. The robot begins at cruise mode (slow speed) would be triggered to 'run away' (increase speed) once the load is applied. The sensing signal during the 'run away' experiments can be seen in Fig. 7-7g. During the cruise mode, the signal shows how the gait of the robot was monitored. Once the load fell, the sensing element produced a strain in the sensing ligament producing a spike in the sensor output. When the amplitude of the spike is higher than an assigned threshold (-0.4V in this case), the system would be triggered to change the working mode (stop, speed up or turn). The sensing capabilities under the external stimulus and gait monitoring are excellent features for robots since it can help to better interact with the environment and to have an observer when visibility is not possible.

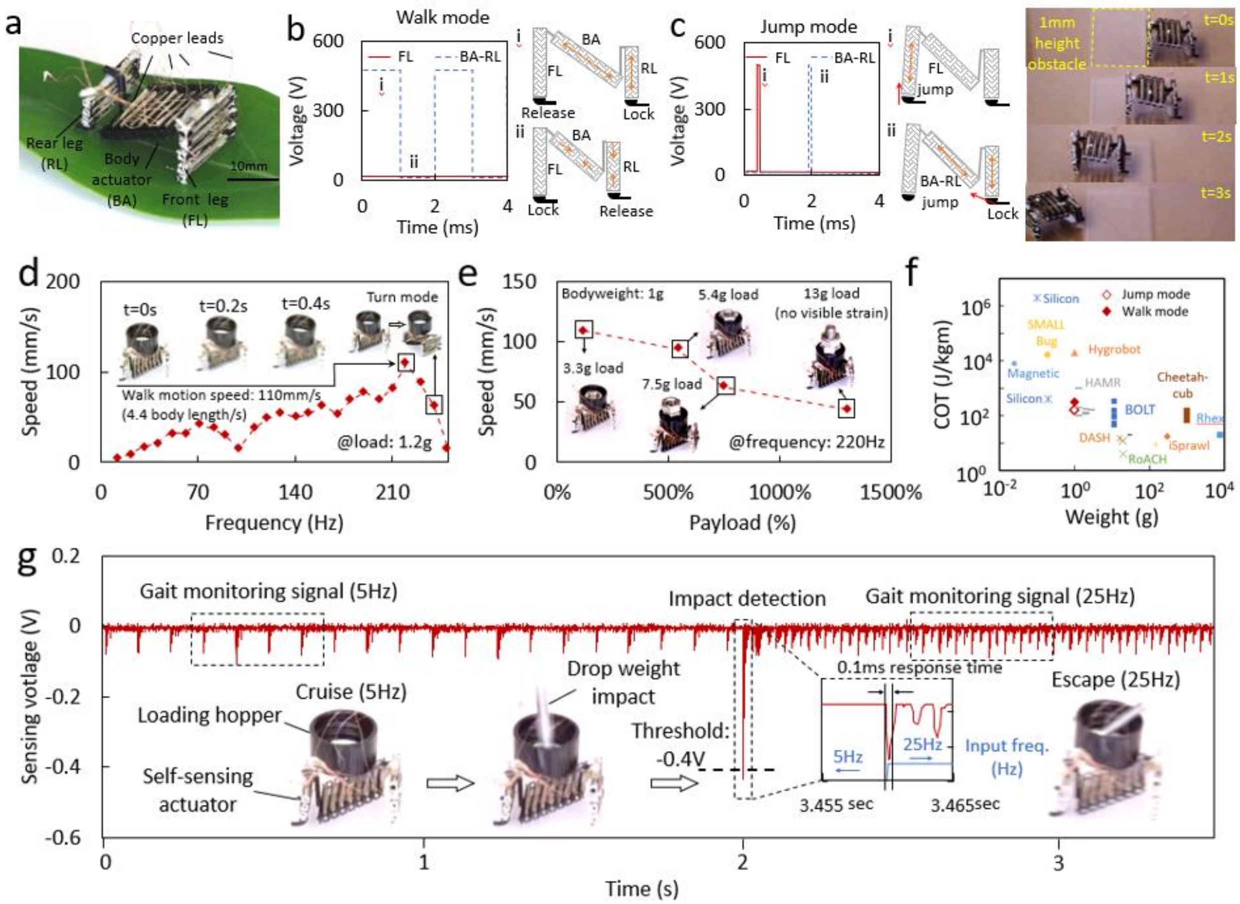

Figure 7-7 High-speed, high payload, self-sensing locomotion millirobot with modular actuation and sensing metamaterials. a) Optical image of the locomotion robot. b-c) Driving voltage and working principle of the locomotion robot under walk mode and jump mode. d) Walk motion speed of the locomotion robot as a function of driving frequency. The mass of the loading hopper is 1.2g. The highest speed is 110mm/s with 220Hz driving frequency. e) Walk motion speed of the locomotion robot as a function of payload. The robot can sustain 13 times body weight with only 50% reduction on walk speed. f) Logarithmic plot of minimum cost of transport vs. mass. The present locomotion robot has a minimum cost of 150J/m/kg and is plotted among data collected from different types of locomotion systems. g) Sensing voltage of the self-sensing actuator. A drop weight impact was applied on the robot and the control voltage frequency of the robot is increased to speed up the robot and escape from the impact area.

Chapter 8 Conclusion

8.1 Answering the research questions

RQ 1 How to enable large area AM with multi-scale features?

A large-area high-resolution projection micro-stereolithography system, capable of printing complex 3D topologies, sub-10μm features and large-volume architectures, was developed. Two scanning mirrors were integrated with a base-line micro-projection stereolithography system to enlarge the printing area while keeping high resolution. Furthermore, the system was upgraded to enable continuous exposure, which synchronized the scanning mirror motion and the UV exposure. The printing speed was increased by 5 times compared to discrete exposure and outperforms the state-of-art method by ~50%. The system allows the fabrication of macro-scale architected materials with micro-scale feature sizes, which will find use in a broad array of applications.

RQ 2 How 3D topology, feature size and scalability impart structural properties?

The LAPμSL system is capable of fabricating multi-scale features, allowing us to reach size effect regime of polymer-derived ceramics and investigate previously unmeasurable metamaterial properties. In this study, the size-dependent mechanical properties of 3D architected ceramic metamaterials and the fracture toughness behavior of micro-architected metamaterials was investigated. I found that these high-temperature architected ceramics of identical 3D topologies exhibit size-dependent strength influenced by both strut diameter and strut length. Weibull theory is utilized to map this dependency with varying single strut volumes. These observations demonstrate the structural benefits of increasing feature resolution in additive manufacturing of ceramic materials. Additionally, the LAPμSL system is capable of fabricating metamaterials containing millions of unit cells, providing a unique experimental platform to study the fracture and damage tolerance of metamaterials. I additive manufactured stretch-dominated architected metamaterials with pre-defined embedded crack, where the size of the unit cells becomes sufficiently small compared to the flaw dimensions. I elucidated the emergence of fracture toughness as a material property in architected metamaterials, which is found to be a property largely influenced by the elastic instabilities of struts members and T-stress. A design map based on a 2-parameter fracture model was developed to guide the design of failure modes in micro-architected metamaterials.

RQ 3 How to develop new AM process to create multi-functional materials with embedded electronics?

Using piezoelectric material as an example, I showed the high-resolution fabrication and functionalization of piezoelectric composite materials with ultra-high particle loading (50vol%). Novel projection stereolithography was integrated with a casting blade to uniformly recoat the highly viscous piezoelectric colloids and ensure high-resolution printing. The piezoelectric particles were functionalized to create covalent bonds between the particle surface and the photosensitive polymer matrix. After being constructed to solid parts with micro-architectures, the electromechanical coupling effect was activated with a novel polarization method designed for piezocomposites and lattices. The as-fabricated piezoelectric composites show the highest piezoelectric charge constant among all state-of-art 3D printed composite materials. Additionally, the functionalization and additive manufacturing technique demonstrated in this study is not limited to piezoelectric particles. It can also be applied to a wide range of functional materials, including piezomagnetic, dielectric and electrostrictive materials.

RQ 4 What are the new opportunities enabled by 3D printed multi-functional materials?

This study paves the way for next generation of smart infrastructures, multi-functional sensors and modular actuators. Specifically, I demonstrated a class of rationally designed electromechanical coupling materials, architected hydrophones with controlled directivity patterns and piezoelectric actuation materials with previously unattainable working modes. The functionality of architected metamaterials is extended from only mechanical or structural properties to electromechanical coupling properties. By applying the novel AM technique to other functional materials, we can also enable other types of functionalities, including electro-magnetic, electro-strictive coupling behaviors. These functional materials can be widely applied to pressure sensing, ultrasonic sensing, displacement sensing, actuation and energy harvesting.

8.2 Contributions and intellectual merit

(1) Established an additive manufacturing platform allowing the creation of architected metamaterials with complex 3D topologies, micro-scale features and large building volumes. The platform can be applied to different UV sensitive materials, including high stiffness polymers, ultra-flexible elastomers and polymer-derived ceramics, making it possible to investigate the process-property-structure relationships of a broad array of metamaterials.

(2) Investigated the size-dependent properties of architected high-temperature ceramics via the LAPμSL system. Utilized Weibull theory to map the size-dependent strength with varying single

strut volumes and provided the first experimental verification. Demonstrated the structural benefits of increasing feature resolution in additive manufacturing of ceramic materials.

(3) Experimentally demonstrated the emergence of fracture toughness as a material property in architected metamaterials. Such investigation is made possible, for the first time, by the large area projection micro-stereolithography developed in this dissertation. Samples with more than 1 million unit cells with embedded penny-shaped cracks, through cracks as well as surface cracks spanning a large number of unit cells allows access to previously unachievable fracture toughness measurement. As a result, we found that fracture toughness in micro-architected metamaterials, is ultimately influenced by the elastic instabilities of struts members and T-stress.

(4) Established an additive manufacturing platform for multi-functional materials. Current additive manufacturing platforms are capable of producing structural materials, including polymer, metals and ceramics. It remains elusive for electronic and multi-functional materials due to the significant trade-off between processability and functional properties. In this research, I developed a high-resolution AM platform capable of processing highly viscous monomers with active-material inclusions over 50vol%. I investigated and optimized the UV curing, polymerization depth, resolutions as well as liquid phase sintering that allows the attainment of high piezoelectric coefficients (over 500pm/V). I also developed an integrated poling process that activates the piezoelectricity of the as-printed samples. The resulting printed piezoelectric achieves tunable stiffness, free-form architectures, high coupling coefficients, tunable dielectric permittivity, and frequency range, paving the way for a myriad of new opportunities for free-form sensors, transducers and robotic actuation.

(5) Developed processing routes that enable integration of the piezoelectrics with electrodes, structural materials and materials with impedance matching for highly sensitive transducers. These transducers were characterized and achieved directional voltage responses prescribed by the designed 3D micro-architectures. I have implemented the 3D electro-mechanical metamaterials as intelligent materials for self-sensing (force magnitude and directionality), directional sound transmission and receiving (beam patterns).

(6) Created a novel class of piezoelectric actuation metamaterials with ultra-high d constant (d_{eff}>10000pm/V) and previously unachievable working modes, including shearing, bending and twisting. The modular nature of these piezoelectric metamaterials allows them to be composed in various arrangements to achieve arbitrarily complex actuation modes. A single actuation element consisting of different metamaterial designs can obtain a variety of different motion and multiple degrees of freedom depending on working conditions. I have implemented the modular elements as actuators for lightweight compact and high-performance automation systems, including high-speed high-resolution beam steering systems, multi degrees-of-freedom nanomanipulation systems and locomotion robotic systems. Moreover, compared to conventional automation systems relying on transmission systems to achieve complex motions, these systems benefit from the micro-architecture designs and can perform complicated operations without transmissions, resulting in increased energy efficiency and low cost of transport.

8.3 Recommendations for Future Work

(1) Machine vision in-situ monitoring of projection pattern during the continuous scanning process. In this study, we demonstrated that the continuous scanning and exposure method increased the printing speed of the LAPμSL system. However, one challenge associated with improving the printing accuracy is the inferior synchronization between the dynamic exposure pattern and the motion of the optics, since the moving speed of optics was pre-calculated based on the frame rate of the dynamic exposure pattern and was open-loop controlled. To ensure better synchronization and improve the dimensional accuracy of the printed part, we can use machine-vision in-situ monitoring of the projection pattern as feedback and integrate a closed-loop control system with the moving optics. Future investigation includes selection of the wavelength of the monitoring light source, design of the monitoring patterns and set-up of the closed-loop control motion systems. Since the photoinitiator is only sensitive to lights with specific wavelengths, the light source used for in-situ monitoring can be rationally selected and avoid triggering the photopolymerization. Simple monitoring pattern, such as a square or circle, can be used to capture the error of the motion of the projection pattern. The error is feedback into the control system to achieve real-time control and increase the alignment and moving accuracy of the projection pattern.

(2) Reduce surface roughness of the polymer-derived ceramics with micro-scale features. Due to the layer-by-layer fabrication process, the surface roughness of the polymer-derived ceramics is high, limiting its application in micro-scale tooling, precision manipulation and micro transmission mechanisms. To improve the surface finishing of the as-fabricated ceramics, a polishing process should be well developed and follows the sintering and pyrolysis. Future investigation includes selection of abrasives, designing of the polishing fixtures and stock removal. Hardness is one of

the criteria for abrasive selection. The hardness of the polymer-derived ceramics needs to be characterized and used for the selection of abrasive. Other considerations include avoiding chemical reactions, ensuring surface quality and avoiding contaminations. The polishing fixture should fit various sizes of the printed part and ensure the stability of the printed part in the polishing slurry.

(3) Investigate methods to improve the fracture toughness of architected metamaterials. In this study, we found the two factors affecting the fracture toughness in micro-architected metamaterials and we established the experimental protocols to accurately measure the fracture toughness of architected materials. Future work includes (i) Investigating the effect of hierarchy on the fracture toughness of micro-architected metamaterials. (ii) Investigating the effect of multi-material architectures on the fracture energy/damage tolerance. (iii) Characterize the fracture toughness of metamaterials with constituent materials that are not brittle.

(4) Creation and optimization of magnetoelectric energy harvesters via the multi-material AM platform. The AM platform developed in this study is not limited to piezoelectric materials. The platform can be applied to different kinds of functional materials. For instance, both the piezo and magnetic particles can be incorporated with the UV sensitive monomer and used to create magnetoelectric energy harvesting devices, which is one of the most widely employed devices for wirelessly charged batteries in sealed packages. Future investigation includes optimizing particle loadings, designing geometries based on magnetic field distributions to maximize the power density.

(5) Integrating power source, local computation and remote communication system with the self-sensing micro-robot. The payload of the self-sensing robotic system demonstrated in this study reaches 13 times its body weight, allowing the integration of onboard functional components. The robot is powered by an off-board amplifier and controlled by an off-board closed-loop control system. Future work includes designing compact control circuits, 3D printing antenna and integrating functional components with the robotic system to achieve on-board closed-loop control and remote communication.

Reference

1. Cui, H. C.; Hensleigh, R.; Chen, H. S.; Zheng, X. Y., Additive Manufacturing and size-dependent mechanical properties of three-dimensional microarchitected, high-temperature ceramic metamaterials. *J Mater Res* **2018,** *33* (3), 360-371.

2. Wang, C. W.; Ping, W. W.; Bai, Q.; Cui, H. C.; Hensleigh, R.; Wang, R. L.; Brozena, A. H.; Xu, Z. P.; Dai, J. Q.; Pei, Y.; Zheng, C. L.; Pastel, G.; Gao, J. L.; Wang, X. Z.; Wang, H.; Zhao, J. C.; Yang, B.; Zheng, X. Y.; Luo, J.; Mo, Y. F.; Dunn, B.; Hu, L. B., A general method to synthesize and sinter bulk ceramics in seconds. *Science* **2020,** *368* (6490), 521-+.

3. Cui, H. C.; Hensleigh, R.; Yao, D. S.; Maurya, D.; Kumar, P.; Kang, M. G.; Priya, S.; Zheng, X. Y., Three-dimensional printing of piezoelectric materials with designed anisotropy and directional response. *Nat Mater* **2019,** *18* (3), 234-+.

4. Sun, C.; Fang, N.; Wu, D. M.; Zhang, X., Projection micro-stereolithography using digital micro-mirror dynamic mask. *Sensors and Actuators A: Physical* **2005,** *121* (1), 113-120.

5. Zheng, X.; Deotte, J.; Alonso, M. P.; Farquar, G. R.; Weisgraber, T. H.; Gemberling, S.; Lee, H.; Fang, N.; Spadaccini, C. M., Design and optimization of a light-emitting diode projection micro-stereolithography three-dimensional manufacturing system. *Rev Sci Instrum* **2012,** *83* (12), 125001.

6. Ha, Y. M.; Choi, J. W.; Lee, S. H., Mass production of 3-D microstructures using projection microstereolithography. *Journal of Mechanical Science and Technology* **2008,** *22* (3), 514-521.

7. Pan, Y.; Zhou, C.; Chen, Y., A Fast Mask Projection Stereolithography Process for Fabricating Digital Models in Minutes. *Journal of Manufacturing Science and Engineering* **2012,** *134* (5), 051011.

8. Wei, K.; Cheng, X. M.; Mo, F. H.; Wen, W. B.; Fang, D. N., Design and analysis of integrated thermal protection system based on lightweight C/SiC pyramidal lattice core sandwich panel. *Mater Design* **2016,** *111*, 435-444.

9. Bapanapalli, S.; Martinez, O.; Gogu, C.; Sankar, B.; Haftka, R.; Blosser, M., (Student Paper) Analysis and Design of Corrugated-Core Sandwich Panels for Thermal Protection Systems of Space Vehicles. In *47th AIAA/ASME/ASCE/AHS/ASC Structures, Structural Dynamics, and Materials Conference*, American Institute of Aeronautics and Astronautics: 2006.

10. We, K.; He, R. J.; Cheng, X. M.; Zhang, R. B.; Pei, Y. M.; Fang, D. N., Fabrication and mechanical properties of lightweight ZrO2 ceramic corrugated core sandwich panels. *Mater Design* **2014,** *64*, 91-95.

11. Wei, K.; He, R.; Cheng, X.; Zhang, R.; Pei, Y.; Fang, D., A lightweight, high compression strength ultra high temperature ceramic corrugated panel with potential for thermal protection system applications. *Mater Design* **2015,** *66* (Part B), 552-556.

12. Monteverde, F.; Scatteia, L., Resistance to thermal shock and to oxidation of metal diborides-SiC ceramics for aerospace application. *J Am Ceram Soc* **2007,** *90* (4), 1130-1138.

13. Matsumura, Y., Stabilization of Cu/ZnO/ZrO2 catalyst for methanol steam reforming to hydrogen by coprecipitation on zirconia support. *J Power Sources* **2013,** *238*, 109-116.

14. Tamai, N.; Myoui, A.; Tomita, T.; Nakase, T.; Tanaka, J.; Ochi, T.; Yoshikawa, H., Novel hydroxyapatite ceramics with an interconnective porous structure exhibit superior osteoconduction in vivo. *J Biomed Mater Res* **2002,** *59* (1), 110-117.

15. Peroglio, M.; Gremillard, L.; Chevalier, J.; Chazeau, L.; Gauthier, C.; Hamaide, T., Toughening of bio-ceramics scaffolds by polymer coating. *J Eur Ceram Soc* **2007,** *27* (7), 2679-2685.

16. Buchanan, R. C., *Ceramic Materials for Electronics, Third Edition*. Taylor & Francis: 2004.

17. Ibanez-Garcia, N.; Martinez-Cisneros, C. S.; Valdes, F.; Alonso, J., Green-tape ceramics. New technological approach for integrating electronics and fluidics in microsystems. *Trac-Trend Anal Chem* **2008,** *27* (1), 24-33.

18. Rodel, J.; Kounga, A. B. N.; Weissenberger-Eibl, M.; Koch, D.; Bierwisch, A.; Rossner, W.; Hoffmann, M. J.; Danzer, R.; Schneider, G., Development of a roadmap for advanced ceramics: 2010-2025. *J Eur Ceram Soc* **2009,** *29* (9), 1549-1560.

19. Muralt, P., Recent progress in materials issues for piezoelectric MEMS. *J Am Ceram Soc* **2008,** *91* (5), 1385-1396.

20. Waldner, J.-B., *Nanocomputers and Swarm Intelligence*. Wiley-IEEE Press: 2008; p 288.

21. Koller, A., *Structure and properties of ceramics*. Elsevier: Amsterdam ; New York, 1994; p 587 p.

22. Lawn, B. R., *Fracture of brittle solids*. 2nd ed.; Cambridge University Press: Cambridge ; New York, 1993; p xix, 378 p.

23. Evans, A. G., Structural Reliability - a Processing-Dependent Phenomenon. *J Am Ceram Soc* **1982,** *65* (3), 127-137.

24. Zheng, X. Y.; Lee, H.; Weisgraber, T. H.; Shusteff, M.; DeOtte, J.; Duoss, E. B.; Kuntz, J. D.; Biener, M. M.; Ge, Q.; Jackson, J. A.; Kucheyev, S. O.; Fang, N. X.; Spadaccini, C. M., Ultralight, Ultrastiff Mechanical Metamaterials. *Science* **2014,** *344* (6190), 1373-1377.

25. Meza, L. R.; Das, S.; Greer, J. R., Strong, lightweight, and recoverable three-dimensional ceramic nanolattices. *Science* **2014,** *345* (6202), 1322-1326.

26. Zheng, X. Y.; DeOtte, J.; Alonso, M. P.; Farquar, G. R.; Weisgraber, T.; Gemberling, S.; Lee, H.; Fang, N.; Spadaccini, C. M., Design and optimization of a light-emitting diode projection micro-stereolithography three-dimensional manufacturing system. *Rev. Sci. Instrum* **2012,** *83*.

27. Zheng, X. Y.; Smith, W.; Jackson, J.; Moran, B.; Cui, H. C.; Chen, D.; Ye, J. C.; Fang, N.; Rodriguez, N.; Weisgraber, T.; Spadaccini, C. M., Multiscale metallic metamaterials. *Nat Mater* **2016,** *15* (10), 1100-+.

28. Bauer, J.; Meza, L. R.; Schaedler, T. A.; Schwaiger, R.; Zheng, X.; Valdevit, L., Nanolattices: An Emerging Class of Mechanical Metamaterials. *Adv Mater* **2017**.

29. Montemayor, L. C.; Wong, W. H.; Zhang, Y. W.; Greer, J. R., Insensitivity to Flaws Leads to Damage Tolerance in Brittle Architected Meta-Materials. *Sci Rep-Uk* **2016,** *6*.

30. Bauer, J.; Schroer, A.; Schwaiger, R.; Kraft, O., Approaching theoretical strength in glassy carbon nanolattices. *Nat Mater* **2016,** *15* (4), 438-+.

31. Jacobsen, A. J.; Mahoney, S.; Carter, W. B.; Nutt, S., Vitreous carbon micro-lattice structures. *Carbon* **2011,** *49* (3), 1025-1032.

32. Eckel, Z. C.; Zhou, C. Y.; Martin, J. H.; Jacobsen, A. J.; Carter, W. B.; Schaedler, T. A., 3D PRINTING Additive manufacturing of polymer-derived ceramics. *Science* **2016,** *351* (6268), 58-62.

33. Hundley, J. M.; Eckel, Z. C.; Schueller, E.; Cante, K.; Biesboer, S. M.; Yahata, B. D.; Schaedler, T. A., Geometric characterization of additively manufactured polymer derived ceramics. *Additive Manufacturing* **2017,** *18* (Supplement C), 95-102.

34. Gong, B. Y.; Zhao, X. P., Numerical demonstration of a three-dimensional negative-index metamaterial at optical frequencies. *Opt Express* **2011,** *19* (1), 289-296.

35. Chernow, V. F.; Alaeian, H.; Dionne, J. A.; Greer, J. R., Polymer lattices as mechanically tunable 3-dimensional photonic crystals operating in the infrared. *Appl Phys Lett* **2015,** *107* (10).

36. Ashby, M. F., The properties of foams and lattices. *Philos T R Soc A* **2006,** *364* (1838), 15-30.

37. Xu, H.; Pasini, D., Structurally Efficient Three-dimensional Metamaterials with Controllable Thermal Expansion. *Sci Rep-Uk* **2016,** *6*.

38. Shoji, S.; Kawata, S., Two-Photon Lithography. *Nanofabrication Handbook* **2012**, 229-249.

39. Meza, L. R.; Zelhofer, A. J.; Clarke, N.; Mateos, A. J.; Kochmann, D. M.; Greer, J. R., Resilient 3D hierarchical architected metamaterials. *P Natl Acad Sci USA* **2015,** *112* (37), 11502-11507.

40. Kooistra, G. W.; Deshpande, V.; Wadley, H. N. G., Hierarchical corrugated core sandwich panel concepts. *J Appl Mech-T Asme* **2007,** *74* (2), 259-268.

41. Deshpande, V. S.; Ashby, M. F.; Fleck, N. A., Foam topology bending versus stretching dominated architectures. *Acta Mater* **2001,** *49* (6), 1035-1040.

42. Deshpande, V. S.; Fleck, N. A.; Ashby, M. F., Effective properties of the octet-truss lattice material. *Journal of the Mechanics and Physics of Solids* **2001,** *49* (8), 1747-1769.

43. Dong, L.; Deshpande, V.; Wadley, H., Mechanical response of Ti-6Al-4V octet-truss lattice structures. *Int J Solids Struct* **2015,** *60-61*, 107-124.

44. O' Masta, M. R.; Dong, L.; St-Pierre, L.; Wadley, H.; Deshpande, V., The fracture toughness of octet-truss lattices. *Journal of the Mechanics and Physics of Solids* **2017,** *98*, 271-298.

45. Ferren, R. A., Advances in Polymeric Piezoelectric Transducers. *Nature* **1991,** *350* (6319), 26-27.

46. Anderson, J. C.; Eriksson, C., Piezoelectric Properties of Dry and Wet Bone. *Nature* **1970,** *227* (5257), 491-&.

47. Priya, S.; Nahm, S., *Lead-free piezoelectrics*. Springer: New York ; London, 2011; p viii, 528 .

48. Li, F.; Lin, D. B.; Chen, Z. B.; Cheng, Z. X.; Wang, J. L.; Li, C. C.; Xu, Z.; Huang, Q. W.; Liao, X. Z.; Chen, L. Q.; Shrout, T. R.; Zhang, S. J., Ultrahigh piezoelectricity in ferroelectric ceramics by design. *Nat Mater* **2018,** *17* (4), 349-+.

49. Guerin, S.; Stapleton, A.; Chovan, D.; Mouras, R.; Gleeson, M.; McKeown, C.; Noor, M. R.; Silien, C.; Rhen, F. M. F.; Kholkin, A. L.; Liu, N.; Soulimane, T.; Tofail, S. A. M.; Thompson, D., Control of piezoelectricity in amino acids by supramolecular packing. *Nat Mater* **2018,** *17* (2), 180-+.

50. Egusa, S.; Wang, Z.; Chocat, N.; Ruff, Z. M.; Stolyarov, A. M.; Shemuly, D.; Sorin, F.; Rakich, P. T.; Joannopoulos, J. D.; Fink, Y., Multimaterial piezoelectric fibres. *Nat Mater* **2010,** *9* (8), 643-648.

51. Lu, X.; Qu, H.; Skorobogatiy, M., Piezoelectric Micro-and Nanostructured Fibers Fabricated from Thermoplastic Nanocomposites Using a Fiber Drawing Technique: Comparative Study and Potential Applications. *Acs Nano* **2017,** *11* (2), 2103-2114.

52. Masmanidis, S. C.; Karabalin, R. B.; De Vlaminck, I.; Borghs, G.; Freeman, M. R.; Roukes, M. L., Multifunctional nanomechanical systems via tunably coupled piezoelectric actuation. *Science* **2007,** *317* (5839), 780-783.

53. Wang, X.; He, X.; Zhu, H.; Sun, L.; Fu, W.; Wang, X.; Hoong, L. C.; Wang, H.; Zeng, Q.; Zhao, W.; Wei, J.; Jin, Z.; Shen, Z.; Liu, J.; Zhang, T.; Liu, Z., Subatomic deformation driven by vertical piezoelectricity from CdS ultrathin films. *Sci Adv* **2016,** *2*.

54. Ganeshkumar, R.; Cheah, C. W.; Xu, R.; Kim, S.-G.; Zhao, R., A high output voltage flexible piezoelectric nanogenerator using porous lead-free KNbO3 nanofibers. *Appl Phys Lett* **2017,** *111* (1), 013905.

55. Gafforelli, G.; Corigliano, A.; Xu, R.; Kim, S.-G., Experimental verification of a bridge-shaped, nonlinear vibration energy harvester. *Appl Phys Lett* **2014,** *105* (20), 203901.

56. Dagdeviren, C.; Shi, Y.; Joe, P.; Ghaffari, R.; Balooch, G.; Usgaonkar, K.; Gur, O.; Tran, P. L.; Crosby, J. R.; Meyer, M.; Su, Y. W.; Webb, R. C.; Tedesco, A. S.; Slepian, M. J.; Huang, Y. G.; Rogers, J. A., Conformal piezoelectric systems for clinical and experimental characterization of soft tissue biomechanics. *Nat Mater* **2015,** *14* (7), 728-+.

57. Grupp, D. E.; Goldman, A. M., Giant piezoelectric effect in strontium titanate at cryogenic temperatures. *Science* **1997,** *276* (5311), 392-394.

58. Espinosa, H. D.; Bernal, R. A.; Minary-Jolandan, M., A Review of Mechanical and Electromechanical Properties of Piezoelectric Nanowires. *Adv Mater* **2012,** *24* (34), 4656-4675.

59. Laurenti, M.; Canavese, G.; Sacco, A.; Fontana, M.; Bejtka, K.; Castellino, M.; Pirri, C. F.; Cauda, V., Nanobranched ZnO Structure: p-Type Doping Induces Piezoelectric Voltage Generation and Ferroelectric-Photovoltaic Effect. *Adv Mater* **2015,** *27* (28), 4218-4223.

60. Shin, S. H.; Kim, Y. H.; Lee, M. H.; Jung, J. Y.; Seol, J. H.; Nah, J., Lithium-Doped Zinc Oxide Nanowires-Polymer Composite for High Performance Flexible Piezoelectric Nanogenerator. *Acs Nano* **2014,** *8* (10), 10844-10850.

61. Harris, D. T.; Burch, M. J.; Mily, E. J.; Dickey, E. C.; Maria, J. P., Microstructure and dielectric properties with CuO additions to liquid phase sintered BaTiO3 thin films. *J Mater Res* **2016,** *31* (8), 1018-1026.

62. Nag, S. K.; Agrawal, D. C., Piezoelectric and Mechanical-Properties of Ceria-Doped Lead Zirconate Titanate Ceramics. *J Mater Sci* **1992,** *27* (15), 4125-4130.

63. Manna, S.; Brennecka, G. L.; Stevanović, V.; Ciobanu, C. V., Tuning the piezoelectric and mechanical properties of the AlN system via alloying with YN and BN. *Journal of Applied Physics* **2017,** *122* (10), 105101.

64. McCall, W. R.; Kim, K.; Heath, C.; La Pierre, G.; Sirbuly, D. J., Piezoelectric Nanoparticle-Polymer Composite Foams. *Acs Appl Mater Inter* **2014,** *6* (22), 19504-19509.

65. Smay, J. E.; Tuttle, B.; III, J. C., Robocasting of Three-Dimensional Piezoelectric Structures. In *Piezoelectric and Acoustic Materials for Transducer Applications*, Safari, A.; Akdoğan, E. K., Eds. Springer US: Boston, MA, 2008; pp 305-318.

66. Challagulla, K. S.; Venkatesh, T. A., Electromechanical response of piezoelectric foams. *Acta Mater* **2012,** *60* (5), 2111-2127.

67. Zheng, X.; Lee, H.; Weisgraber, T. H.; Shusteff, M.; DeOtte, J.; Duoss, E. B.; Kuntz, J. D.; Biener, M. M.; Ge, Q.; Jackson, J. A.; Kucheyev, S. O.; Fang, N. X.; Spadaccini, C. M., Ultralight, Ultrastiff Mechanical Metamaterials. *Science* **2014,** *344* (6190), 1373-1377.

68. Meza, L. R.; Zelhofer, A. J.; Clarke, N.; Mateos, A. J.; Kochmann, D. M.; Greer, J. R., Resilient 3D hierarchical architected metamaterials. *Proceedings of the National Academy of Sciences* **2015,** *112* (37), 11502-11507.

69. Tumbleston, J. R.; Shirvanyants, D.; Ermoshkin, N.; Janusziewicz, R.; Johnson, A. R.; Kelly, D.; Chen, K.; Pinschmidt, R.; Rolland, J. P.; Ermoshkin, A.; Samulski, E. T.; DeSimone, J. M., Continuous liquid interface production of 3D objects. *Science* **2015,** *347* (6228), 1349-1352.

70. Maxwell, J. C., *Philosophical Magazine* **1864,** *27*, 294.

71. RB, F., Octet truss. *U.S. Patent Serial No. 2* **1961,** *986*, 241.

72. Meza, L. R.; Phlipot, G. P.; Portela, C. M.; Maggi, A.; Montemayor, L. C.; Comella, A.; Kochmann, D. M.; Greer, J. R., Reexamining the mechanical property space of three-dimensional lattice architectures. *Acta Mater* **2017,** *140* (Supplement C), 424-432.

73. Gibson, L. J.; Ashby, M. F., Cellular Solids: Structure and Properties. **1999**.

74. Du, P.; Wang, X. N.; Lin, I. K.; Zhang, X., Effects of composition and thermal annealing on the mechanical properties of silicon oxycarbide films. *Sensor Actuat a-Phys* **2012,** *176*, 90-98.

75. Mocingkharnklang, P.; Elzey, D. M.; Wadley, H. N. G., Titanium matrix composite lattice structures. *Compos Part a-Appl S* **2008,** *39* (2), 176-187.

76. Flores, O.; Bordia, R. K.; Bernard, S.; Uhlemann, T.; Krenkel, W.; Motz, G., Processing and characterization of large diameter ceramic SiCN monofilaments from commercial oligosilazanes. *Rsc Adv* **2015,** *5* (129), 107001-107011.

77. Bazant, Z. P., Scaling Laws in Mechanics of Failure. *J Eng Mech-Asce* **1993,** *119* (9), 1828-1844.

78. Bazant, Z. P., Size effect on structural strength: a review. *Arch Appl Mech* **1999,** *69* (9-10), 703-725.

79. Tsu, T. C.; Mugele, R. A.; Mcclintock, F. A., A Statistical Distribution Function of Wide Applicability. *J Appl Mech-T Asme* **1952,** *19* (2), 233-234.

80. Riley, F., STRUCTURAL CERAMICS Fundamentals and Case Studies Conclusions. *Structural Ceramics* **2009**, 384-393.

81. Riley, F., STRUCTURAL CERAMICS Fundamentals and Case Studies Preface. *Structural Ceramics* **2009**, Xi-Xii.

82. Chantikul, P.; Bennison, S. J.; Lawn, B. R., Role of Grain-Size in the Strength and R-Curve Properties of Alumina. *J Am Ceram Soc* **1990,** *73* (8), 2419-2427.

83. Griffith, A. A., The Phenomena of Rupture and Flow in Solids. *Philosophical Transactions of the Royal Society of London. Series A, Containing Papers of a Mathematical or Physical Character* **1921,** *221*, 163-198.

84. Gao, H. J.; Ji, B. H.; Jager, I. L.; Arzt, E.; Fratzl, P., Materials become insensitive to flaws at nanoscale: Lessons from nature. *P Natl Acad Sci USA* **2003,** *100* (10), 5597-5600.

85. Liontas, R.; Greer, J. R., 3D nano-architected metallic glass: Size effect suppresses catastrophic failure. *Acta Mater* **2017,** *133*, 393-407.

86. Zok, F. W., On weakest link theory and Weibull statistics. *J Am Ceram Soc* **2017,** *100* (4), 1265-1268.

87. Weibull, W., A Statistical Distribution Function of Wide Applicability. *J Appl Mech-T Asme* **1951,** *18* (3), 293-297.

88. Weibull, W., *The phenomenon of rupture in solids*. Generalstabens litografiska anstalts fo?rlag: 1939.

89. Hertzberg, R. W., *Deformation and fracture mechanics of engineering materials*. Wiley: New York, 1976; p xiv, 605 p.

90. Messner, M. C., Optimal lattice-structured materials. *Journal of the Mechanics and Physics of Solids* **2016,** *96*, 162-183.

91. Quintana-Alonso, I.; Fleck, N. A., Fracture of Brittle Lattice Materials: A Review. *Major Accomplishments in Composite Materials and Sandwich Structures: An Anthology Onr Sponsored Research* **2009**, 799-816.

92. Bazant, Z. P.; Pang, S. D., Mechanics-based statistics of failure risk of quasibrittle structures and size effect on safety factors. *P Natl Acad Sci USA* **2006,** *103* (25), 9434-9439.

93. Genet, M.; Couegnat, G.; Tomsia, A. P.; Ritchie, R. O., Scaling strength distributions in quasi-brittle materials from micro- to macro-scales: A computational approach to modeling Nature-inspired structural ceramics. *Journal of the Mechanics and Physics of Solids* **2014,** *68*, 93-106.

94. Begley, M. R.; Philips, N. R.; Compton, B. G.; Wilbrink, D. V.; Ritchie, R. O.; Utz, M., Micromechanical models to guide the development of synthetic 'brick and mortar' composites. *Journal of the Mechanics and Physics of Solids* **2012,** *60* (8), 1545-1560.

95. Roohani-Esfahani, S.-I.; Newman, P.; Zreiqat, H., Design and Fabrication of 3D printed Scaffolds with a Mechanical Strength Comparable to Cortical Bone to Repair Large Bone Defects. **2016,** *6*, 19468.

96. Tankasala, H. C.; Deshpande, V. S.; Fleck, N. A., 2013 Koiter Medal Paper: Crack-Tip Fields and Toughness of Two-Dimensional Elastoplastic Lattices. *J Appl Mech-T Asme* **2015,** *82* (9).

97. Huang, J. S.; Lin, J. Y., Mixed-mode fracture of brittle cellular materials. *J Mater Sci* **1996,** *31* (10), 2647-2652.

98. Huang, J. S.; Gibson, L. J., Fracture-Toughness of Brittle Honeycombs. *Acta Metall Mater* **1991,** *39* (7), 1617-1626.

99. Huang, J. S.; Gibson, L. J., Fracture-Toughness of Brittle Foams. *Acta Metall Mater* **1991,** *39* (7), 1627-1636.

100. Kim, K.; Zhu, W.; Qu, X.; Aaronson, C.; McCall, W. R.; Chen, S. C.; Sirbuly, D. J., 3D Optical Printing of Piezoelectric Nanoparticle - Polymer Composite Materials. *Acs Nano* **2014,** *8* (10), 9799-9806.

101. Jabbari, M.; Hattel, J., Bingham plastic fluid flow model in tape casting of ceramics using two doctor blades - analytical approach. *Mater Sci Tech-Lond* **2014,** *30* (3), 283-288.

102. Song, X.; Chen, Z. Y.; Lei, L. W.; Shung, K.; Zhou, Q. F.; Chen, Y., Piezoelectric component fabrication using projection-based stereolithography of barium titanate ceramic suspensions. *Rapid Prototyping J* **2017,** *23* (1), 44-53.

103. Griffith, M. L.; Halloran, J. W., Stereolithography of ceramics. *Proceedings of the Sixth International Conference on Rapid Prototyping - 1995* **1995**, 25-34.

104. Griffith, M. L.; Halloran, J. W., Freeform fabrication of ceramics via stereolithography. *J Am Ceram Soc* **1996,** *79* (10), 2601-2608.

105. Cui, H.; Hesleigh, R.; Chen, H.; Zheng, X., Fabrication and Size-dependent Mechanical Properties of Three-dimensional Microarchitected, High-temperature Ceramic Metamaterials. *Journal of Material Research* **2017,** (In Press).

106. Yamaguchi, M.; Hashimoto, K. Y.; Kogo, H., Elastic, Piezoelectric and Dielectric-Properties of Composite-Materials. *Ieee T Ultrason Ferr* **1987,** *34* (3), 425-426.

107. Glushanin, S.; Topolov, V. Y.; Krivoruchko, A. V., Features of piezoelectric properties of 0-3 PbTiO3-type ceramic/polymer composites. *Mater Chem Phys* **2006,** *97* (2-3), 357-364.

108. Huang, J. H.; Kuo, W. S., Micromechanics determination of the effective properties of piezoelectric composites containing spatially oriented short fibers. *Acta Mater* **1996,** *44* (12), 4889-4898.

109. Bowen, C. R., Electromechanical Properties in Composites Based on Ferroelectrics. *Eng Mater Process* **2009**, 1-202.

110. Nix, E. L.; Ward, I. M., The measurement of the shear piezoelectric coefficients of polyvinylidene fluoride. *Ferroelectrics* **1986,** *67* (1), 137-141.

111. Wang, H.; Zhang, Q. M.; Cross, L. E.; Sykes, A. O., Piezoelectric, dielectric, and elastic properties of poly(vinylidene fluoride/trifluoroethylene). *Journal of Applied Physics* **1993,** *74* (5), 3394-3398.

112. Yang, L.; Harrysson, O.; West, H.; Cormier, D., Mechanical properties of 3D re-entrant honeycomb auxetic structures realized via additive manufacturing. *Int J Solids Struct* **2015,** *69-70*, 475-490.

113. Liu, W.; Liu, W. T.; Wang, Y. Z.; Xue, C. R.; Wang, J. H.; Yang, J. L., Piezoelectric and mechanical properties of CaO reinforced porous PZT ceramics with one-dimensional pore channels. *Ceram Int* **2017,** *43* (2), 2063-2068.

114. Bowen, C. R.; Perry, A.; Lewis, A. C. F.; Kara, H., Processing and properties of porous piezoelectric materials with high hydrostatic figures of merit. *J Eur Ceram Soc* **2004,** *24* (2), 541-545.

115. Wang, J. X.; Nie, H. C.; Lan, C. F.; Wang, G. S.; Dong, X. L.; Chen, X. F.; Cao, F.; He, H. L., Microstructure, electrical and mechanical properties of MgO nanoparticles-reinforced porous PZT 95/5 ferroelectric ceramics. *Ceram Int* **2013,** *39* (4), 3915-3919.

116. Pu, J. A.; Yan, X. J.; Jiang, Y. D.; Chang, C. E.; Lin, L. W., Piezoelectric actuation of direct-write electrospun fibers. *Sensor Actuat a-Phys* **2010,** *164* (1-2), 131-136.

117. He, X. J.; Yao, K., Crystallization mechanism and piezoelectric properties of solution-derived ferroelectric poly(vinylidene fluoride) thin films. *Appl Phys Lett* **2006,** *89* (11).

118. Babu, I.; de With, G., Highly flexible piezoelectric 0-3 PZT-PDMS composites with high filler content. *Compos Sci Technol* **2014,** *91*, 91-97.

119. Fang, L. C.; Li, J.; Zhu, Z. Y.; Orrego, S.; Kang, S. H., Piezoelectric polymer thin films with architected cuts. *J Mater Res* **2018,** *33* (3), 330-342.

120. Singhal, N.; Sharma, M.; Mangal, S. K., Optimal placement of piezoelectric patches over a smart structure. *Integr Ferroelectr* **2017,** *183* (1), 60-90.

121. Annamdas, V. G. M.; Soh, C. K., Influence of Loading on the Near Field Based Passive Metamaterial in Structural Health Monitoring. *Struct Hlth Monit* **2015**, 633-640.

122. Kim, H.; Torres, F.; Wu, Y. Y.; Villagran, D.; Lin, Y. R.; Tseng, T. L., Integrated 3D printing and corona poling process of PVDF piezoelectric films for pressure sensor application. *Smart Mater Struct* **2017,** *26* (8).

123. Min, Y. H.; Lee, K. S.; Yoon, C. S.; Do, L. M., Surface morphology study of corona-poled thin films derived from sol-gel processed organic-inorganic hybrid materials for photonics applications. *J Mater Chem* **1998,** *8* (5), 1225-1232.

124. He, X. M.; Aizenberg, M.; Kuksenok, O.; Zarzar, L. D.; Shastri, A.; Balazs, A. C.; Aizenberg, J., Synthetic homeostatic materials with chemo-mechano-chemical self-regulation. *Nature* **2012,** *487* (7406), 214-218.

125. Eliades, S. J.; Wang, X. Q., Neural substrates of vocalization feedback monitoring in primate auditory cortex. *Nature* **2008,** *453* (7198), 1102-U8.

126. Wu, W. Z.; Wen, X. N.; Wang, Z. L., Taxel-Addressable Matrix of Vertical-Nanowire Piezotronic Transistors for Active and Adaptive Tactile Imaging. *Science* **2013,** *340* (6135), 952-957.

127. Jaffe, H.; Berlincourt, D. A., Piezoelectric Transducer Materials. *Pr Inst Electr Elect* **1965,** *53* (10), 1372-+.

128. Lifson, M. L.; Kim, M. W.; Greer, J. R.; Kim, B. J., Enabling Simultaneous Extreme Ultra Low-k lin Stiff, Resilient, and Thermally Stable Nano-Architected Materials. *Nano Lett* **2017,** *17* (12), 7737-7743.

129. Kara, H.; Ramesh, R.; Stevens, R.; Bowen, C. R., Porous PZT ceramics for receiving transducers. *Ieee T Ultrason Ferr* **2003,** *50* (3), 289-296.

130. Liu, W.; Xu, J.; Wang, Y. Z.; Xu, H.; Xi, X. Q.; Yang, J. L., Processing and Properties of Porous PZT Ceramics from Particle-Stabilized Foams via Gel Casting. *J Am Ceram Soc* **2013,** *96* (6), 1827-1831.

131. Marselli, S.; Pavia, V.; Galassi, C.; Roncari, E.; Craciun, F.; Guidarelli, G., Porous piezoelectric ceramic hydrophone. *J Acoust Soc Am* **1999,** *106* (2), 733-738.

132. Yang, A. K.; Wang, C. A.; Guo, R.; Huang, Y., Microstructure and Electrical Properties of Porous PZT Ceramics Fabricated by Different Methods. *J Am Ceram Soc* **2010,** *93* (7), 1984-1990.

133. Zhang, Y.; Chen, L. J.; Zeng, J.; Zhou, K. C.; Zhang, D., Aligned porous barium titanate/hydroxyapatite composites with high piezoelectric coefficients for bone tissue engineering. *Mat Sci Eng C-Mater* **2014,** *39*, 143-149.

134. Guo, R.; Wang, C. A.; Yang, A. K., Effects of pore size and orientation on dielectric and piezoelectric properties of 1-3 type porous PZT ceramics. *J Eur Ceram Soc* **2011,** *31* (4), 605-609.

135. Liu, W.; Du, L. J.; Wang, Y. Z.; Yang, J. L.; Xu, H., Effects of foam composition on the microstructure and piezoelectric properties of macroporous PZT ceramics from ultrastable particle-stabilized foams. *Ceram Int* **2013,** *39* (8), 8781-8787.

136. Zeng, Y. S.; Jiang, L. M.; Sun, Y. Z.; Yang, Y.; Quan, Y.; Wei, S.; Lu, G. X.; Li, R. Z.; Rong, J. H.; Chen, Y.; Zhou, Q. F., 3D-Printing Piezoelectric Composite with Honeycomb Structure for Ultrasonic Devices. *Micromachines-Basel* **2020,** *11* (8).

137. Hu, H. J.; Zhu, X.; Wang, C. H.; Zhang, L.; Li, X. S.; Lee, S.; Huang, Z. L.; Chen, R. M.; Chen, Z. Y.; Wang, C. F.; Gu, Y.; Chen, Y. M.; Lei, Y. S.; Zhang, T. J.; Kim, N.; Guo, Y. X.; Teng, Y.; Zhou, W. B.; Li, Y.; Nomoto, A.; Sternini, S.; Zhou, Q. F.; Pharr, M.; di Scalea, F. L.; Xu, S., Stretchable ultrasonic transducer arrays for three-dimensional imaging on complex surfaces. *Sci Adv* **2018,** *4* (3).

138. Jafferis, N. T.; Helbling, E. F.; Karpelson, M.; Wood, R. J., Untethered flight of an insect-sized flapping-wing microscale aerial vehicle. *Nature* **2019,** *570* (7762), 491-+.

139. Ci, P. H.; Liu, G. X.; Chen, Z. J.; Zhang, S. J.; Dong, S. X., High-order face-shear modes of relaxor-PbTiO3 crystals for piezoelectric motor applications. *Appl Phys Lett* **2014,** *104* (24).

140. Yang, J. K.; Li, Z. M.; Xin, X. D.; Gao, X. Y.; Yuan, X. T.; Wang, Z. H.; Yu, Z. H.; Wang, X. H.; Zhou, J.; Dong, S. X., Designing electromechanical metamaterial with full nonzero piezoelectric coefficients. *Sci Adv* **2019,** *5* (11).

141. Sherrit, S.; Domm, L.; Bao, X. Q.; Bar-Cohen, Y.; Chang, Z. S.; Badescu, M., Single Piezo-Actuator Rotary-Hammering (SPaRH) Drill. *Sensors and Smart Structures Technologies for Civil, Mechanical, and Aerospace Systems 2012, Pts 1 and 2* **2012,** *8345*.

142. Koratkar, N. A.; Chopra, I., Testing and validation of a Froude scaled helicopter rotor model with piezo-bimorph actuated trailing edge flaps. *Smart Structures and Integrated Systems - Smart Structures and Materials 1997* **1997,** *3041*, 183-205.

143. Nguyen, X. T.; Calderon, A. A.; Rigo, A.; Ge, J. Z.; Perez-Arancibia, N. O., SMALLBug: A 30-mg Crawling Robot Driven by a High-Frequency Flexible SMA Microactuator. *Ieee Robot Autom Let* **2020,** *5* (4), 6796-6803.

144. Koh, J. S.; Cho, K. J., Omegabot: Crawling Robot Inspired by Ascotis Selenaria. *Ieee Int Conf Robot* **2010**, 109-114.

145. Rafsanjani, A.; Zhang, Y. R.; Liu, B. Y.; Rubinstein, S. M.; Bertoldi, K., Kirigami skins make a simple soft actuator crawl. *Sci Robot* **2018,** *3* (15).

146. Shepherd, R. F.; Ilievski, F.; Choi, W.; Morin, S. A.; Stokes, A. A.; Mazzeo, A. D.; Chen, X.; Wang, M.; Whitesides, G. M., Multigait soft robot. *P Natl Acad Sci USA* **2011,** *108* (51), 20400-20403.

147. Calderon, A. A.; Ugalde, J. C.; Chang, L. L.; Zagal, J. C.; Perez-Arancibia, N. O., An earthworm-inspired soft robot with perceptive artificial skin. *Bioinspir Biomim* **2019,** *14* (5).